Optical Performance of E-beam Deposited ZnSe/BaF_2−Based Distributed Bragg Reflectors in the MWIR Region

BY

DEGINET ADMASSU

M.S., Royal Institute of Technology, Sweden, 2011

THESIS

Submitted as partial fulfillment of the requirements

for the degree of Doctor of Philosophy in Physics

in the Graduate College of the

University of Illinois at Chicago, 2020

Chicago, Illinois

Defense Exam Committee members:

Sivalingam Sivananthan, Chair.

Christoph Grein

Robert Klie

Gregory Brill, Army Research Lab

Silviu Velicu, EPIR

I dedicate this thesis to my wife Selamawit Dagne, my son Amisyas Tebekew, and my parents, for their unreserved support.

Acknowledgements

I am thankful to my advisor Professor Sivalingam Sivananthan for allowing me to work in his Lab. He offered me different projects to choose and allowed me to excel on my current PhD project. Professor Sivananthan has also exposed me to many trainings at the University of Illinois at Chicago, Nanotechnology core facility. I am grateful to Professor Christoph Grein for his unreserved advice, genuine comments, and answering many basic physics questions. He has helped me by reading, guiding, and correcting the thesis thoroughly. I am also grateful to Professor David Smith from Arizona State University, for TEM sample tests and insightful comments. I am also thankful toward other members of my final thesis and preliminary exam committee: Robert Klie, Gregory Brill, Silviu Velicu, and Nibir Dhar. I want to mention Dr. Srini Krishnamurthy for the insightful comments and reading the thesis.

Many thanks to the UIC physics department for the supporting and offering teaching assistantship position throughout the years. Many thanks to the staffs of Nanotechnology core facility for their help in providing training to different MEMS processing equipment. Besides, I would like to thank EPIR Technologies Inc. and Sivananthan Laboratories for the internship and device process engineering roles. I have got a lot of training, professional experience, and financial support to complete my Ph.D. studies by working at Sivananthan Laboratories.

Special thanks to my best friend Tejumade Durowade, I thoroughly enjoyed your company throughout the years. I would never forget all the favors and memorable nights inside the cleanroom. Many thanks to Dr. Suk-Ryong Hahn, Dr. Yong Chang, Ryan Sellers, Peihong Man, Eranjan, Bilash, and Cynthia Deters for your help.

I am grateful to my father Tebekew Admassu, my mother Atnaf Wube, and my youngest brother Michael Admassu (MD) for your help and belief in me throughout the years. I am thankful to my family-in-law who supported me throughout the years.

At last, I would forward special thanks to my wife and son, Selamawit and Amisyas, for their endless love, wisdom, and care. Having you beside me, sharing my experiences has made it truly valuable and unforgettable. I dedicate this thesis to you.

SUMMARY

The distributed Bragg reflectors (DBRs) serve as basic optical elements in various optoelectronics, such as Fabry-Perot resonators, hyperspectral sensors, micro-cavity structures, and waveguide lasers. In this thesis, we have developed, designed, and fabricated highly reflecting, and mechanically stable DBRs comprised of electron beam deposited zinc selenide (ZnSe) and barium fluoride (BaF_2) thin films and explored its use in two applications. ZnSe and BaF_2 dielectric thin films were used for the DBR multilayer structures, with refractive indices, $n = 2.43$ and $n = 1.45$, respectively, at the target mid-wave infrared (MWIR) region. DBRs consisting of triple stacks of alternating ZnSe and BaF_2 multilayers, were deposited on silicon substrate with quarter-wave optical thickness (QWOT) design. The thicknesses of ZnSe and BaF_2 thin films were 416 nm and 689 nm, respectively. The fabricated DBRs showed a central wavelength λ_c= 4 μm and reflection exceeding 93%.

When the central wavelength is tunable, the DBRs are useful in hyperspectral sensing and imaging applications. The Micro-Opto-Electromechanical Systems (MOEMS)-based optical filters, which is made up of two parallel DBRs with half-wavelength optical cavity thickness in between were assembled and characterized. A parallel-plate electrostatic micro-actuation was performed to tune the optical cavity thickness of optical filters and, thus, the transmission wavelength. MOEMS based micro-actuators were chosen since they offer the advantages of inherent ruggedness, cheaper cost, and less maintenance, which make them attractive for many applications including hyperspectral sensing, biomedical drug delivery, autonomous vehicles, and optical communications. The fabricated membranes that are critical for the operation of the MOEMS-based micro-actuators consist of a stationary bulk silicon wafer and a movable MOEMS membrane with three x-beam configurations.

SUMMARY (continued)

An SU-8 negative photoresist layer was deposited on the stationary chip to act as a spacer since it creates a cavity that determines the target wavelength. We achieved maximum stable displacements of 8.75 µm and 9.89 µm for spacer thicknesses of 28 µm and 33 µm at 95 VDC and 128 VDC, respectively, for MEMS micro-actuators with serpentine arm design. Beyond these voltages, we found the displacement of the micro-actuators tended to be non-uniform and unstable. However, because of the defects in the movable DBR, such as bowing, non-planarity, and non-parallelism, the assembled MOEMS optical filters showed limited tunability. This limitation makes MOEMS-based micro-actuators impractical for hyperspectral sensing application.

DBRs have the potential to minimize the cost and increase light absorption when integrated with black phosphorous, a two-dimensional material in the application of next generation 2D MWIR sensors and photodetectors. Most published results are in the short-wavelength infrared (SWIR) and near-infrared (NIR), with limited results in the MWIR. In this thesis, we have successfully designed and fabricated high quality ZnSe/BaF_2 -based DBRs in the MWIR region. A Fabry-Perot optical filter was used to partially transmit and reflect the incident light in the target wavelength. The assembled fixed-cavity Fabry-Perot optical filters achieved a FWHM of 450 nm. For the first time, we further showed that the FWHM of the optical filters can be reduced by $\sim$ 50 % with the addition of a nano-thick silicon monoxide (SiO) interface grading layer between every pair of the quarter-wave optical thick (QWOT) layers in the stack. The SiO interface grading layer with refractive index, $n \sim 1.8$, at the central wavelength of 4 µm acts as anti-reflection coating layer to reduce reflection loss in the DBR multilayer structure. The interface grading layer, $\sim$ 80 nm thick, also has the potential to stop atomic inter-diffusion between the layers to minimize free

carrier absorption. Temperature-dependent optical characterization was performed on the assembled Fabry-Perot optical filters. Our experimental data show that the optical transmission of optical filters increases as we cool to a low temperature (T=120 K); this is due to the freezing of carriers which in turn reduces free carrier absorption.

We achieved the principal thesis goal to design and assemble fixed-cavity interface-graded Fabry-Perot optical filters (with SiO interfacial layers) with optimized optical transmission and spectral finesse. The spectral finesse of graded interface optical filters has increased by ~ 225% compared to the abrupt interface Fabry-Perot optical filters (without SiO interfacial layers) counterparts. We also propose a low-cost next generation micro-cavity structure that can be formed by embedding two dimensional atomic crystals into a DBR structure. The proposed design can be used to increase absorption in 2D materials, when it is embedded inside the cavity of DBR structures. Since 2D materials are showing considerable promise in sensing from visible to LWIR, the high quality fabricated DBRs can be used to increase the efficiency of next generation 2D MWIR infrared sensors and photodetectors.

CONTENTS

FIGURES

TABLES

NOMENCLATURE AND SYMBOLS

FPI	Fabry-Perot interferometer
MCT	Mercury cadmium telluride
λ_{cent}	Central wavelength
DBR	Distributed Bragg reflector
QWOT	Quarter wave optical thickness
E	Electric field
H	Magnetic field
LWIR	Long-wave infrared
η	Optical admittance
ZnSe	Zinc selenide
LPCVD	Low-pressure chemical vapor deposition
BaF_2	Barium fluoride
SiO	Silicon monoxide
SiO_2	Silicon dioxide
ZnS	Zinc sulfide
Ge	Germanium
Si_3N_4	Silicon nitride
MOEMS	Micro opto electromechanical systems
SWIR	Short-wave infrared
MEMS	Micro electromechanical Systems
SOI	Silicon on insulator
PR	Photoresist

CCP	Capacitively coupled plasma
ICP	Inductively Coupled Plasma
DRIE	Deep Reactive Ion Etching
FSR	Free Spectral Range
HF	Hydro-Fluoric acid
KOH	Potassium hydroxide
H_3PO_4	Phosphoric acid
CVD	Chemical-vapor deposition
m	Order of interference, integer
NIR	Near-infrared
N_R	Reflective Finesse
n	Refractive index
FTIR	Fourier-transform infrared
R	Reflectance
A	Absorption
k	Extinction coefficient
α	Absorption coefficient
T	Transmittance
t	Optical cavity length
V	Voltage
MWIR	Mid-wave infrared
V_{pi}	Pull-in voltage
θ_i	Incident angle
λ	Wavelength

PECVD	Plasma-enhanced chemical vapor deposition
QCM	Quartz crystal monitor
FWHM	Full width at half maximum
θ_t	Angle of transmission.
k	Mechanical stiffness constant
F_{mech}	Mechanical restoring force
F_{elec}	Electrostatic force
LEDs	Light-emitting diodes
TMDs	Transition metal dichalcogenides
TOFs	Tunable optical filters

1. Introduction

1.1. MOEMS-Based DBRs

The distributed Bragg reflector (DBR) mirror is comprised from dielectric material layers with alternating refractive indices, n_H and n_L respectively. DBRs are commonly used to create a broad-band reflector. The quarter-wave optical thick (QWOT)-based DBR mirror is the most popular design nowadays. Its simple design, ease of integration and no requirements of post-growth processing makes it attractive in different modern devices. DBR mirrors have been used in various optoelectronic devices, such as, Fabry-Perot optical resonators, hyperspectral sensors, next-generation micro-cavity structures, waveguide lasers, light emitting diodes, optical switches, and other devices [1, 123].

Micro-Opto-electromechanical systems (MOEMS), is a technology that can be defined as miniaturized opto-electromechanical elements that are made using the techniques of micro-fabrication [2, 124]. In the past few decades MOEMS devices have contributed a significant role in the advancement of various industrial applications, such as hyperspectral imagers in chemical detection, accelerometers in automobile airbag systems, scanning electron microscope tips to image single atoms, in medical applications such as biomedical drug delivery, and telecommunications [3, 4]. In military applications, MOEMS-based missile navigation has a reliability that emphasizes on environmental robustness [3, 4].

The physical dimension of MOEMS can vary from 1 μm to several hundred micrometers; this small size is an advantage in that it enables integration with a wide range of systems [2, 124]. MOEMS always have moving parts, which makes MOEMS devices different from integrated circuits [3, 4]. The displacement of MOEMS devices is usually monitored by actuating the movable structures though continuous tuning [4, 124]. MOEMS always appear either in the form of sensors or micro-actuators. Sensors are devices that convert physical parameters such as mechanical, thermal and other forms of energy into an electrical signal, whereas the micro-actuators do vice-versa [2, 6]. In this work, we have employed the parallel-plate electrostatic micro-actuators to displace the MOEMS devices that can tune the target wavelength. The micro-actuation is discussed in detail in the later chapters of this thesis.

MOEMS-based interference optical filters that are important components of the hyperspectral spectrometers and micro-cavity structures have been studied and reported. They were chosen for their many technological applications, since they offer the advantages of low cost, inherent ruggedness, small size and high precision batch processing. In addition, robustness, reliability, and repeatability are often cited properties of MOEMS-based hyperspectral sensors [8, 9].

1.2. Principal goals of the thesis

The principal goals of this thesis study are:

1.Investigate various dielectric thin film materials for optical filtering in the MWIR region.

2. Investigate the optical performance of $ZnSe/BaF_2$-based multilayer DBR structures in the MWIR region.

3. Study the main absorption mechanisms involved in the MOEMS-based optical filters in the MWIR region and to study how the temperature affects the transmission and spectral resolution of fixed-cavity Fabry-Perot optical filters.

4. Design, fabricate, assemble, and characterize various MEMS-based micro-actuators.

5. Increasing the main figures of merit of optical filters, particularly the optical transmission and spectral resolution of optical filters by grading the interfaces of the DBR multilayers with an appropriate grading layer.

6. Propose a low-cost micro-cavity structure that can be used to increase the photon absorption of 2D materials, by embedding them inside the fabricated MWIR fixed cavity DBRs, that has potential applications in next-generation high performance infrared sensors and photodetectors.

1.3. DBR multilayer structures

DBR multilayer structures are highly reflective mirrors, that consist of alternating lossless stack of dielectric materials. The DBR mirrors are always designed to achieve a higher reflection at a specific central wavelength, λ_c . To obtain higher reflectivity, the thicknesses of each DBR layers should satisfy the QWOT, $d_i = {}^{\lambda_c}/_{4n_i}$, that is very critical in achieving constructive interference of the reflected beams at each interface, that increases the reflection of the DBR multilayer structure. Increasing the total number of multilayer stacks is another means to increase reflection of the DBR structure [1, 10, 123].

Choosing the dielectric thin films with suitable material properties in the target wavelength depends on several factors, such as a compatible deposition process, adhesion between the deposited thin films, reproducibility, and spectral range. Various techniques of thin film deposition, that includes either the physical vapor deposition or CVD are used by numerous researchers to fabricate the DBRs [1, 10, 123]. We used E-beam evaporation, a physical vapor deposition method to fabricate DBRs. Various DBR thin films were deposited and characterized for their optical performance using Fourier transform infrared (FTIR) spectroscopy. ZnSe and BaF_2 thin films showed lower absorption losses and lower extinction coefficients in the target MWIR region, hence they were chosen for DBR fabrication [1,10, 123].

In this work, we have developed, designed, and fabricated highly reflecting, and mechanically stable distributed Bragg reflectors (DBRs) comprised of electron beam deposited ZnSe and BaF_2 thin films. ZnSe and BaF_2 thin films were used to fabricate the DBR multilayer structure. The thin films have refractive indices, $n_{ZnSe} = 2.43$ and $n_{BaF_2} = 1.45$, at the target mid-wavelength infrared (MWIR) region. DBRs consisting of triple stacks of alternating ZnSe and BaF_2 layers, with QWOT of 416 nm and 689 nm, respectively were deposited on lightly doped silicon substrate. The fabricated DBRs showed a central wavelength λ_c= 4 µm and reflection exceeding 93%. The DBR mirror can be used to increase absorption in 2D materials, when it is embedded inside the cavity of DBR structures. We believe the fabricated DBRs can be used to increase the efficiency of next generation 2D MWIR infrared sensors and photodetectors [1, 123].

1.4. MOEMS based Fabry-Perot interferometer for hyperspectral sensing

The multiple and overlapping absorption peaks of harmful chemical agents such as CO, CO_2, and hydrocarbons in the MWIR region makes spectroscopic detection an attractive research topic. There is a need to rigorously study the spectral analysis in the infrared region [11]. The Absorption spectra are mostly used to identify the concentration of chemical agents. Various chemical agents have specific absorption peaks that are unique to their atomic structure. The peaks are signatures of the atoms transitions that take place between different energy levels [11]. The incident radiation is absorbed by an atom or molecule, and it will be transferred to a higher energy state. The absorbed photon during the transition has an energy given by $E = hc/\lambda$, where

E, h and λ represent the energy, Planck's constant and wavelength of the incident electromagnetic radiation. In the MWIR region, the transition occurs as a result of vibrational and rotational state transitions of the molecules [12, 13].

A MOEMS-based hyperspectral spectrometer is comprised of a narrow band-pass filter assembled to infrared photodetector as shown in the schematic Fig.1 below. The hyperspectral spectrometer uses a hyperspectral imaging method [14]. The hyperspectral infrared sensors are useful in detecting harmful chemical agents in the MWIR region based on rotational and vibrational spectra [12,13]. It offers the advantages of fast acquisition time, high reliability and long lifetime [13].

The tunable FPI used in the hyperspectral spectrometer is constructed by placing two parallel distributed Bragg reflectors (DBRs) face-to-face separated by an optical cavity. The light that satisfies the resonance condition will be transmitted through the optical filter while the rest of light is reflected. The wavelength tuning capability is obtained by changing the spacer thickness through external bias voltages applied across the two DBRs of the FPI [15]. The FPI is assembled by bonding two DBR membrane chips with an SU-8 photoresist spacer layer that separates them with a predesigned thickness. The accuracy and consistency of the optical cavity affects the wavelength tuning capability and it relies on the spacer fabrication process technology. The finesse of the FPI is predominately dependent on several fabrication conditions, such as structural consistency of DBR, precise control of the thickness accuracy, absorption loss in the multilayers, and consistency of ZnSe and BaF_2 thin films in the DBR structure [12, 15].

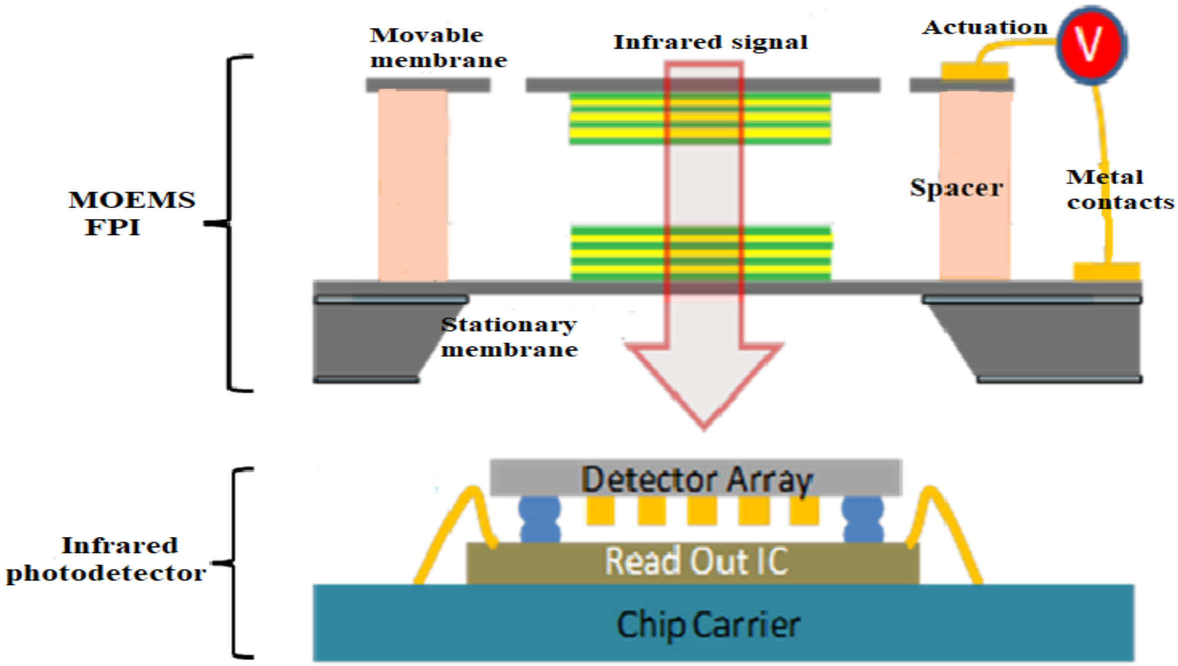

Figure. 1. MOEMS based MWIR hyperspectral imager. The MOEMS-based optical filter is mounted on top of HgCdTe (MCT)-based infrared photodetector. Only a resonance wavelength reaches an infrared photodetector, and the target wavelength is transmitted by controlling the cavity thickness using an electrostatic micro actuation.

Current state of the art MWIR HgCdTe (MCT) photodetectors have high sensitivity but low spectral resolution, hence need to be integrated with tunable optical filters to narrow down the spectral range of infrared detection [12, 15]. The most commonly used approach for tuning the target wavelength is discussed in the next section of this thesis.

1.5. Tunable optical filters

Various types of designs are used to create the tunable optical filters (TOFs). The main filtering mechanisms used nowadays are categorized into three major classes [16], schematic diagrams of the various tunable optical filters are shown in Figure. 2:

1. Fabry-Perot filters (FPFs): It is formed by assembling parallel DBR mirrors with an optical cavity layer between the DBRs. FPFs act as a TOF by changing the cavity length controllably.

2. Grating-based filters: these are interference-based filters which uses interference of waves to disperse incident light. Light that is incident through an entrance slit will be conditioned in a collimating mirror to form a parallel beam. Then, the light will be dispersed at the grating and the dispersed light will be focused using a focusing lens. The Grating-based filters are bulky, slow, power consuming and are not suitable for miniaturization that affects their integration [16].

3. Acousto-optic tunable filters (AOTFs): AOTF is a tunable band-pass filter, which uses the acousto-optic interaction. This filters usually uses the principle of diffraction to disperse an incident radiation [16].

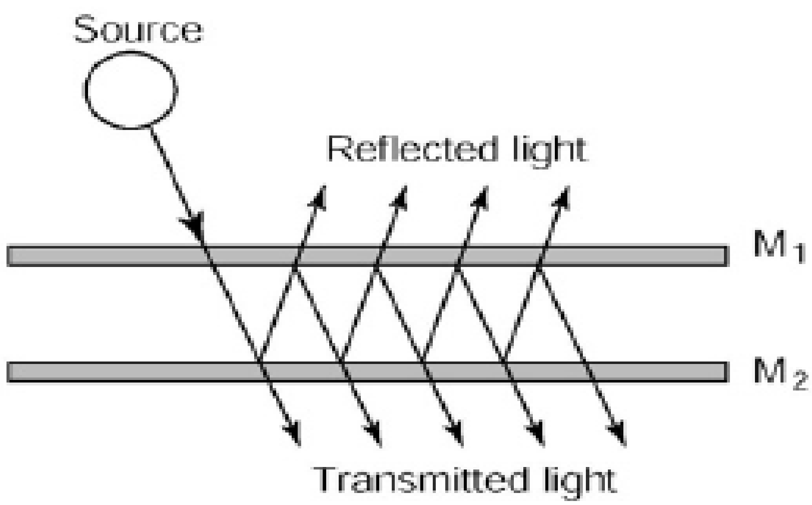

(a) Fabry-Perot optical filters (FPFs)

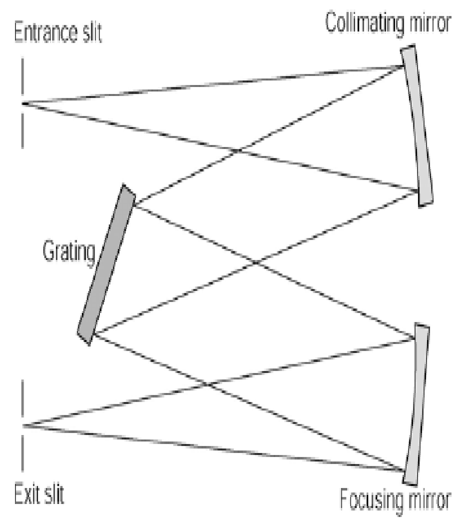

(b) Grating-based filters

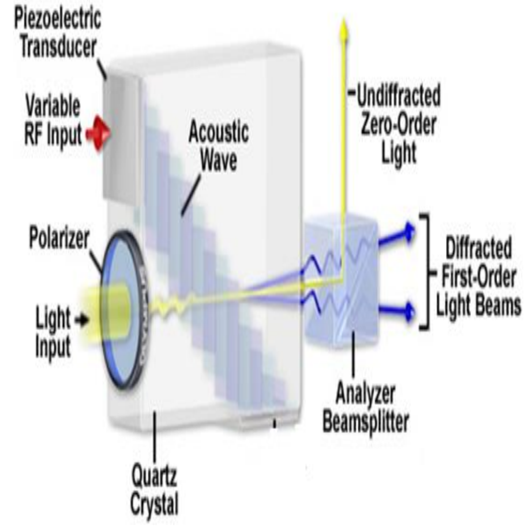

(c) AOTFs

Figure. 2. The various kinds of tunable filters. Source: www.olympusmicro.com

The optical filter presented in this thesis is MOEMS-based FPF. a practical design is the use of an optical cavity between two DBR mirrors to tune the target wavelength. The ease of integration, cheaper fabrication cost, robustness, and lower power consumption makes FPFs preferable compared to the other bulk counterparts. The tunable Fabry-Perot optical filters are important components of MOEMS-based hyperspectral spectrometers. The importance of a TOF in a hyperspectral imaging system is to select a resonant wavelength that can be transmitted out and detected by an infrared photodetector.

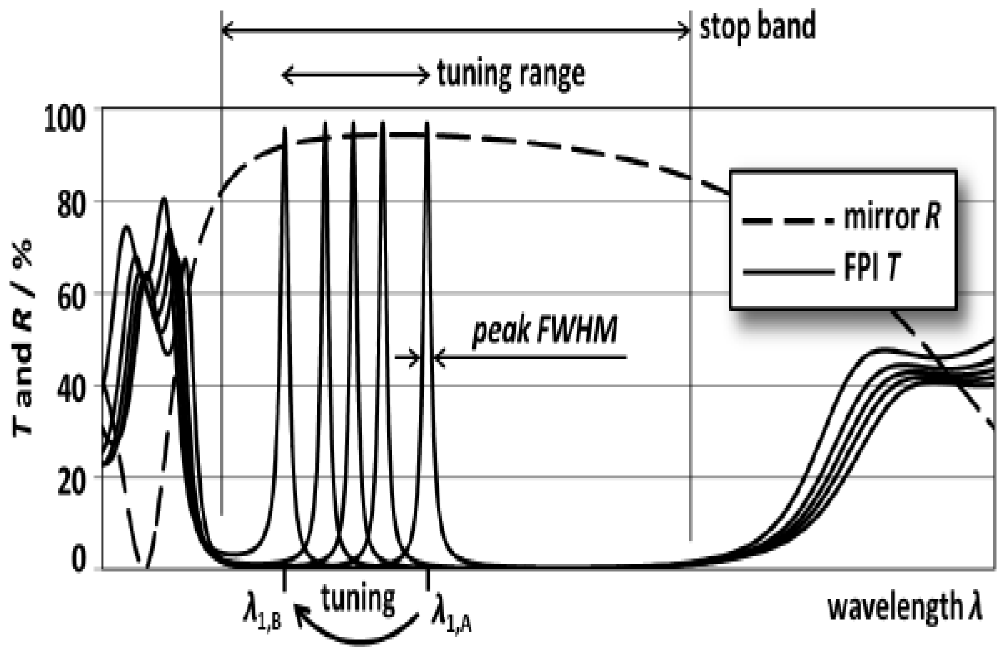

Figure 3. Transmission (T) and reflection (R) of Fabry-Perot optical filters. The optical transmission peak can be altered between λ_{1A} and λ_{1B}. The optical transmission tuning is performed for various optical cavities [19].

The tunable optical filter is a narrow band-pass optical filter for wavelengths that can range from the ultraviolet to far infrared. The FPF usually forms a narrow transmission peak [17, 18]. The optical filter uses the principle of multiple reflection and transmission between the highly reflective parallel DBR mirrors for its operation. Incident electromagnetic radiation is always coupled with the thickness of the air cavity between the DBRs [19, 20]. The transmitted light has a resonance wavelength λ, and it has a magnitude twice the thickness of the spacing between the mirrors and it propagates on the same direction as incident light. Most often the DBRs should be highly reflective with finite transmission; hence we need semi-transparent dielectric mirrors [19, 21].

The main figures of merit of Fabry-Perot optical filters include FWHM, percentage of optical transmission, tuning range, spectral finesse, and cost. The transmission peak FWHM is a standard parameter to quantity the finesse of Fabry-Perot optical filters. For most of the applications considered in this work, we are targeting a narrower the width that has an advantage in increasing the finesse of the optical filters. Optical transmission of the optical filter should be as high as possible. The peak transmission decreases due to absorption losses, lattice mismatch-induced defects, surface roughness and asymmetry between the DBR mirrors [8, 10].

1.5.1. TOFs in MWIR region

The TOF cavity structure is one of the most commonly used approach to filter the incident electromagnetic radiation. The FPF offers an advantage by changing the optical cavity thickness, hence it provides a tunable optical filter. In applications, such as hyperspectral sensing, it requires a narrow band width that is highly resonant. To achieve a highly resonant optical filter, the mirrors should be highly reflective, and high level of parallelism and planarity is expected between the mirrors.

Most published results are in the shortwave infrared (SWIR) and near infrared (NIR), with limited results in the MWIR. In this thesis, we make a TOF in the MWIR region assembled from DBR mirrors that are comprised of ZnSe and BaF_2 dielectric thin films. We believe, it is for the first time that we used ZnSe/BaF_2- based DBRs to realize Fabry-Perot optical filters. Though the refractive index ratio of the selected DBR thin films was not so high, we have successfully designed and fabricated high quality DBRs with reflection exceeding 93% and FWHM of 450 nm. For the first time, we further showed that the FWHM of the optical filters can be reduced by ~ 44.4% with the addition of a nano-thick silicon monoxide (SiO) interface grading layer between every pair of the QWOT DBR layers in the stack. The optical cavity tuning was performed by moving the freely suspended movable mirror using a parallel-plate electrostatic micro-actuation method.

In this study, our goal is to increase the reflective finesse and decrease the FWHM of the optical filter, since this optimizes its spectral resolution. In practice, various non-idealities affect the effective reflective finesse. The next section addresses these effects.

1.6. MEMS-based TOF

MOEMS devices offer the advantages of lower cost, easy integration and lower power consumption. We have developed, designed and fabricated MOEMS devices from silicon-on-insulator (SOI) wafers. Freely suspended moving mirrors have been fabricated using MOEMS micromachining technology. The MOEMs movable membrane mirror that is crucial component for the wavelength tuning is illustrated in Figure. 4. In this figure, we have shown one of the three x-beam micro-actuator configurations with serpentine arm design that showed a maximum displacement while tuning.

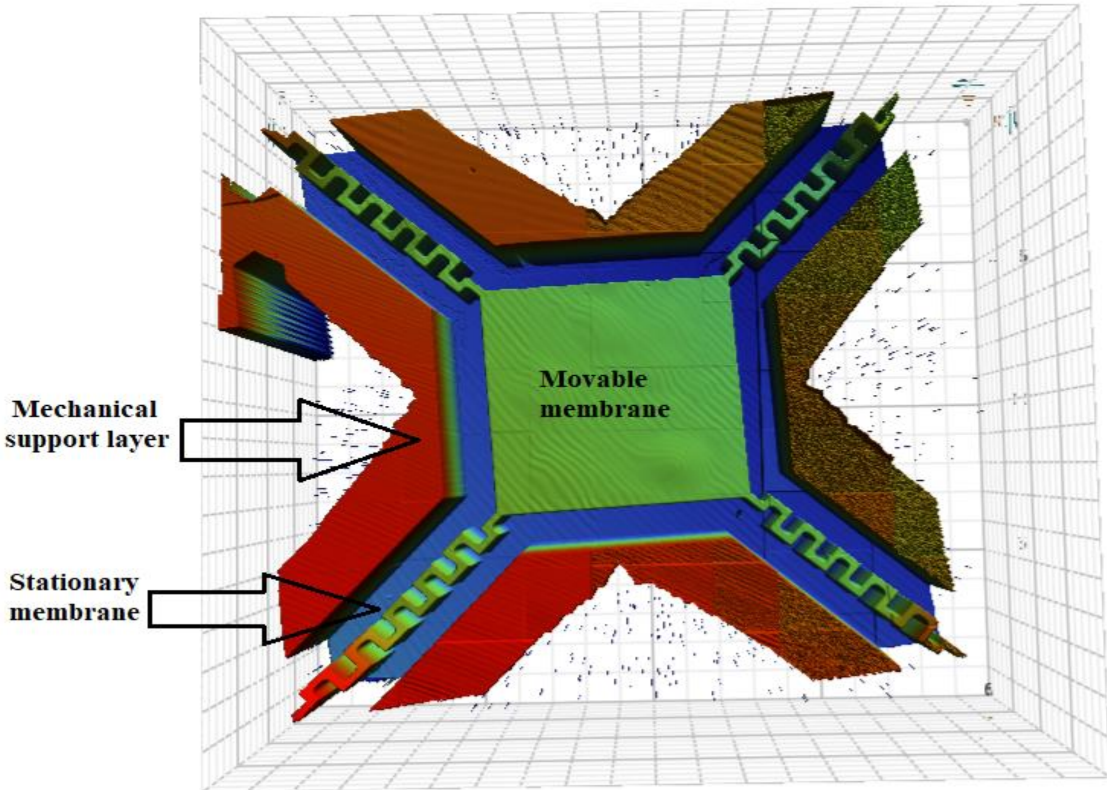

Figure 4. MOEMs micro-actuator. Tuning is performed using parallel-plate electrostatic actuation.

The parallel-plate electrostatic micro actuation was used to change the thickness of optical cavity by displacing the movable mirror under an applied external bias, and thus the transmission wavelength. We have achieved maximum stable displacements of 8.75 µm and 9.89 µm for spacer thicknesses of 28 µm and 33 µm at 95 VDC and 128 VDC, respectively, for MEMS micro-actuators with serpentine arm design.

However, because of the defects in the movable DBR, such as bowing, non-planarity and non-parallelism, our assembled MOEMS devices showed limited tunability. The bowing is expected to arise from variation of stress in the DBR dielectric materials, and the non-parallelism usually occurs when there is a difference in the thickness of the SU-8 photoresist spacer. The curvature in the movable DBR gets worse during the actuation and this effect limits the importance of our device for the hyperspectral sensing application.

Though, the fabricated DBR multilayer structures were not applicable for hyperspectral sensing, we have proposed a design where the DBR mirrors can be used in other applications. In this thesis, we propose a low-cost next generation micro-cavity structure that can be formed by embedding 2D atomic crystals into cavity DBR structures. The micro-cavity structures and its applications are discussed in the next section of this work.

1.7. Micro-cavity structures

Over the last two decades, major research has been focused on minimizing the cost, ease of fabrication and complexity, improving light-matter interaction of two-dimensional novel materials like black phosphorous and graphene [22]. Two-dimensional materials have been considered since they provide exceptional electronic, mechanical and optical properties [23]. The immense interaction of light and matter exhibited by two-dimensional materials has made them applicable in different optoelectronic devices that include photodetectors, polarization selective emitters, and switches [23]. The light-matter interaction of two-dimensional materials can be further controlled by embedding them into DBR mirrors to form optical microcavities [23].

Among the two-dimensional materials, the newly discovered black phosphorous is a good candidate since it offers many advantages that include moderate band gap, easy integration with silicon and can be easily deposited on various electronic materials [22, 23]. Compared to the gapless graphene with high dark current, black phosphorous offers the advantage of suppressed dark current, thus a lower noise photodetection that makes it attractive in enhancing light-matter interactions [24, 25].

It has been studied and demonstrated in the literature that photodetectors with black phosphorous thin films are operable in wavelengths, that range from NIR to MWIR region. Since Black phosphorous thin films offer interesting properties such as lower dark current and high photoconductive gain, it can be leveraged in MWIR photodetectors, and sensors with low light levels [22, 24]. Black phosphorous, which has a band gap of ~ 4.1 µm (0.3 eV) in its bulk form offers a stronger photon absorption. In this thesis we propose a low-cost micro-cavity structure that can be formed by embedding black phosphorous atomic crystals into a mid-wavelength infrared fixed cavity DBRs that can be used to increase the efficiency of those devices. The proposed design can be used to increase the photon absorption of black phosphorous, when it is placed inside the cavity of fabricated DBR structures [22]. We believe the proposed design will open a roadmap towards the development of high-performance next generation mid-wavelength infrared sensors and photodetectors that can be operable in low power detections within the ranges of picowatts [22, 24].

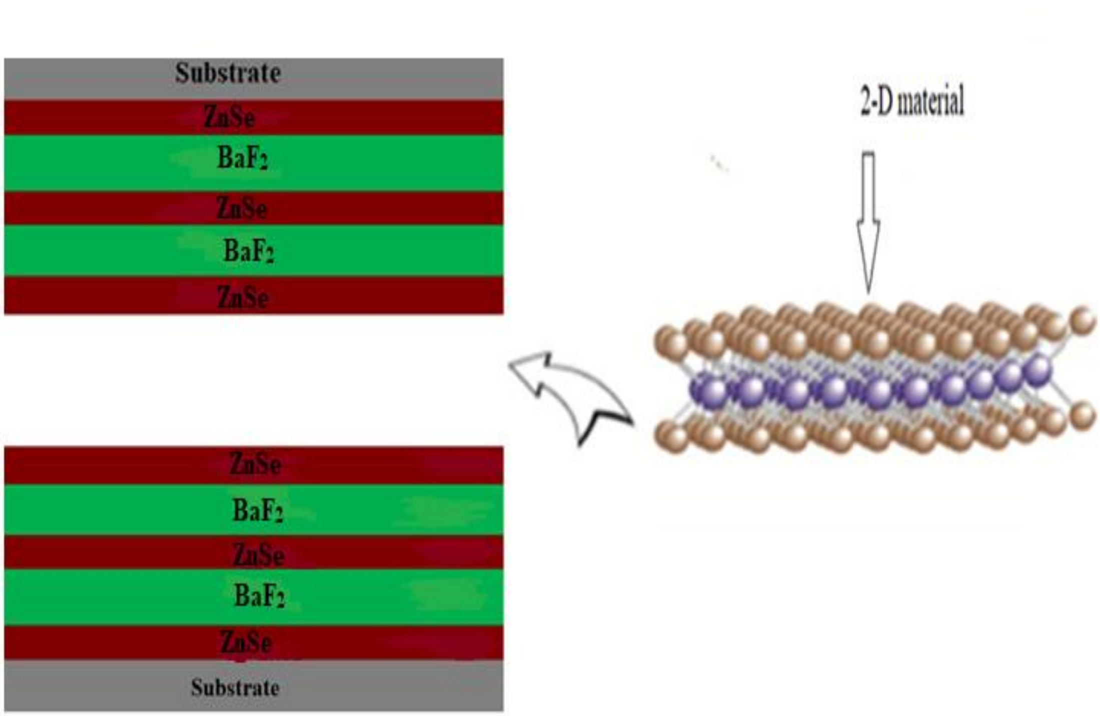

Figure 5. Schematic of micro cavity structure

The proposed optoelectronic device in Figure. 5 is composed of a 2D black phosphorous inserted in the cavity between mid-wavelength infrared DBRs. The fabricated high-quality cavity

DBRs are expected to increase the photon absorption in black phosphorous. The DBR multilayer structure is comprised of alternating ZnSe and BaF_2 thin films that are deposited using an electron beam deposition technique, that will reduce the cost of next generation micro-cavity structures. The fabrication cost of E-beam deposited DBR mirror was very cheap compared to an epitaxial grown mirror. We believe cost is another figure of merit that our proposed micro-cavity structure offers when it is compared with current state of the art photodetectors, that includes Mercury Cadmium telluride (MCT)-based infrared photodetectors.

The DBR micro-cavity structures can also be integrated with other 2D materials, namely the transition metal dichalcogenides (TMDs). TMDs have interesting aspects with unique electronic properties as the materials transform from bulk state to monolayer state [26, 27]. Among the TMDS, Molybdenum disulphide (MoS_2) is widely applied in 2D light emitters, transistors and photodetectors [22, 26]. The novel excitonic properties of 2D MoS_2, such as enhanced direct band gap, small excitonic Bohr radius, and 2D nature of the dipole orientation makes it attractive in applications that demand strong light-matter interactions [26, 27]. The strong light-matter interaction produces a highly directional emission of polaritons that are observed from the coupling between the photons of the DBR structures and excitons of 2D materials. The emitted polaritons have practical applications in the development of polaritonic circuits and switches [26, 27].

The interaction of a dipole in MoS_2 with the cavity photons can also be modified by changing the surrounding dielectric environment [23]. It has been studied and commonly known as the Purcell enhancement, where the emission rate of the dipole is increased by placing 2D materials inside an optical cavity that alters the photon density of states [23,26]. Most of the time, there is a need to create strong light matter interaction by embedding MoS_2 in a dielectric micro-cavity structure. In this case, the interaction between the cavity photons and excitons happens at a very fast rate when compared with the dissipation rates, and this phenomenon creates a half matter-half light bosonic quasiparticle named a cavity polariton [26]. The cavity polaritons can be incorporated in various optoelectronic applications, that includes polaritonic optical spin switches, and quantum confined well structures [24, 26].

1.8. Other applications of MOEMS-based optical filters

Though hyperspectral sensing is one of the primary applications of MOEMS-based optical filters, they can be applied in other technologies as well. MOEMS-based optical filters are useful in the telecommunications industry that demand a wide tuning range, low insertion loss and very low tuning power [28]. MOEMS based optical filters are used as important optical components of various telecommunication devices. Dielectric-based DBRs made from InGaAs/InAlAs layers have been applied in wavelength division multiplexing (WDM) to obtain FWHM of 0.6 nm by Peerling et al., which can optimize the spectral resolution of such devices [29].

Highly efficient light-emitting diodes (LEDs) in the ultraviolet and visible spectral ranges are used to substitute traditional light sources in various applications [30]. LED devices always suffer from light extraction efficiency, the rate at which light is emitted out of the semiconductor material. Various DBRs and photonic crystals are crucial components to optimize the efficiency of LEDs. Specifically, highly reflective DBRs were used to improve the extraction efficiency of LEDs [30, 31].

1.9. Motivation of the study

The demand of MOEMS-based Fabry-Perot optical filters have increased in various optoelectronic applications. The ease of integration and simple design were among the main reasons that makes them highly demanding compared to other counterparts. Fabrication of low-cost MOEMS-based optical filters has opened a range of possibilities and advantages in modern devices. MOEMS-based Interference optical filters are important components in many optoelectronic applications like, hyperspectral sensing of harmful chemical agents, increasing the optical efficiency of LEDs, and increasing the photon absorption of 2D materials by forming micro-cavity structures, that is applicable in increasing the efficiency of next generation 2D infrared sensors and photodetectors.

The primary motivation of this work was to develop MOEMS-based hyperspectral spectrometer to detect harmful chemical agents in the MWIR region. This region has been chosen since this atmospheric transmission window is crowded with multiple overlapping absorption peaks of harmful chemicals that need extensive spectral analysis. However, the lower spectral resolution of the MOEMS-based optical filters, and limited tunability that mainly arises from the defects in the movable DBR micro-mirrors, such as, membrane bowing, and tilting of mirrors makes it impractical for hyperspectral imaging applications.

This thesis also has the motivation to design and fabricate high quality and low-cost DBR mirrors from ZnSe and BaF_2 thin films. Though the ratio between the refractive indices (n_H: n_L) between the selected dielectric thin films was moderate, ~ 1.67, these pair of DBR thin films offer the advantage of no significant transmission wavelength shifting while operating at lower temperatures (T= 120K). We believe our DBR mirror that is comprised of materials with positive and negative thermo-optic coefficients compensate this effect. For the first time, we showed that the spectral resolution of the Fabry-Perot filters can be increased by ≈ 225% by adding a nano-thick silicon monoxide (SiO) interface grading layer between every pair of the quarter wave optical thick (QWOT) layers in the stack. The thesis also explains the fabrication, assembly, testing, and development of MOEMS-based optical filter in the MWIR region.

The thesis has a motivation to develop a low-cost micro-cavity structure that is formed by embedding 2D materials into a low-cost an electron beam-deposited DBR structure, that is highly selective in optical filtering and useful to increase the optical absorption in 2D materials and allows to increase the efficiency of next generation 2D MWIR infrared sensors and photodetectors.

1.10. Thesis structure

This thesis has been organized into eight chapters. Chapter one gives a brief introduction of tunable optical filters and the major applications of MOEMS-based optical filters in the MWIR region. Chapter two discusses the electromagnetic wave theory and the design of optical filters, operating principles and main figures of merit of optical filters that are important in this study are discussed. Chapter three discusses MOEMS and the fabrication flow of MOEMS movable membranes, which are crucial for the realization of micro-actuators. Chapter four addresses the assembly of micro-actuators. In this chapter, various actuation mechanisms of MOEMS-based micro-actuators is discussed. Particularly, parallel plate electrostatic actuation is emphasized in depth since we have employed this method to study the electromechanical properties of the micro-actuators. Chapter five discusses the QWOT-based DBRs that are important optical components of the optical filters, and its design determines the transmitted wavelength. This chapter also discusses the operating principles of DBR mirrors, the different techniques and methods used to fabricate DBR thin films, and the absorption theory of multilayers. Chapter six and chapter seven discuss the results of this work. In chapter six, the mechanical analysis of various micro-actuator designs are explored and discussed. This chapter also gives recommendations to optimize the sensitivity of the micro-actuators. Chapter seven describes the analysis of the optical performance of DBR multi-layers and Fabry-Perot optical filters. The optical modeling of DBRs that guides the experimental design is discussed. Chapter seven also discusses the fabrication, assembly, and optical characterization of Fabry-Perot optical filters. The chapter addresses an alternative mechanism to reduce lattice mismatch-induced defects by engineering the interfaces of the multilayers. Fixed cavity Fabry-Perot optical filters were assembled and the effect of temperature on their optical performance is discussed. Chapter eight provides the conclusions, summarizes current results and suggests future directions of the work.

2. Optical design of Fabry-Perot optical filters

2.1. Optical filters

Thin-film optical filters have been used and applied in various MOEMS-based optoelectronic applications [32]. They are crucial components in various optoelectronic devices such as micro-cavity structures, micro-spectrometers, and LEDs. They are useful to disperse an incident electromagnetic wave into a target wavelength [33]. Interference-based narrow-bandpass optical filters are used in this study to selectively reflect and transmit MWIR radiation.

An interference-based narrow-bandpass optical filter is comprised of alternating dielectric multilayer thin films in which the constructive and destructive interference pattern at the interface between consecutive layers determines the optical performance of the overall device structure. In order to analyze the optical performance of such optical filters, we need to understand electromagnetic wave theory [32, 33]. In this chapter, the basic Maxwell equations and the boundary conditions at the interfaces between the multilayers that govern the reflection and optical transmission of the DBR multilayer structures and absorption are discussed. A Fabry-Perot optical resonator is introduced and its operating principles, main figures of merit, and major challenges as interference-based optical filters are presented.

2.2. Electromagnetic wave theory in dielectric media

Electromagnetic wave theory and the laws of physical optics should be applied to understand the propagation of electromagnetic waves in vacuum and dielectric media. The wave theory always considers light as a transverse electromagnetic wave, that is governed by Maxwell's wave equations [34]. In this section, we solve Maxwell's equations by applying boundary conditions at the interfaces between dielectric media, since their solution is crucial in understanding the interaction of electromagnetic waves with various media [34]. Maxwell's equations for isotropic media with appropriate materials are given by [35]:

$$\nabla \times \boldsymbol{H} = \boldsymbol{J} + \frac{\partial \boldsymbol{D}}{\partial t} \tag{2.1}$$

$$\nabla \times \boldsymbol{E} = -\frac{\partial \boldsymbol{B}}{\partial t} \tag{2.2}$$

$$\nabla . \boldsymbol{D} = \rho \tag{2.3}$$

$$\nabla . \boldsymbol{B} = 0 \tag{2.4}$$

where, $\boldsymbol{J} = \sigma \boldsymbol{E}, \boldsymbol{D} = \varepsilon \boldsymbol{E}\ and\ \boldsymbol{B} = \mu \boldsymbol{H}$. $\boldsymbol{J}, \boldsymbol{D}\ and\ \boldsymbol{B}$ represent the electric current density, electric displacement and magnetic field strength respectively. Again, σ, ε and μ represent the charge density, permittivity and permeability respectively.

In the case when $\rho = 0$, and $\boldsymbol{J} = 0$ respectively. The Maxwell equations will be modified as:

$$\nabla \times \boldsymbol{B} = \mu_o \varepsilon_o \frac{\partial \boldsymbol{E}}{\partial t} \tag{2.5}$$

$$\nabla \times \boldsymbol{E} = -\frac{\partial \boldsymbol{B}}{\partial t} \tag{2.6}$$

$$\nabla . \boldsymbol{E} = 0 \tag{2.7}$$

$$\nabla . \boldsymbol{B} = 0 \tag{2.8}$$

To calculate the Maxwell equations for an electric field wave function in free space we take the curl of Eq. (2.6).

$$\nabla \times (\nabla \times \boldsymbol{E}) = \nabla \times \left(-\frac{\partial \boldsymbol{B}}{\partial t}\right) \tag{2.9}$$

But we have an identity from vector calculus:

$$\nabla \times (\nabla \times \boldsymbol{E}) = \nabla(\nabla . \boldsymbol{E}) - \nabla^2(\boldsymbol{E}) \tag{2.10}$$

Applying the above identity and the relationship in Eq. (2.7) into Eq. (2.9) will give

$$\nabla^2(\mathbf{E}) = \mu_o \varepsilon_o \frac{\partial^2(\mathbf{E})}{\partial t^2} \tag{2.11}$$

Again, we have the standard wave equation given by:

$$\nabla^2 \Psi = \frac{1}{V^2} \frac{\partial^2 \Psi}{\partial t^2} \tag{2.12}$$

By taking analogy with standard wave equation, the plane wave harmonic solution associated with the electric field is given by:

$$\boldsymbol{E}_{r,t} = \boldsymbol{E_o} e^{i(\boldsymbol{k}.\boldsymbol{r} - \omega t + \varphi)} \tag{2.13}$$

In the plane wave Eq. (2.13), **k** represents wave vector, ω denotes the temporal frequency and φ represents initial phase. When the harmonic solution is substituted into Eq. (2.11), it gives a relationship between the wave number and angular frequency of the wave as shown below.

$$-k^2 \boldsymbol{E_o} e^{i(\boldsymbol{k}.\boldsymbol{r} - \omega t + \varphi)} + \varepsilon \mu \omega^2 \boldsymbol{E_o} e^{i(\boldsymbol{k}.\boldsymbol{r} - \omega t + \varphi)} = 0 \tag{2.14}$$

$$k = \omega \sqrt{\varepsilon \mu_o} \tag{2.15}$$

Again, if we reinsert the relationships, $\omega = \frac{2\pi c}{\lambda}$, $\varepsilon = \varepsilon_r \varepsilon_o$, and $c = \frac{1}{\sqrt{\varepsilon_o \mu_o}}$. where c, μ_o, and ε_o represent speed of electromagnetic waves in vacuum, magnetic permeability and electric permittivity in free space respectively into Eq. (2.15):

$$k = \frac{2\pi}{\lambda} \tilde{n} \tag{2.16}$$

where $\tilde{n}$ represents the index of refraction and λ denotes wavelength of the incident electromagnetic wave.

The index of refraction , $\tilde{n} \equiv \sqrt{\varepsilon_r}$, is a physical quantity that characterizes the response of incident electromagnetic wave interaction with the dielectric medium and it is usually expressed by, $\tilde{n} = n + ik$. By substituting refractive index into Eq. (2.13) and assuming the wave propagates along the z-direction produces:

$$\boldsymbol{E}_{z,t} = \boldsymbol{E_o} e^{i\left(\frac{2\pi}{\lambda}(n+ik)\boldsymbol{z}-\omega t+\varphi\right)} = \boldsymbol{E_o} e^{\frac{-2\pi kz}{\lambda}} e^{i\left(\frac{2\pi n\boldsymbol{z}}{\lambda}-\omega t+\varphi\right)} \quad (2.17)$$

Another physical quantity, the Poynting vector, $\boldsymbol{S}$, is an important parameter that should be considered while studying the energy transport in an electromagnetic radiation. The Poynting vector is usually related to the energy of electromagnetic radiation [35]. The poynting vector is given by:

$$\boldsymbol{S} = \boldsymbol{E} \times \boldsymbol{H} \quad (2.18)$$

The time average of an electromagnetic radiation energy or the irradiance is expressed as:

$$\mathrm{I} = \frac{1}{2}\mathrm{Re}(\mathbf{E} \times \mathbf{H}^{*}) = \frac{1}{2}\varepsilon c E^2 \quad (2.19)$$

$$\mathrm{I} = \varepsilon c e^{-4\pi kz/\lambda} * {E_o}^2 = \varepsilon c e^{-\alpha z} * {E_o}^2 \quad (2.20)$$

The distance at which the electromagnetic radiation energy drops to about 37% of its initial value is named the penetration depth and it has a value of, $\frac{\lambda}{4\pi k}$. Its inverse defines the absorption coefficient α, so $\alpha = \frac{4\pi k}{\lambda}$.

2.3. Transmission and reflection at the interfaces of dielectric thin films

When electromagnetic radiation propagates through multilayer thin films, it usually interacts with various materials at different interfaces in which the electromagnetic radiation can be either transmitted, reflected, or absorbed [35]. The plane wave solution describes how the electromagnetic radiation travels within the dielectric media.

We usually consider a normal incident plane polarized harmonic wave in which the electromagnetic radiation propagates from an initial medium with index of refraction, n_0 into another medium with index of refraction n_1 as shown below.

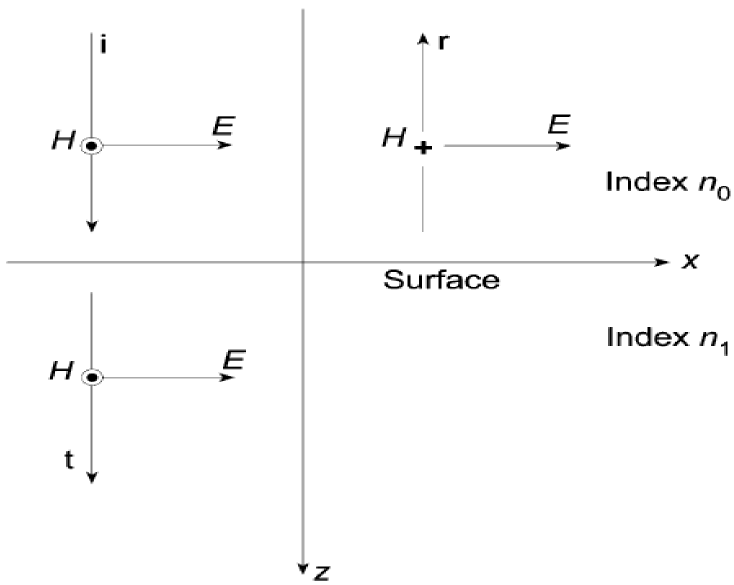

Figure 6. Electromagnetic field vectors at an interface with normal incidence [35].

We have considered normal incident light instead of oblique incident light, since the optical reflection and transmission of the designed FPFs is sensistive to incident flux. To optimize the transmission peak of FPFs a normal incident light with a small field of view should be utilized [35, 36].

Applying the boundary conditions into the Maxwell's wave equations for two different dielectric media that have refractive indices of n_0 and n_1 yields:

$$\boldsymbol{E_i} + \boldsymbol{E_r} = \boldsymbol{E_t} \tag{2.21}$$

$$\boldsymbol{H_i} - \boldsymbol{H_r} = \boldsymbol{H_t} \tag{2.22}$$

When analyzing the reflectivity and transmittivity of FPFs, it is always important to consider the tangential components of the electromagnetic fields. In this case, optical admittance can be written as:

$$\eta = \frac{\boldsymbol{H}}{\boldsymbol{E}} \tag{2.23}$$

Assuming a s-polarized wave, an electromagnetic wave that has normal incident electric field, Eq. (2.22) can be re-written as:

$$\eta_o(\boldsymbol{E_i} - \boldsymbol{E_r}) = \eta_1 \boldsymbol{E_t} \tag{2.24}$$

The amplitude of the coefficients of the reflectivity and transmissivity is given by:

$$\mathrm{r} = \frac{\boldsymbol{E_r}}{\boldsymbol{E_i}} \quad and\ \mathrm{t} = \frac{\boldsymbol{E_t}}{\boldsymbol{E_i}} \tag{2.25}$$

The reflected irradiance and the transmitted irradiance are usually calculated by dividing the reflected and transmitted electromagnetic radiation intensities with respect to the intensity of incident electromagnetic radiation. These relationships can be derived using Eq. (2.19). The solution to the Maxwell equations with refractive indices n_0 and n_1, named the Fresnel equations [35], is given by:

$$R = rr^* = \frac{|\mathbf{E_r}|^2}{|\mathbf{E_i}|^2} = \left(\frac{n_o - n_1}{n_o + n_1}\right)^2$$

$$T = tt^* = \frac{|\mathbf{E_t}|^2}{|\mathbf{E_i}|^2} = \frac{4 n_o n_1}{(n_o + n_1)^2} \tag{2.26}$$

The absorption is assumed to be negligible, that is R+T=1. It should also be noted that the frequency of the electromagnetic radiation is unchanged at the interface, $\omega_r = \omega_t = \omega_i$ [35].

2.4. Optical resonator

An optical resonator is a one dimensional (1D) photonic band gap structure that was first demonstrated by Fabry and Perot in 1899. The optical resonator confines and stores electromagnetic radiation at selected frequencies. The radiation is repeatedly reflected within the optical resonator. A typical optical resonator is comprised of two parallel semi- reflecting and transmitting optical mirrors with an optical cavity thickness t, between them as shown by the schematic Figure 7 below [6, 21, 127].

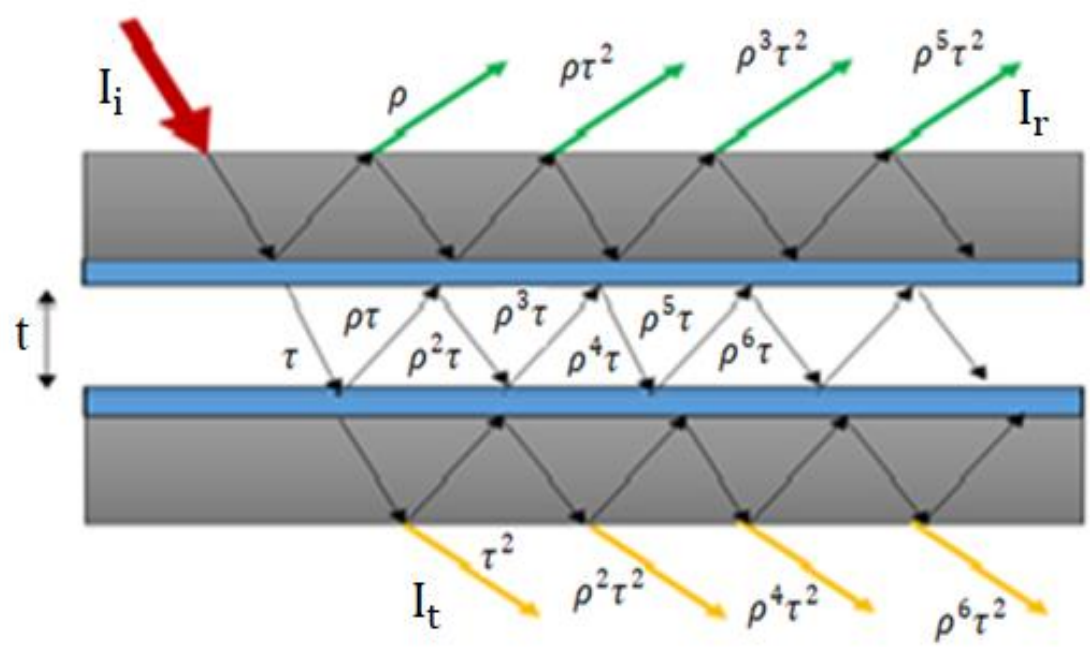

Figure 7. Schematic of Fabry-Perot optical filter.

When electromagnetic waves travel and reflect between the mirrors, constructive and destructive interferences will occur within the cavity [21, 127]. When coherent interference waves transmit, the optical path length difference between adjacent rays is given by:

$$2nt\cos\theta \;=\; \mathrm{m}\lambda \tag{2.27}$$

where n denotes the index of refraction of the media, t represents cavity length, λ denotes wavelength of the incident electromagnetic radiation and m represent the cavity mode number.

We have assumed the angle of incidence to be normal, hence Eq. (2.27) will be modified as:

$$2nt \;=\; \mathrm{m}\lambda \tag{2.28}$$

Hence the cavity length should be given by $t = \frac{\mathrm{m}\lambda}{2n}$. In this work, the cavity is a vacuum medium that has an index of refraction n=1, which gives:

$$t = \mathrm{m}\left(\frac{\lambda}{2}\right)\text{, where m } = 1, 2, 3 \tag{2.29}$$

Electromagnetic waves with special cavity modes are transmitted through the optical cavity, since other wavelengths will destructively interfere [19].

The transmission spectrum $T(\lambda)$ of the Fabry-Perot optical resonator is derived from the multiple reflections and transmissions in the optical cavity [18, 19]. The plane waves that are transmitted through the optical cavity are represented by:

$$\boldsymbol{E_t}(\varphi) = \boldsymbol{E_i}\tau^2 \sum_{k=0}^{k=\infty} \rho^{2k}\, e^{ik\varphi} \tag{2.30}$$

The above expression (Eq.2.30) has a geometrical series solution given by:

$$\boldsymbol{E_t}(\varphi) = \frac{\boldsymbol{E_i}\tau^2}{1 - \rho^2 e^{i\varphi}} \tag{2.31}$$

The transmission of FPF is computed mathematically by taking into consideration of the intensities of the transmitted and incident electromagnetic radiation, and it is called ed the Airy function,

$$T(\lambda) = \frac{I_t}{I_i} = \left|\frac{\boldsymbol{E_t}}{\boldsymbol{E_i}}\right|^2 = \frac{T^2}{(1-R)^2}\left(\frac{1}{1+\frac{4R}{(1-R)^2}Sin^2\left(\frac{\varphi}{2}\right)}\right) \qquad (2.32)$$

In the above expression T denotes the transmissivity, whereas R denotes the reflection of the parallel DBRs, and φ is the phase shift of the DBRs. It has been shown in (Eq.2.32) that transmission of FPFS is controlled by the optical reflection of DBRs [19, 20].

It is known that the incident electromagnetic radiation will either be transmitted, reflected or absorbed by the DBRs, that is $T + R + A = 1,\ 1 - R = T + A$. If we have assumed there is constructive interference between the transmitted waves, the phase change will have a value, $\Delta\varphi = 2m\pi$. By inserting these assumptions into the Airy function, the transmission of FPFs will be modified to:

$$T_{FPI} \cong \left(\frac{1}{(1+\frac{A}{T})^2}\right)_{\mathrm{DBR}} \qquad (2.33)$$

where T_{FPI} represent the transmission of the optical filter, and it is highly dependent on the reflection and absorption coefficients of the DBRs.

2.5. Main figures of merit of a Fabry-Perot optical filter

The most important parameters and figures of merit of FPFs are FWHM, free spectral range and reflective finesse (N_R).

The free-spectral range of FPFs is usually calculated by taking the wavelength difference between two adjacent transmission peaks [37]. In a parallel-plane optical filter, the FSR in terms of wavelength is given by:

$$\lambda_{FSR} = \lambda_m - \lambda_{m+1} = \frac{2nd}{m(m+1)} = \frac{\lambda_m}{m+1} \tag{2.34}$$

The bandwidth or FWHM, is another performance figure of merit that quantifies the spectral resolution of FPFs. FWHM is the spectral distance between two adjacent points in the transmission spectrum in which the spectral points attain a transmission percentage that has half of the maximum value [37]. Assuming lossless mirrors and normal incident light, the FWHM bandwidth is calculated using:

$$\text{FWHM} = \frac{\lambda(1 - \text{R})}{\pi\sqrt{\text{R}}} \tag{2.35}$$

The other important parameter to be considered in FPFs is the finesse,N_R, it is calculated by dividing FSR with respect to the FWHM. Mathematically, it is expressed as:

$$N_R = \frac{FSR}{FWHM} \approx \frac{\pi\sqrt{R}}{1 - R} \tag{2.36}$$

The reflective finesse N_R is a useful parameter that gives us information about the spectral resolution of optical filters. A higher the reflective finesse means better spectral resolution [37].

2.6. Defects in Fabry-Perot optical filters

Fabricated Fabry-Perot optical filters always have defects that deviate their performance from ideal theory. The main defects of optical filters are introduced through tilting, bowing and roughness on the surfaces of DBRs [37].

To analyze the defects of FPFs, it has been assumed that one of the mirrors is perfectly ideal and the other mirror is assumed to have all the defects [37]. The different types of defects associated with Fabry-Perot optical filters are shown in the schematic Figure below.

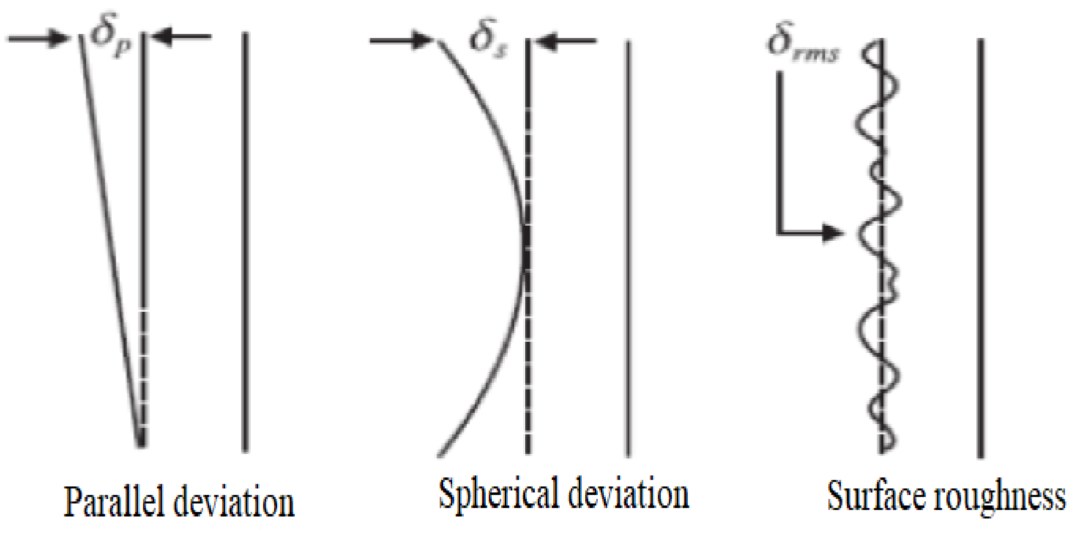

Figure. 8. Schematic of defects in Fabry-Perot optical filters [37].

The parallel-deviation defect results from tilting of the mirrors and thickness variations in the optical spacer cavity layer [37]. The finesse associated with this kind of defect is given by:

$$N_{Dp} = \frac{\lambda}{\sqrt{3}\delta_p} \tag{2.37}$$

The spherical deviation defect mainly results from the bowing of mirrors due to mismatched stresses in the mirror materials. The finesse due to spherical deviation is mathematically given by [37]:

$$N_{Ds} = \frac{\lambda}{2\delta_s} \tag{2.38}$$

The surface roughness deviation, results from a non-ideal surface at the interface between alternating layers of the mirrors. The variation in the roughness of the mirrors is due to the thickness variations in the multilayers and deposition characteristics. The effect of the root mean square roughness finesse is:

$$N_{Dr} = \frac{\lambda}{3\sqrt{3}\delta_{rms}} \tag{2.39}$$

The effective finesse (N_{Eff}), of a fabricated Fabry-Perot optical filter considering all the above defects and non-idealities is given by:

$$\frac{1}{{N_{Eff}}^2} = \frac{1}{{N_R}^2} + \frac{1}{{N_{Dp}}^2} + \frac{1}{{N_{Ds}}^2} + \frac{1}{{N_{Dr}}^2} \qquad (2.40)$$

In Eq. (2.40), $\mathrm{N_R}$ is the ideal finesse of the Fabry-Perot optical filter, whereas $\mathrm{N_{Dp}}$, $\mathrm{N_{Ds}}$, and $\mathrm{N_{Dr}}$ represent the non-parallelism, spherical deviation and surface roughness finesses that arise from the defects of the optical mirrors.

It is important to consider defects and design mitigation mechanisms during the fabrication of Fabry-Perot optical filters. These non-idealities have effects that will later minimize the optical performance and degrade bandpass filtering mechanism needed for the accurate detection of absorption and transmission peaks [37].

3. Fabrication of MOEMS movable membranes

3.1. MOEMS fabrication

The fabrication of MOEMS-based devices meant for integration with fully-developed sensing systems is a steadily advancing field. It is now possible to fabricate resonators, sensors, actuators and cantilever beams that exhibit reproducible characteristics on the micro-scale [3, 63]. However, the integration of these devices with fully-developed systems, such as infrared detectors, is a challenge that still limits their use in various applications. MOEMS-based micro-actuators have non-idealities such as non-parallelity, oscillations and non-ideal anchors make integration with infrared devices difficult.

MOEMS devices are fabricated through a batch process in which many identical chips are fabricated simultaneously on silicon wafers [3, 4, 125]. MOEMS fabrication technology has been derived from IC technology and is named micromachining [3, 4, 125]. Micromachining technology always combines bulk micromachining, surface micromachining and micro-molding [3, 4, 125]. Bulk micromachining is the oldest part of the MOEMS fabrication process. Here, mechanical structures are fabricated by the selective etching and removal of a bulk material. Masking films and etch stopping techniques are crucial components of bulk micromachining [3, 4, 125]. Surface micromachining does not etch the substrate, rather thin film materials such as photoresist layers are selectively added and etched away from the substrate. Surface micromachining is preferred when there is a need to fabricate complex mechanical and free-standing membranes. It has compatibility with IC processing, but it creates two-dimensional structures, a major draw-back of surface micromachining technology [3, 4, 125]. Micro-molding is the third micromachining method usually named the LIGA method. It relies on lithography, electroforming, and molding.

The wafers are exposed using x-ray photolithography. The LIGA method has been applied to very few devices since the technology is very expensive [3, 4, 125].

The following sections describe the fabrication and process flow of movable membranes from SOI wafers that are crucial for the realization of MEMS micro-actuators.

3.2. Fabrication flow of MOEMS movable membranes

The movable membrane that is critical for a MOEMS micro-actuator was fabricated on (100) oriented SOI starting wafer. SOI wafer is comprised of a stack of three layers, a thick bulk handle wafer, a very thin layer of buried SiO_2 insulating layer and single crystalline silicon device layer. In this work, an SOI wafer that has a 500 μm thickness was used to fabricate movable membranes. Currently, SOI wafers are fabricated using two different technologies. The first approach is named the separation by Implanted Oxygen (SIMOX) method and uses ion implantation technique to deposit oxygen ions followed by the annealing of ions at a higher temperature to form buried oxide (BOX) layer on a bulk silicon substrate [38, 39]. The second approach is named the layer transfer technique. In this case, SOI wafers were fabricated by bonding two silicon wafers, one of the wafers is a very high-quality pure wafer and the second wafer has a thin oxide layer [39]. The layer transfer technique provides better quality SOI wafers that are compatible with silicon micromachining.

A SOI wafer is chosen as a starting wafer for MOEMS membrane fabrication since it has a stable oxide that is preferentially etched away by hydrofluoric acid (HF) with high etching selectivity to silicon. A SOI wafer offers several advantages such as reducing leakage currents in various MEMS devices, compatibility with silicon processing, and operability at high temperatures and in extremely harsh environments [38].

3.2.1. Front side photolithography

The surface of the SOI wafer was firstly cleaned with cleaning solvents such as, acetone, methanol, isopropyl alcohol and DI water before starting the front side photolithography. The surface cleaning removes dust particles and residues. The front side photolithography has been performed on the device layer. This photolithography process involves three main sequential steps, spin coating of a photosensitive thin film polymer, exposure to ultraviolet light where the designed features of the photomask are transferred to the photoresist and immersion of the substrate in an aqueous developer solution to dissolve the photoresist and make visible the latent designed device features [4, 125].

The initial photolithographic patterning was done by spin coating the wafer with AZ9260, a positive photoresist. The spin-coated wafer was baked with hot plate to remove solvents and densify the thin film. The baked wafer was then exposed using Karl Suss mask aligner in contact mode with UV light ~ 250mJ/cm^2. The exposed wafer was developed with 1:3 AZ340: DI water developer solution for 30 seconds. The photoresist has shown good integrity. The main purpose of the front side photolithographic step is to delineate the eventual electrical and optical active device area from the mechanical support layer. In addition, the photoresist thin film also serves as a masking layer to protect the device layer prior to the subsequent deep reactive ion etching (DRIE) [4, 125].

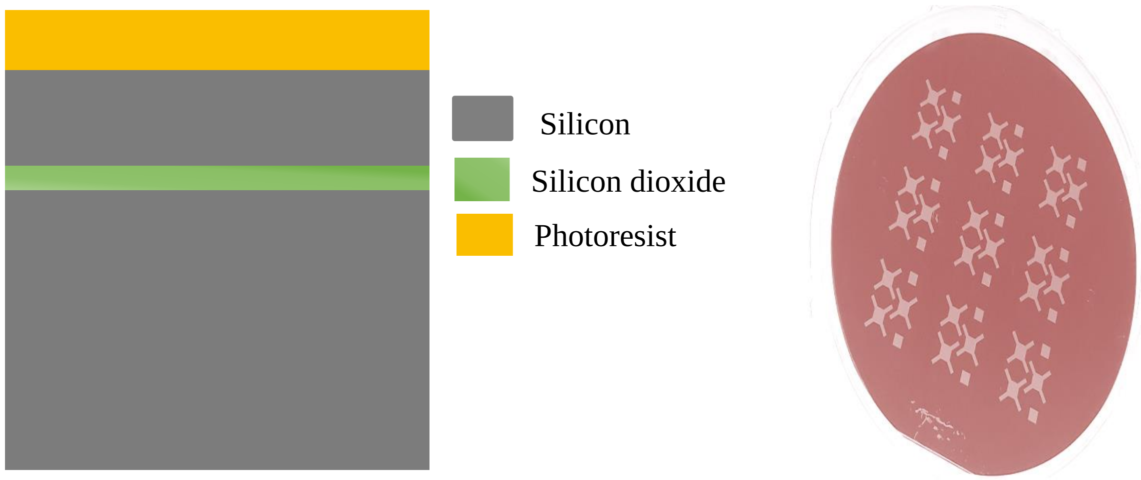

Figure 9. Schematic of front-side photolithography

3.2.2. Deep RIE

Deep RIE is an anisotropic dry etching technique which uses fluoride-based chemistries to etch silicon wafers. Various etching processes have been developed to achieve the proper etching profile in SOI wafers [40]. Bosch etching process, a patented process developed by Bosch Inc. has been used to selectively etch silicon on the device layer. The process consists of alternative passivation and etching steps that utilizes ICP-RIE system. The Substrate is initially coated with a teflon-like passivation layer by utilizing octafluorocyclobutane (C_4F_8) source gases. In the following etch step, reactive fluorine radicals and vertically oriented ions (${SF_x}^+$) remove the passivation polymer, while the passivation polymer remains intact along sidewalls. Alternating passivation and etching steps result in an anisotropic etch profile [40].

The ICP-RIE etching process consists of two plasma sources: an ICP source to generate high densities of ions and neutrals to etch the substrate, and an externally applied RF power to provide greater excitation of the electron cloud that manipulates the transfer and velocity of the ions which bombard the SOI wafer. The etching mechanism is comprised of chemical etching and mechanical milling [40].

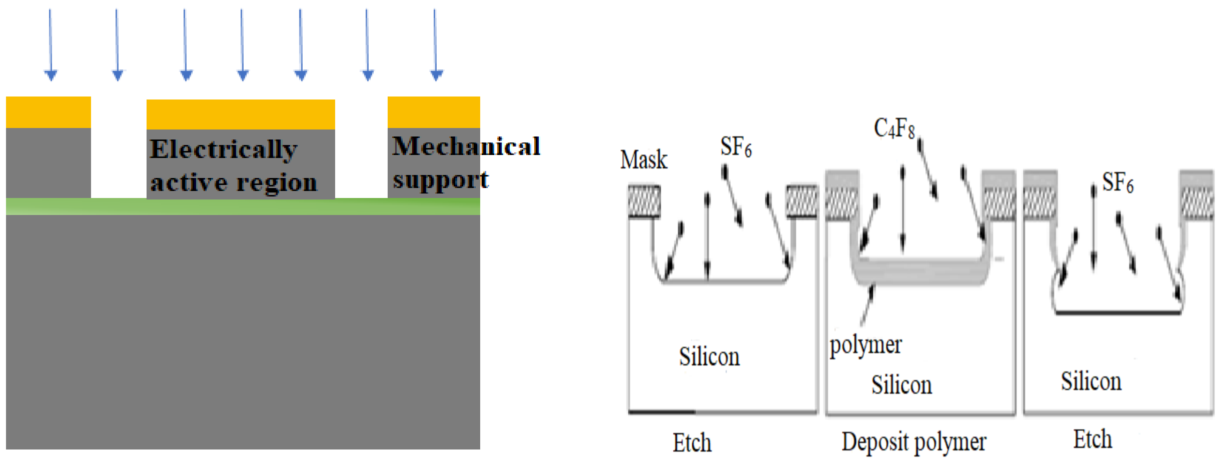

Figure 10. Schematic diagram and principle of DRIE Bosch process [40].

Deep trenches created in the front side of the wafers isolate the individual three x-beams from one another that will be discussed in the later sections of this study. The deep trenches also separate the electrically active regions from the mechanical support layer as shown in the schematic Fig. 10 above. The detailed recipe for the DRIE is given in table I.

Process	Etch	Deposition
SF_6(SCCM)	100	1
C_4F_8(SCCM)	1	100
Time (Sec)	10	4
Forward power	500W	
ICP power	1500W	
Number of cycles	25	
Etch amount (µm)	~ 34 µm	

Table I: DRIE recipe.

A photoresist of ~ 4 µm thickness masking layer has been spin-coated prior to etching. The etching profile was characterized using SEM, and the profile after dry etching step is shown in the Fig .11 below.

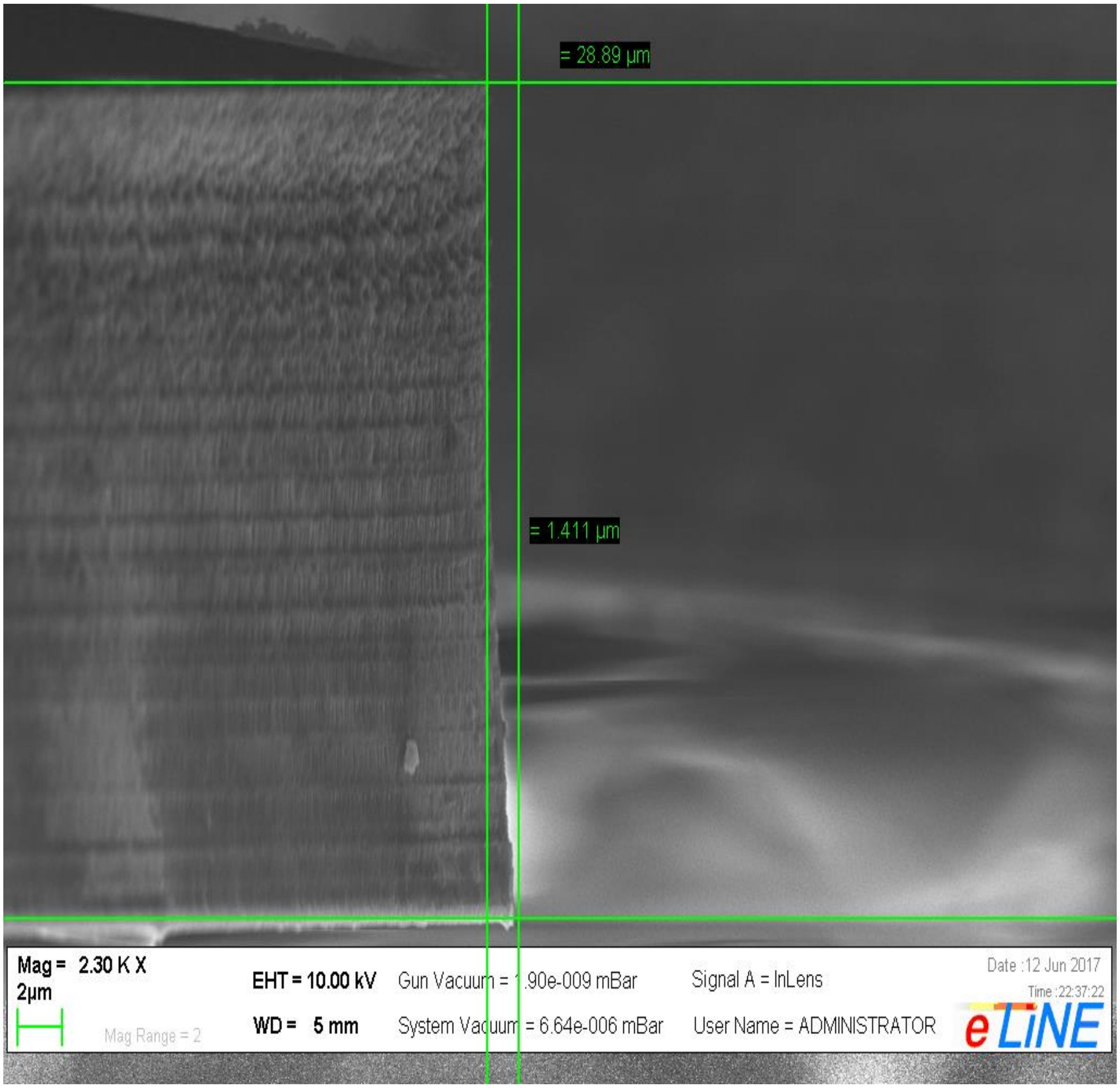

Figure 11. SEM cross-sectional image of device layer (~ 30 µm) after DRIE step, with sidewall angle ~ 87.2°.

3.2.3. LPCVD Si_3N_4 deposition

The Masking sacrificial layer of Si_3N_4 has been deposited on SOI wafers with PTL-LPCVD system at a higher temperature of an 805˚C ambient. Silicon nitride was chosen since it has an etching selectivity with silicon which is close to infinity [38]. PTL-LPCVD system deposits Si_3N_4 by reacting dichlorosilane ($SiCl_2H_2$) and ammonia (NH_3) gases according to the overall reaction:

$$3SiCl_2H_2 + 4NH_3 \dashrightarrow Si_3N_4 + 6HCl + 6H_2$$

Many deposition parameters and process steps including, temperature, total pressure, reactant ratios, will have to be controlled in the process. Table II shows the basic process steps.

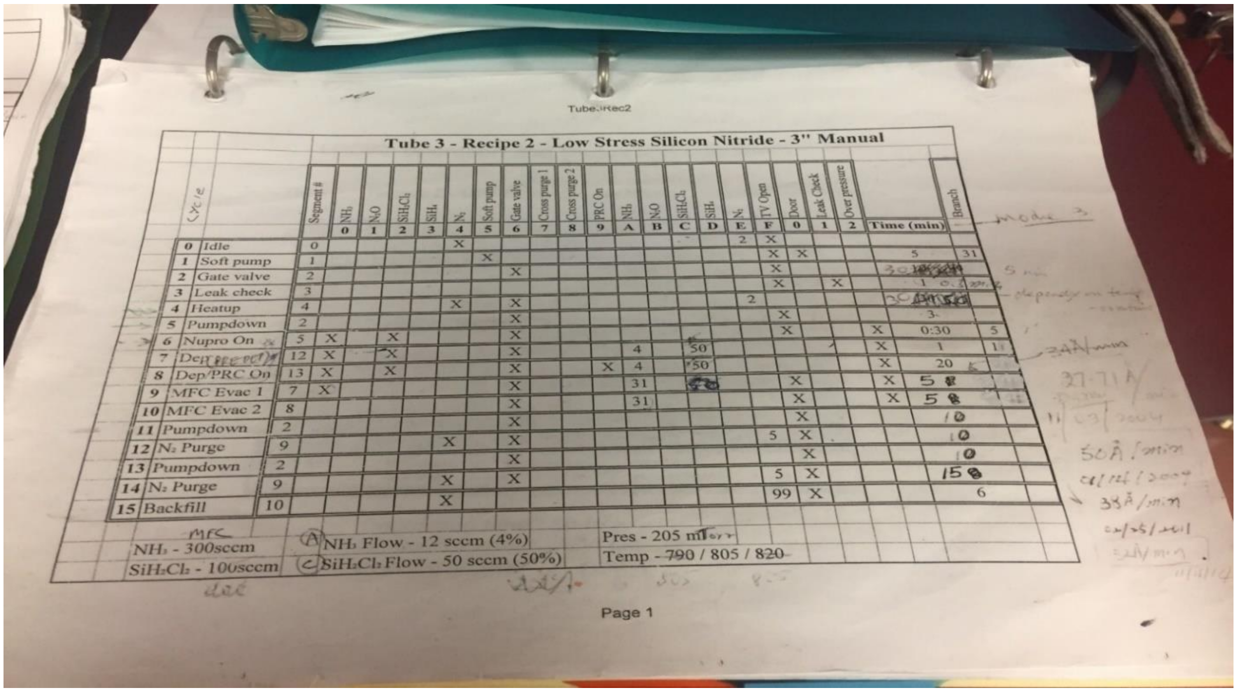

Tube3Rec2

Tube 3 - Recipe 2 - Low Stress Silicon Nitride - 3" Manual

Cycle	Segment #	NH_3 0	N_2O 1	SiH_2Cl_2 2	SiH_4 3	N_2 4	Soft pump 5	Gate valve 6	Cross purge 1 7	Cross purge 2 8	PRC On 9	NH_3 A	N_2O B	SiH_2Cl_2 C	SiH_4 D	N_2 E	TV Open F	Door 0	Leak Check 1	Over pressure 2		Time (min)	Branch
0 Idle	0					X										2	X						
1 Soft pump	1						X										X	X				5	31
2 Gate valve	2							X									X					30	
3 Leak check	3																X		X			1	
4 Heatup	4					X		X								2						30	
5 Pumpdown	2							X									X					3	
6 Nupro On	5	X		X				X									X				X	0:30	5
7 Dep	12	X		X				X				4		50							X	1	11
8 Dep/PRC On	13	X		X				X			X	4		50							X	20	
9 MFC Evac 1	7	X						X				31		50			X				X	5	
10 MFC Evac 2	8							X				31					X				X	5	
11 Pumpdown	2							X									X					10	
12 N_2 Purge	9					X		X								5	X					10	
13 Pumpdown	2							X									X					10	
14 N_2 Purge	9					X		X								5	X					15	
15 Backfill	10					X										99	X					6	

MFC
NH_3 - 300sccm
SiH_2Cl_2 - 100sccm

(A) NH_3 Flow - 12 sccm (4%)
(C) SiH_2Cl_2 Flow - 50 sccm (50%)

Pres - 205 mTorr
Temp - ~~790~~ / 805 / ~~820~~

Page 1

Table II. LPCVD Si_3N_4 deposition recipe

A ~ 0.2 μm thickness of Si_3N_4 layer has been deposited on the SOI wafer by using the deposition recipe in Table II. The purpose of depositing silicon nitride layer is to mask the active device layer from alkaline wet etchants. As shown in Table II various parameters are used to deposit the silicon nitride layer. The flow rates used at this processing step are 12 sccm and 50 sccm for NH_3 and SiH_2Cl_2 gases respectively. Following this step, the wafer is flipped over and the rest of the processing is done on the handle layer. A photoresist is deposited on the handle layer and back side aligned with the features on the device layer prior to reactive ion etching (RIE).

3.2.4. RIE

RIE is an isotropic dry etching technique that was used to etch silicon nitride on the handle wafer. The STS-RIE system utilizes capacitively coupled plasma system. Most of the time, this etching step combines chemical reaction and mechanical milling. CCP-RIE offers a lower plasma density when compared to inductively coupled plasma (ICP-RIE) systems. The ion density and the momentum of the ions cannot be controlled separately in the CCP-RIE systems. The plasma is usually created by a single RF source, unlike the ICP-RIE system. Always there exists a voltage difference in between the created plasma and the wafer holder, commonly called the DC bias. And the bias serves to accelerate ions towards the substrate [42].

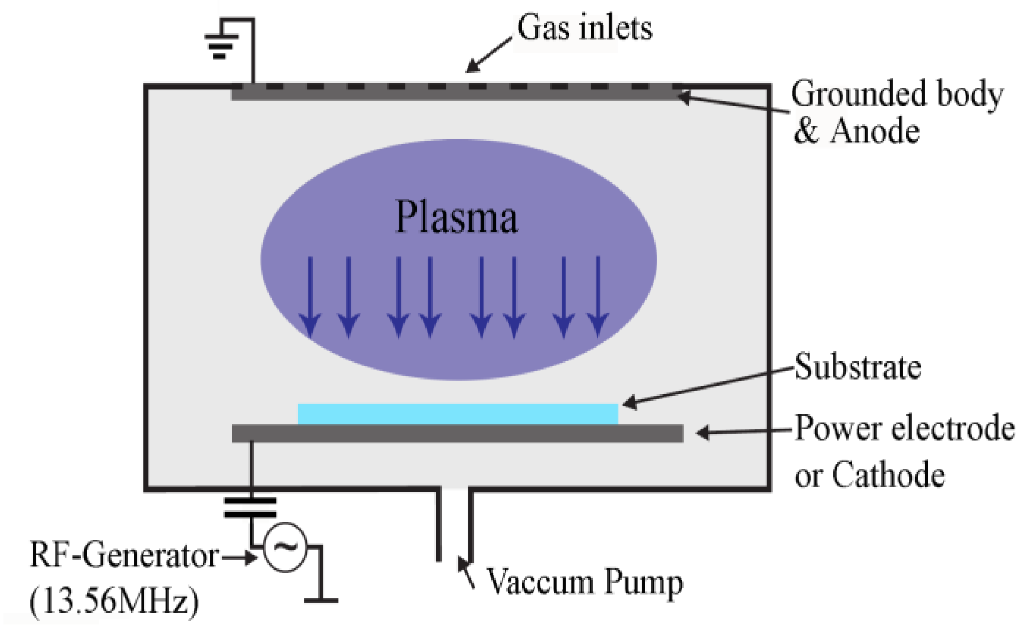

Figure 12. Schematic of a CCP-RIE system [43].

The CCP-RIE system utilizes CF_4 and O_2 gases to etch away silicon nitride thin film from the handle layer. This isotropic etching opens a window on the handle wafer that corresponds to the x-beam active areas on the device layer.

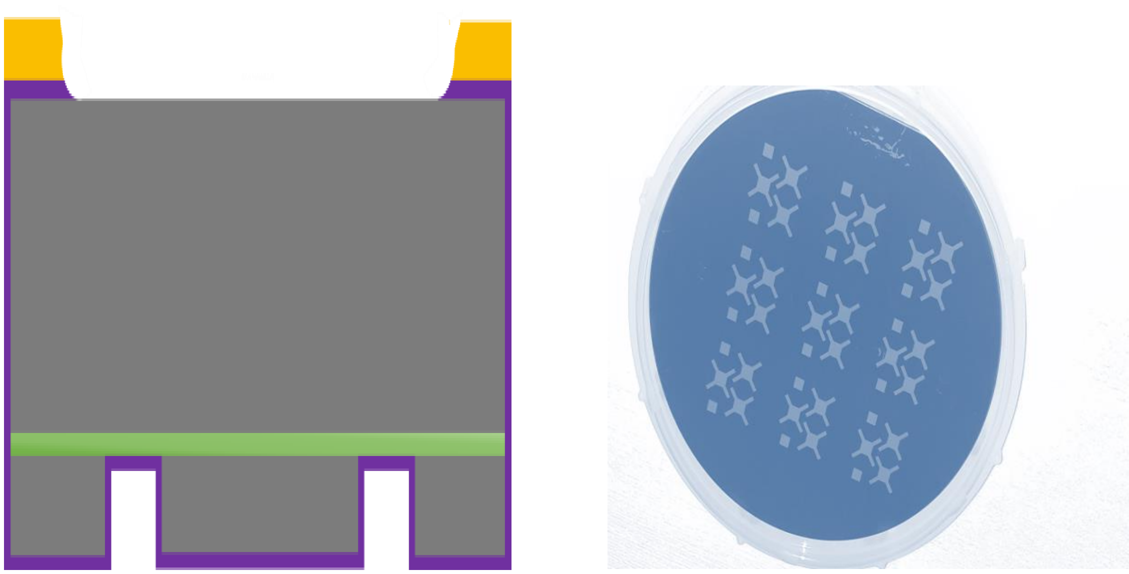

Figure 13. Schematic of back side photolithography and RIE.

3.2.5. Potassium hydroxide silicon etch

A Potassium hydroxide silicon etch is anisotropic wet etching method that was used to etch the bulk silicon handle wafer. A KOH bath with 50% concentrated potassium hydroxide at 80°C was prepared to etch the silicon wafers. The wafers are placed inside the bath and the actual etching starts when the solution starts bubbling. The wafers are etched in the <111> direction to form smooth surfaces, an advantage compared to dry etching technique [41]. While the sacrificial silicon nitride protects the device layer, portions of the handle wafer are etched with an etching rate about 65 μm/hr. A SOI wafer with ~ 500 μm thick handle wafer will need about 8 hours to finish etching. The overall redox chemical reaction associated with the potassium hydroxide wet silicon etch is given by:

$$Si + 2OH^- + 4H_2O \rightarrow Si(OH)_2{}^{++} + 2H_2 + 4OH^-$$

KOH wet etching, a slow etching process in which it is very hard to control the etching rate due to temperature fluctuations in the bath, still offers smooth etch profile at a very low price. This makes it popular and attractive in MOEMS processing [41]. The temperature of the potassium hydroxide etch bath apparatus is controlled by dialing the immersion heaters at the target temperature.

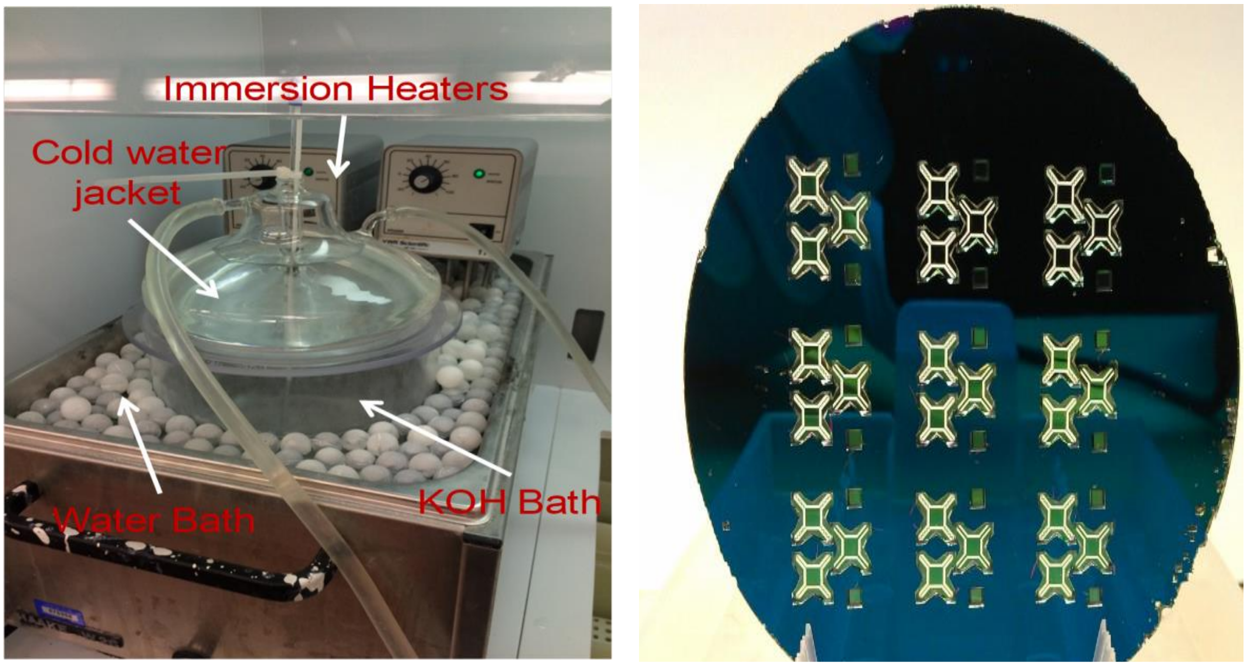

Figure 14. Left: KOH bath etch apparatus setup. Right: a wafer image after 8 hours of KOH etching.

As can be seen in Fig.14, the silicon nitride mask layer is in good condition after finishing the wet alkaline etching step.

3.2.6. Phosphoric acid and hydrofluoric acid etch

Hot phosphoric acid heated at 170°C was used to etch silicon nitride from the device and handle layers. The overall chemical reaction to etch the silicon nitride layer is given by:

$$3\mathrm{Si_3N_4} + 27\mathrm{H_2O} + 4\mathrm{H_3PO_4} \rightarrow 4(\mathrm{NH_2})_3\mathrm{PO_2} + 9\mathrm{H_2SiO_3}$$

The silicon nitride wet etching is isotropic and has an etch rate ~ 4 nm/min.

Hydrofluoric acid wet etching was used to etch silicon-dioxide and release the movable membranes, allowing the x-beams to hang freely with the handle wafer providing structural support. The overall chemical reaction of hydrofluoric wet etching is given by [5, 126]:

$$Sio_2 + 6HF \rightarrow H_2SiF_6 + 2H_2O$$

An image of the movable x-beams chip is shown in Figure.15 below. The active square region for all three x-beams measured 2 mm x 2mm. The arm lengths of x-beams 1 and 2 were rigid and it has length of 1.9 mm each, whereas the widths of these arms were 0.1 mm and 0.25 mm respectively. And x-beam 3 was designed with ten meanders, each segment being 0.25 mm x 0.075 mm, it has arms of length 3.625mm.

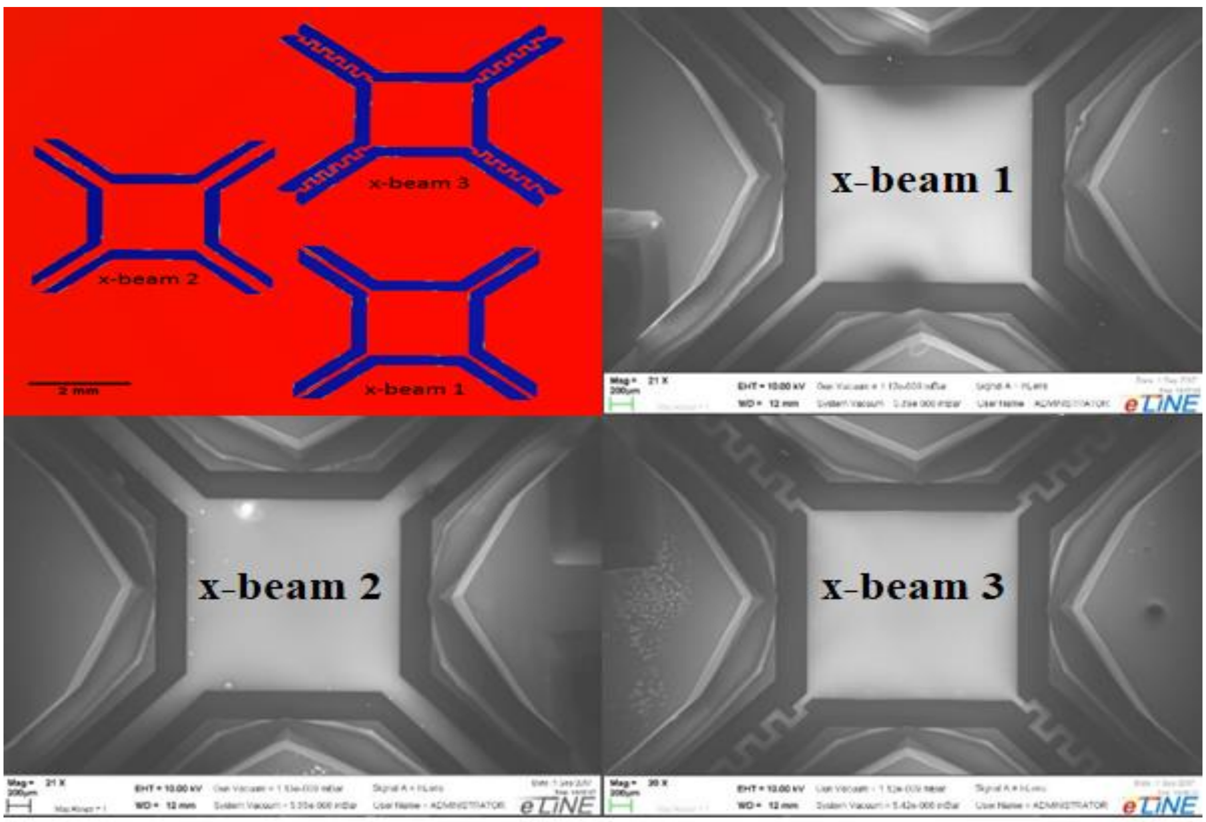

Figure 15. Optical and SEM images of the various x-beam designs. The arms and anchors attach to the unetched handle wafer providing structural support to the freely hanging beams. The surface areas of the three designs were 4.76 mm^2, 5.9 mm^2, and 4.75 mm^2 for x-beams 1, 2, and 3, respectively.

4. MOEMS-based micro-actuators

In this chapter, assembly of micro-actuators, spacer development, and various actuation mechanisms of MOEMS-based micro-actuators are discussed. The advantages and benefits of parallel-plate electrostatic actuation compared to other actuation mechanisms in tuning the micro-actuators are addressed.

4.1. Micro-actuator device assembly

The micro-actuator consists of a stationary bulk silicon wafer assembled with a movable x-beam chip placed on top. The two chips are bonded together using adhesive wafer bonding technique. A spacer made from a negative photoresist SU-8(3025) is spin-coated on the stationary bulk silicon and is meant to separate the chips, introducing an optical cavity that can later be reduced in thickness when electrostatic actuation is performed. Graphite-based conductive wire glue was used to attach electric output wires to the stationary and movable membrane chips, where the stationary bulk silicon is grounded, and the movable membrane is connected to a high voltage since its configuration is suitable for actuation.

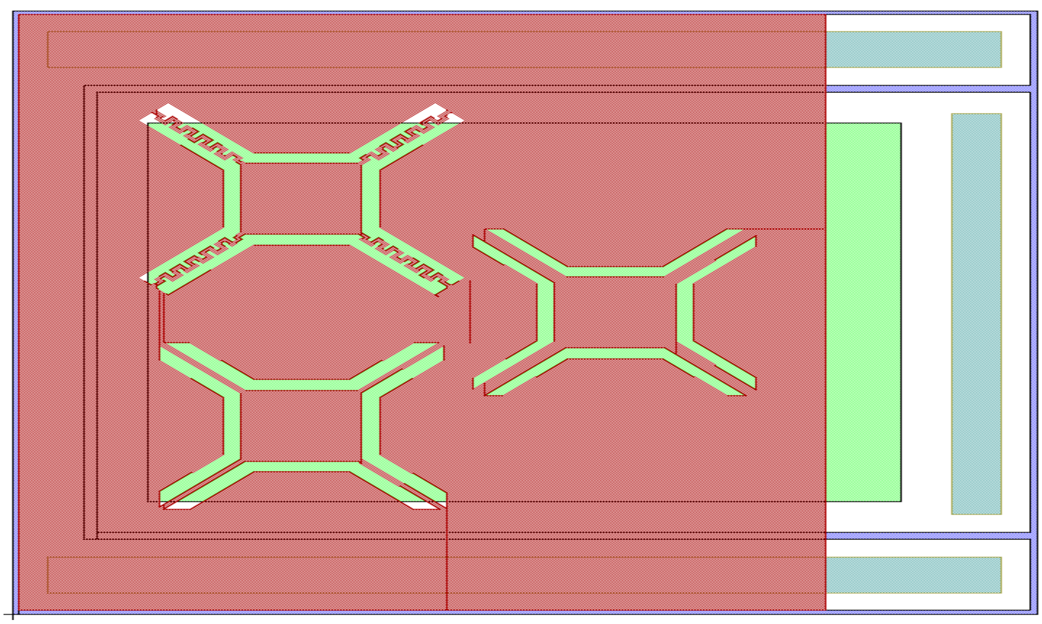

Figure 16. Schematic of the assembled micro-actuator

In the next section, the spacer layer development that includes deposition of SU-8 photoresist on the stationary bulk silicon wafer as well as the wafer bonding technique that is crucial for the realization of the micro-actuator is discussed.

4.1.1. Spacer layer deposition

SU-8 (3025), a negative photoresist that has many important features like high aspect ratio, reasonable film thickness & near UV processing, was chosen and spin-coated on the stationary membrane [45]. The fabrication of the spacer layer involves three main steps: surface preparation, patterning the spacer layer with photolithography, and wafer bonding. The silicon wafers were prepared by cleaning the substrates with 25% concentrated piranha solution with 1:4 H_2SO_4: H_2O_2 to remove organic residues. The substrates were then dehydrated at 140°C for ~10 mins to promote their adhesion with a photoresist [46]. After treating the surface of the substrate, the photolithography process to fabricate the SU-8 spacer involved spin-coating the photoresist on the substrate, and pre-bake the photoresist to remove the solvents. Next comes exposing with ultraviolet light at various exposure doses, which depend on the requirements of the film thickness and bond strength. SU-8 photoresist needs post-exposure baking after exposure, which affects its cross-linking. The exposed wafers were then developed using SU-8 developer [45, 46].

Various wafers were processed under different conditions by changing the processing parameters like spinning speed & time, pre-baking conditions, exposure dose and post-exposure bake conditions to achieve the target photoresist thin film thickness.

4.1.2. Adhesive wafer bonding

Wafer bonding allows the fabrication of different microstructures like fluidic sensors, integrated circuits and microfluidics. Fabrication of SOI wafers, a starting material for many MOEMS devices nowadays, is one of the major applications of wafer bonding. There are various types of wafer bonding techniques, like direct bonding, soldering, ultrasonic and adhesive wafer [47, 48].

Adhesive wafer bonding is a technique that utilizes an adhesive polymer to glue different wafers. In this technique, an intermediate insulating SU-8 adhesive layer is applied and deposited on the mechanical layer of stationary bulk wafer. The SU-8 adhesive provides forces to the micro- to stick together. This technique was chosen since it offers the advantages of lower cost, absence of electric voltage and current, and lower temperature processing usually < 250 ^{O}C [47].

When an adhesive polymer is used to bond the micro-chips, it deforms to fit the surfaces of the micro-chips. The SU-8 photoresist was used to wet and glue the micro-chips. The adhesive polymer must be hardened to bring a force and attach the micro-chips [45, 47]. The surfaces of the wafers should be wet by an adhesive polymer and it is crucial step in adhesive bonding method. To wet the surface of a wafer, it should have a surface energy that is greater than the surface energy of the adhesive polymer [49].

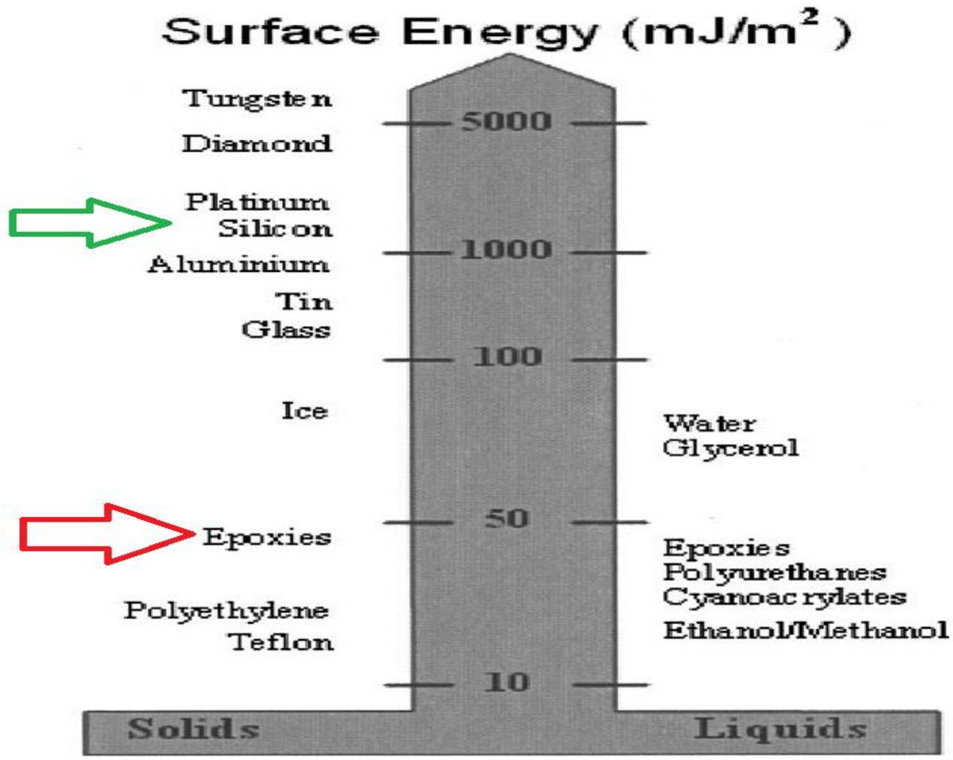

Figure 17. A chart of surface energy of various materials [49].

The surface energies of various solids and liquids are listed in Figure. 17. The silicon wafer has higher surface energy compared to the SU-8 epoxy; hence the SU-8 photoresist can properly wet a silicon wafer [43]. The degree of wetting is affected by the surface contaminants. In this work, a clean surface is achieved by treating it with Piranha solution prior to photoresist processing.

The adhesive wafer bonding was done by applying pressure to the micro-chips while baking them on a hot-plate by varying the temperature of SU-8 photoresist [45, 47]. It is known that the pre-baking temperature, baking time, exposure dose, post-exposure baking temperature, and applied pressure are the main parameters which affect the wafer bonding strength between the stationary and movable membranes.

The adhesive wafer bonding experimental set up was designed to optimize the bond strength of the wafers. The bonding was performed by applying pressure, while the samples sit on the hot plate by varying temperature as shown in Figure. 18.

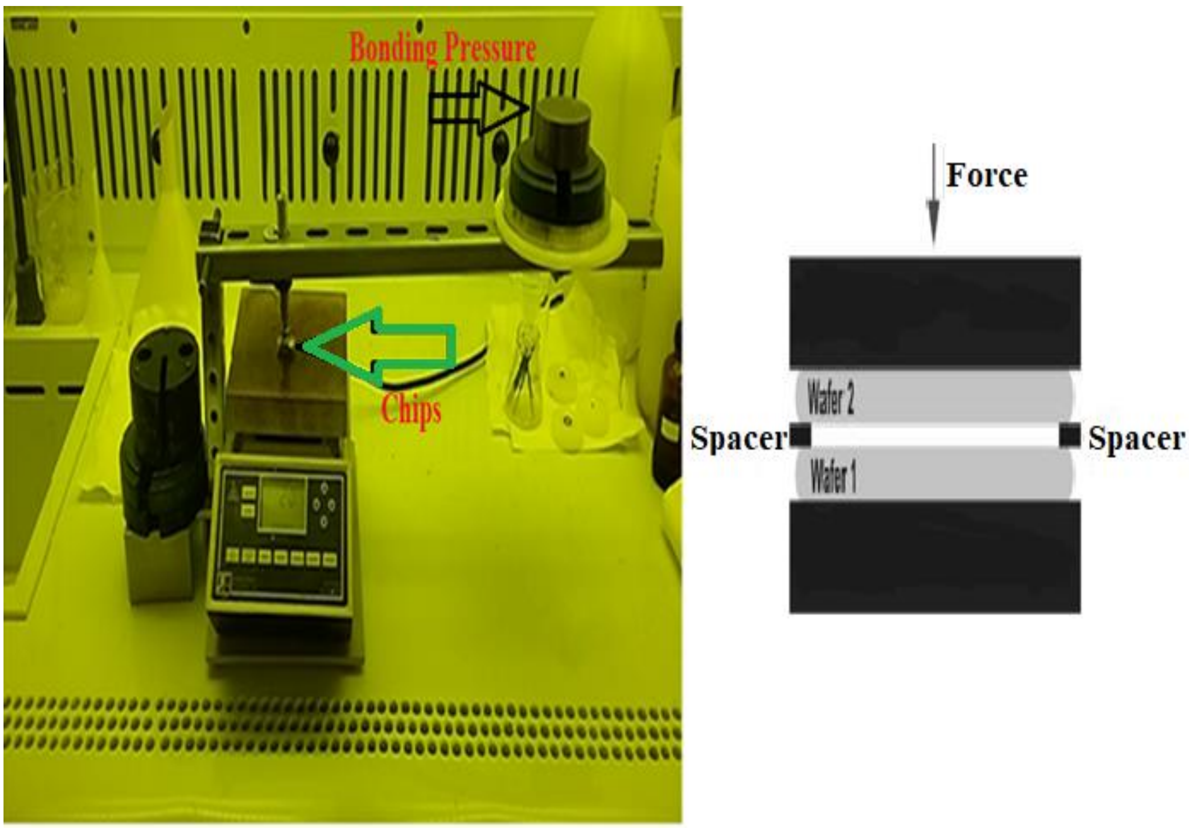

Figure 18. Experimental setup of adhesive wafer bonding

Here are some of the details about the design of the adhesive wafer bonding experimental setup:

i) A teflon block which has the same size as the movable membrane of size 1.3cm x 1.7 cm, was designed with center of mass, $\boldsymbol{r_{cm}} = 0.51cm\vec{\imath} + 0.83cm\,\vec{\jmath}$. The center of mass of the teflon block was designed to coincide with the center of mass of the spacer cavity layer to ensure that pressure is uniform across the micro-actuator.

ii) A home-made lever system which multiplies the force applied on the sample stack was designed, and a maximum pressure of 2.85 MPa was applied on the microchips.

The bonding was done by varying different key parameters. The bonding parameters and bonding strengths are shown in Table III below.

Sample No.	SU-8 Thickness (µm)	Pressure (MPa)	Baking Temperature ($°C$)	Exposure Dose (mJ/cm^2)	Baking Time (minutes)	Bond Strength (KPa)
1	12	1.74	ramp $55 \rightarrow 145$	145	60	224.4
2	12	2.84	ramp $55 \rightarrow 145$	150	60	360
3	12	2.57	ramp $55 \rightarrow 145$	140	60	565
4	12	2.85	ramp $55 \rightarrow 145$	130	60	685
5	12	2.85	ramp $55 \rightarrow 145$	110	60	1100

Table III: Adhesive wafer bonding process parameters and results.

In this work, the adhesive wafer bonding was performed with the following specific procedure. While applying a constant bonding pressure of 2.85Mpa, the bonding temperature of the micro-chips was varied in the following sequence:

i) The microchips were held at 55°C for 5 minutes.

ii) The temperature of the microchips was then ramped from 55 °C $\rightarrow$ 65 °C, with a ramping speed ~ 5 °C/min and was held at 65°C ~ 5 minutes.

iii) Finally, the temperature was changed from 65 °C $\rightarrow$ 145 °C, with ramping speed ~ 10°C/min and was held at 145°C for ~ 40 minutes.

After bonding the wafers with this technique, the bonding strength was tested using a pull test method with a pull sensor. Once the microchips were bonded, wax was melted at 100°C and a clamp that fits with the pull sensor was stuck on. The force applied on the top silicon chip was measured by reading the amount of total weight needed to de-bond the microchips. we achieved a maximum bond strength of ~ 1.1 MPa as listed in Table III.

Figure 19. Experimental set up of pull-test.

In this study, the post-exposure baking temperature was the low value of 55°C since it is understood that a low post-exposure temperature will inhibit hardening of the intermediate negative photo-resist layer, and it enhances softening of SU-8 thin film, which can facilitate the bonding between the micro-chips. It was also verified the bonding temperature, pressure, baking time and thickness of the photoresist layer play roles in affecting the bond strength of the assembled chips during the adhesive wafer bonding process [47].

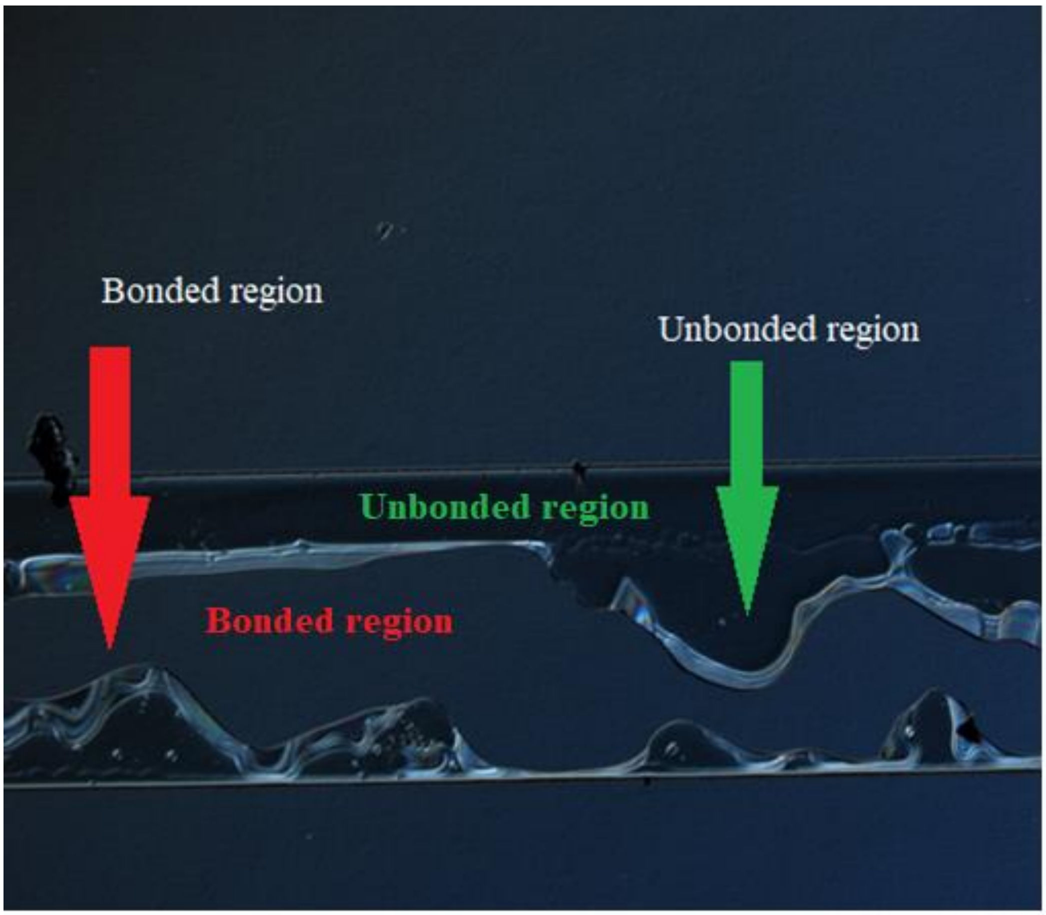

Figure 20. An optical microscope image of a stationary membrane after debonding.

The de-bonded stationary membranes were investigated by an optical microscope, and it was seen that bonded and unbonded areas occur at the bonding interface between movable and stationary membranes. Some portion of the adhesive polymer at the stationary membrane has been transferred to the movable membrane as can be seen in Figure. 20. The bonded portion at the interface offers the required bonding strength to hold the micro-actuator together.

4.2. Actuation mechanisms of MOEMS-based micro-actuators

Various types of actuation methods, including electromagnetic, piezoelectric, electrostatic, and thermal, have been used to achieve reasonable displacements of micro-actuators [50, 51].

Electromagnetic actuation usually uses a magnetic coating ferromagnetic material to be deposited on a micro-actuator and an inductor coil beneath it to create a magnetic field that displaces the micro-actuator [51]. Electromagnetic actuation mechanism gives the largest actuation displacement compared to other actuation mechanisms, however, the higher power consumption and the challenge to deposit ferromagnetic material on the micro-actuator limits the realization of electromagnetic micro-actuators [52].

Piezoelectric actuation is a mechanism in which materials having charge asymmetry in the primitive unit cell, like ZnO undergoes either expansion or contraction in response to an applied external voltage. A small displacement and a high actuation voltage are the main limitations of the piezoelectric method [53].

The electro-thermal actuation mechanism utilizes the principle of thermal expansion when different materials with different thermal expansion coefficients are fabricated in forming bimetallic strip. When heat energy is applied, a micro-actuator with the strip will deflect. Though electro-thermal actuation has a simple fabrication process, the very slow response time and thermal fatigue limit its application [54].

The electrostatic actuation method uses an electrostatic force to displace the micro-actuator. This method usually causes mechanical motion through a capacitor system in response to an externally applied voltage. Electrostatic micro actuation is commonly used to construct different micro actuators since it offers fast response time, ease of fabrication with commercially available silicon wafers, and easy implementation [55, 56]. The micro-actuators in this study use the parallel plate electrostatic actuation method.

4.3. Parallel plate electrostatic actuators

Parallel plate capacitive electrostatic actuation is based on the accumulation of charge on two electrically separated, parallel membranes that make up a capacitor [57, 58]. A movable membrane plate is suspended with an elastic restoring force suitable for movement along the vertical z-axis while the bottom stationary plate is fixed in place [57]. When a voltage is applied across the membranes, charges of opposite polarity accumulate on the two separated surfaces, as shown in Figure. 17. The initial spacer distance, d is an important parameter since it gives information about the amount of voltage to be applied to the micro-actuator. When an external bias is applied, charge will be accumulated that later creates an electric force that will pull a movable plate toward the stationary bulk membrane. The generated electric force is given by [56]:

$$\mathrm{F}_{\mathrm{electrostatic}} = \frac{-\varepsilon_0 A}{2}\frac{\mathrm{V}^2}{(\mathrm{d}-\mathrm{z})^2} \tag{4.1}$$

where, d represents original spacing, A denotes the electrically and optically active area of movable membrane, z represents the distance moved by movable membrane, and V is an external applied bias. The displacement of the top movable membrane due to the attractive electric force creates a mechanical restoring force that acts in opposition to it [56, 57]. This is modeled as an attached spring and its mechanical resistive force follows Hooke's Law, which is given by:

$$\mathrm{F}_{\mathrm{mechanical}} = \mathrm{kz} \tag{4.2}$$

The parameter *k* represents the mechanical stiffness constant of the movable membrane. At equilibrium, the sum of all the forces acting on the micro actuator is zero. When the applied voltage is increased such that the equilibrium condition does not hold, the gap between the plates *d* will begin to gradually decrease [58]. This means that the electrostatic force will increase quadratically while the mechanical restoring force will increase linearly [57, 58].

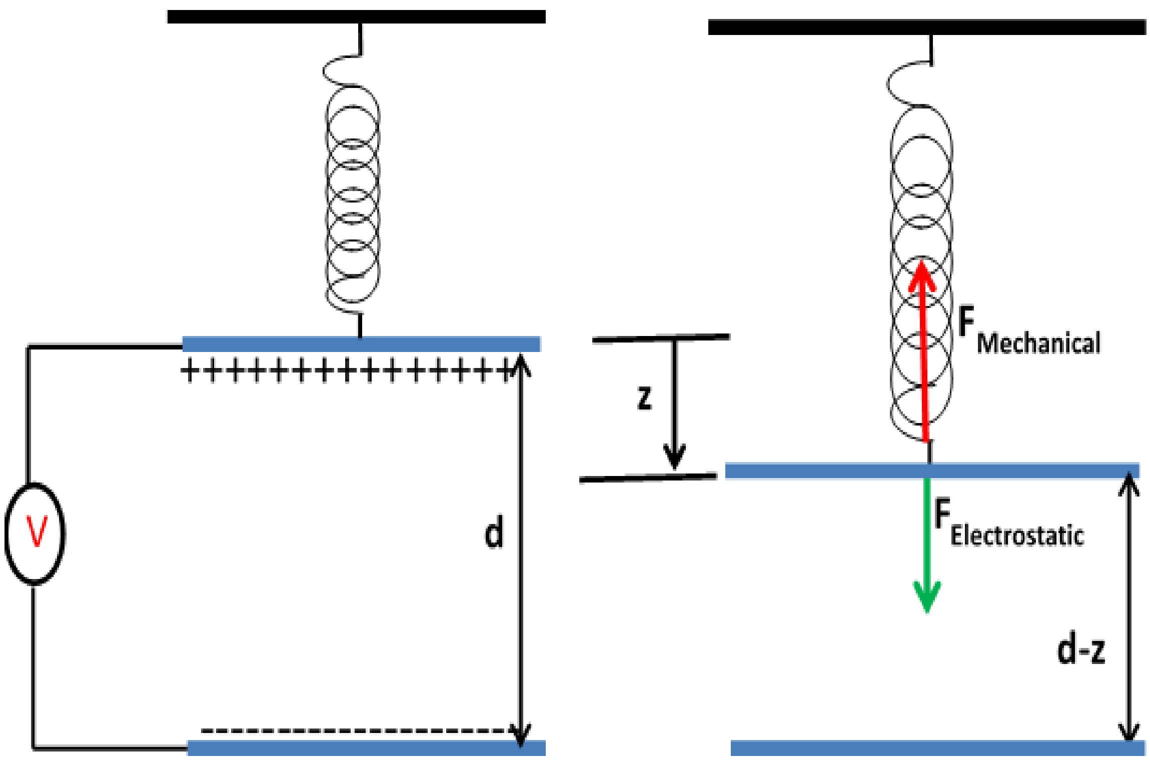

Figure 21. Model schematic of parallel plate electrostatic actuator. A movable top plate can be modeled with an attached spring representing the mechanical restoring force while the bottom plate is fixed. Application of a voltage causes displacement of the movable membrane, given by parameter z.

At some point, however, the electrostatic force will begin to dominate, resulting in the non-linear motion of the movable plate [59]. When the partial derivative of the total force is less than zero, this situation results in a term that gives the maximum stable linear displacement of the top movable plate [58, 60]. This condition is known as the "snap-in" point, and is given by,

$$z > \frac{d}{3} \tag{4.3}$$

The external bias voltage in which the plates become unstable is known as the "snap-in" condition and the bias associated to this condition is given by [58, 61]:

$$V_{snap-in} = \sqrt{\frac{8kd^3}{27\varepsilon_0 A}} \tag{4.4}$$

Beyond snap-in voltage, the actuator starts to show non-linear motion [58, 62]. Although the snap-in condition is a major limitation, parallel plate electrostatic actuation would potentially be most practical for integration with high-speed sensing devices in the military, space and commercial applications [57, 63].

5. DBRs

5.1. Introduction

DBRs are periodic structures of dielectric thin films commonly used to create broadband reflectors [64]. These mirrors are comprised of multiple layers of thin films with alternating refractive indices and optical thicknesses. The DBR is a one-dimensional photonic structure that is an important component in optoelectronic devices. The DBR mirror is incorporated in various optoelectronic devices, like Fabry-Perot optical filters, microcavity structures, switches, lasers, LEDs, and photodetectors. The mirrors offer several advantages, such as providing wavelength selectivity, improving the light extraction efficiency of emitters, and enhance light-matter interaction at the operation wavelength [64, 65].

The quarter-wave-optical thickness (QWOT)-based DBR mirror has been utilized in this work. It was chosen since it offers the advantages of simple design, ease of integration, and it eliminates post-growth processing [64, 66].

Theory of DBR mirrors, principle of operation, thin film growth techniques, the nature of the interfaces between the alternating dielectric thin films, and absorption mechanisms of multilayers will be discussed.

5.2. Principles of DBR operation

The DBRs work with the principle that light propagating from a lighter optical density medium to a higher optical density medium will undergo 180° (π) phase shift at the interface between the layers. The reflected light from each interface in the multilayer structure will also experience additional phase change that arises from the pathlength of light within each layer [67]. For the reflected waves to achieve high reflection, they should undergo constructive interference. To ensure all the reflected waves have constructive interference, the DBR layers should have a particularly designed thickness within each layer, which is commonly known as QWOT, and is expressed as [64, 67]:

$$d_H = \frac{\lambda}{4n_H} \text{ , and } \quad d_L = \frac{\lambda}{4n_L} \tag{5.1}$$

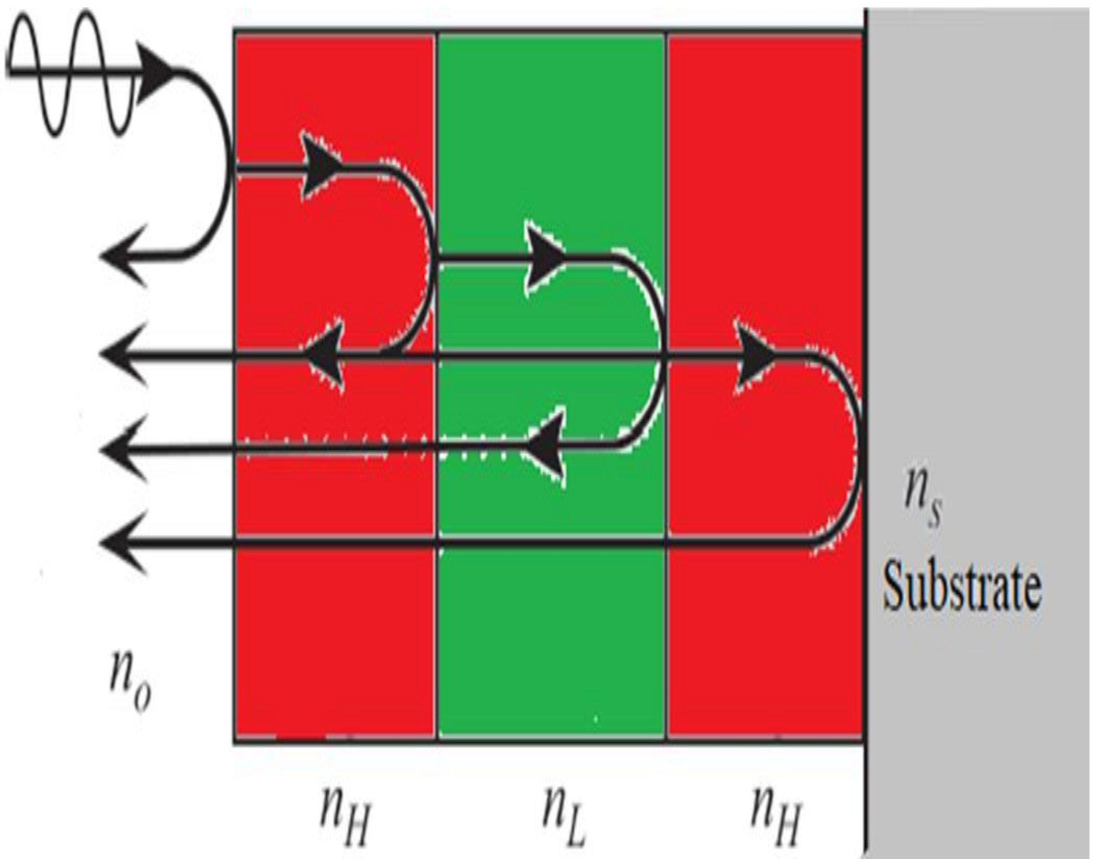

Figure 22. Schematic of DBR mirror

The reflection of the DBR mirror depends on stack numbers and value of $({n_H}/{n_L})$ between the dielectric materials. Because refractive indices of dielectric materials are wavelength dependent, the performance of the DBR mirror will be limited to a small wavelength width [68]. The reflection, R_N for a DBR is mathematically given by,

$$\mathrm{R_N} = \left[\frac{n_H{}^{2N+1} - \frac{n_O}{n_s} n_L{}^{2N+1}}{n_H{}^{2N+1} + \frac{n_O}{n_s} n_L{}^{2N+1}}\right]^2 \tag{5.2}$$

where n_0 and n_s represent the refractive indices for incident medium and substrate material respectively, n_H and n_L denote the refractive indices for dielectric materials that make up the DBR stacks.

The reflectivity also depends on the reproducibility of the layer thickness of multi-layers. The reproducibility of the DBR is usually checked by observing the spectral shape of the high reflection region, commonly called the stop band zone [67, 68].

5.3. Growth methods of dielectric thin films

Currently, various types of thin film growth methods are used to fabricate dielectric thin films on the substrate. The deposition technologies are classified into two different broad groups; namely physical vapor deposition and CVD. In the case of chemical vapor deposition, firstly the substrate is heated to a higher temperature, then very reactive chemical species can undergo chemical reaction near the substrate that later creates thin films that will be deposited on the substrate [69, 70]. The most commonly used CVD techniques nowadays include LPCVD, PECVD, and APCVD. In contrast, PVD technologies are physical in nature, meaning the source material is vaporized and transported through a vacuum environment towards the surface of the wafers and the vaporized material always condenses in forming a thin film [69, 71].

The deposition of thin films always involves many steps. When the dielectric source materials atoms are colliding on the substrate, the atoms undergo physical adsorption, nucleation, growth and ripening stages [72]. The atoms of the target materials interact with the newly arriving dielectric material atoms and there is an exchange of energy with the substrate atoms till condensation. The evaporated dielectric material atoms usually have high kinetic energy, and it loses enough energy during the collisions so that it can stick on the target material. After sticking, the source material atoms will form small grains, the grains will grow over the substrate to form clusters, and clusters will migrate over the surface of the substrate and interact with other clusters. The clusters usually keeps growing and coalescing until a continuous thin film is formed [73, 74].

The average thickness value when the thin film formation will start to be continuous is dependent on several factors. The main ones that should be considered are the rate of deposition, vacuum pressure of deposition chamber, and temperature of substrate [73, 74].

In this work, various compound semiconductor thin films that are important components of the DBRs were grown by the electron beam deposition technique. In Chapter 7, this thin-film deposition method is discussed in detail.

5.4. Absorption theory of infrared multilayers

The optical absorption properties of infrared multilayers are manifestations of the interaction of electrons and nuclei of a semiconducting material with the incident electromagnetic radiation. This interaction provides an excellent tool for probing the microscopic absorption characteristics of the DBR multilayers [75]. The optical absorption characteristics in the infrared region are subdivided into electronic and lattice properties. Electronic absorption mechanism depends on the band structure of the materials that are mainly affected by the crystallography, type of bonding and the atoms in the semiconductor material. On the other hand, lattice absorption always involves lattice vibrations, namely a phonon [75, 76].

In the next sections, the major absorption mechanisms present in the MWIR region that can be categorized into three fundamental processes, namely; electronic absorption, phonon absorption, and free carrier absorption are discussed.

5.4.1. Electronic absorption

Electronic absorption is an inter-band absorption mechanism where a charge carrier usually electron absorbs light and transit from a lower energy band to a higher energy band [77]. Electronic absorption is one of the dominant absorption processes in the infrared region and it occurs when an infrared signal interacts with the charge carriers of the semiconducting material [77, 78].

If an incident electromagnetic radiation has larger energy than electronic band gap of the material, then it will be absorbed by exciting a charge carrier from a lower energy band to a higher energy band [78]. Electronic absorption serves to define the short wavelength transparent edge of the material. This absorption edge is always referred to as the cut-off wavelength and it occurs at

$$\lambda_{\mathrm{cutoff}} = {}^{1.24\ \mathrm{ev}}/_{\mathrm{E_g}} \tag{5.3}$$

where $\lambda_{\mathrm{cutoff}}$ represents the on-set of the transparent edge, and E_g denotes the gap energy of semiconducting material.

Very smaller change as small as a fraction of electron-volt of energy near the band gap of the infrared material can alter the material from being optically transparent to completely opaque [77, 78].

Optical band to band transitions in semiconducting materials should satisfy both momentum and energy conservation laws in between initial and final states [79]. The electronic band absorption are categorized into vertical and nonvertical transitions. In vertical optical transitions, such as the case of GaAs, the charge carrier is usually excited by absorbing only a photon, excited charge carrier only changes its state of energy, and its momentum is unchanged to within the photon momentum [79, 80]. Whereas in the case of non-vertical optical transitions, like the case of silicon, a minimum energy band gap occurs between electronic states with different values of wave vector **k**, and a photon does not possess enough momentum to ensure the conservation of momentum for such a transition. A few additional processes however can provide the necessary extra momentum to affect the indirect transition [79]. The most general of these involves phonons. The overall conservation of energy becomes: $E_f = E_i + h\nu \pm E_{phonon}$, the plus and minus signs refer to phonon absorption and phonon emission respectively [79, 80].

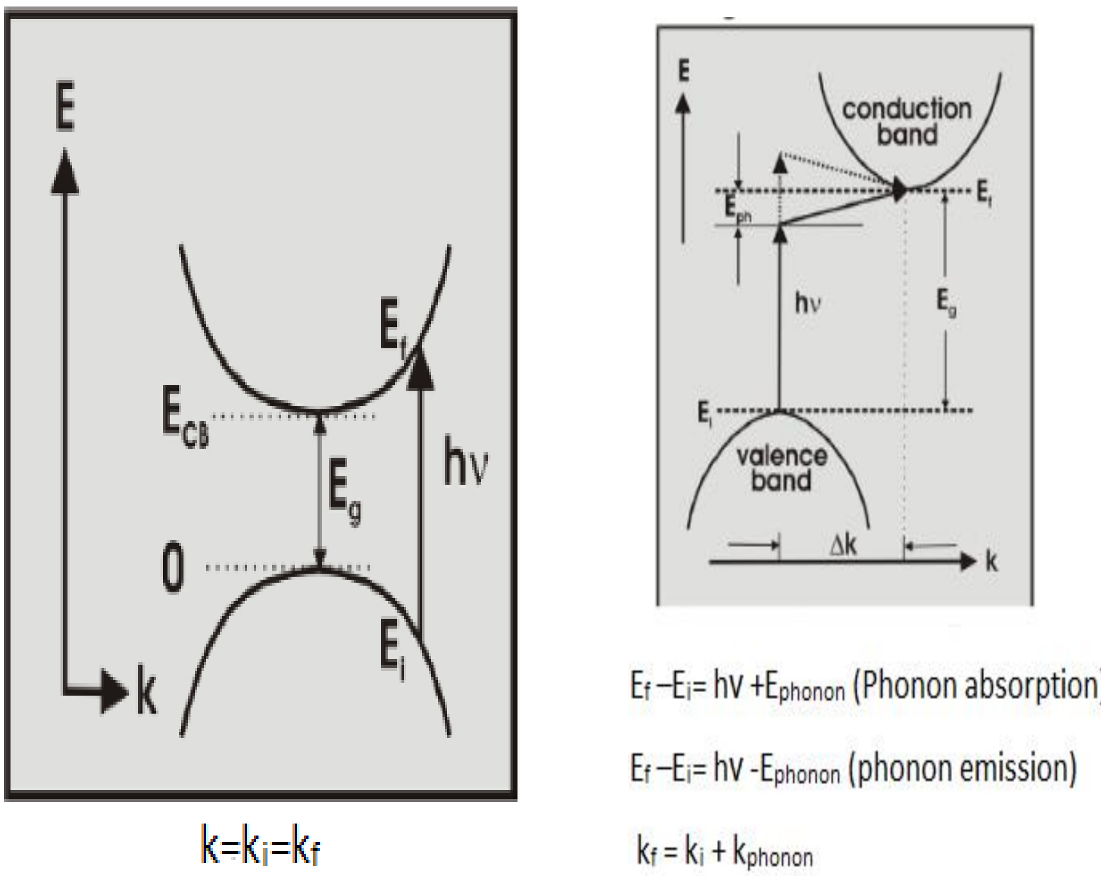

a) Vertical optical transition b) Non-vertical optical transition

Figure 23. Electronic band absorption of semiconductors [80].

5.4.1.1. The optical joint density

The photon absorption in a semiconductor corresponds to an optical excitation of electron in two distinct bands. Most often the optical transition is initiated by photons with a certain energy [81]. The optical joint density of inter-band transition is approximately expressed as:

$$J_{cv} = \frac{2}{(2\pi)^3}\frac{d}{d(h\nu)}\left[\frac{4\pi}{3}k^3\right] \tag{5.4}$$

where, J_{cv} is the optical joint density and **k** represents associated wave vector.

The optical joint density is estimated from a parabolic approximation of these two bands as [81, 82].

$$E_c(k_c) - E_v(k_v) = h\nu \tag{5.5}$$

where, $E_c(k_c) = E_c(k_{minimum}) + \frac{\hbar^2k^2}{2(m_e{}^*)}$, $E_v(k_v) = E_v(k_{maximum}) - \frac{\hbar^2k^2}{2(m_h{}^*)}$, and $E_c(k_{minimum}) - E_v(k_{maximum}) = E_g$

Hence Eq. 5.5 can be modified as:

$$h\nu = E_g + \frac{\hbar^2k^2}{2(m_r{}^*)} \tag{5.6}$$

where E_g denotes the band gap of the semiconducting material and $m_r{}^*$ represents the reduced carrier mass.

Solving for wave vector, **k** from Eq. 5.6 and inserting it into Eq. 5.4, we obtain the expression for the joint density of states [81, 82]:

$$J_{cv}=\frac{2(m_r{}^*)^{\frac{3}{2}}}{\hbar^3}\sqrt{h\nu - E_g} \tag{5.7}$$

The above expression (eq. 5.7) defines and gives information about available states in the bands to interact with a photon, and for an optical band-to-band transition, the incident photon requires at least energy, $h\nu \geq E_g$ [81].

5.4.2. Lattice absorption

Lattice absorption occurs as a result of the coupling between the incident light and lattice vibrations of the constituent atoms in the crystal. Lattice vibrational motion always produces traveling waves in which localized regions of the atomic vibration travel through the lattice [81, 83]. If we consider it from a quantum point of view, the energy levels in a quantum mechanical oscillator are discrete. And the quanta of these oscillations is named phonon [83].

Energy absorbed by lattice atoms when it interacts with the incident radiation is usually converted to the vibration and oscillation of the atoms. In complex lattice structures, for a mode of vibration to absorb any incident radiation there should exist a coupling mechanism [84, 85]. The main lattice absorption mechanisms are categorized into:

i) Single phonon Reststrahl absorption that occurs in ionic crystals, such as, ZnSe and BaF_2 is caused by single phonon absorption in the lattice. The one-phonon absorption process is related to the electrostatic attraction of opposite charges that produce an electric field which couples with the incident radiation [84].

ii) Multi-phonon absorption that occurs in polar covalent crystals such as, Ge when two or more phonons interact with the crystal and produce an electric dipole moment that couple with the incident radiation.

The lattice absorption characteristics are observed in the long wavelength region and define the long wavelength transparency limits of materials [83, 85].

5.4.3. Free-carrier absorption

It is an intra-band absorption process in which a charge carrier absorbs light and excites itself to another higher level in that same band [86]. This optical absorption process does not create electron-hole pairs [87]. Transition of a free carrier is always accompanied by a momentum-conserving process. When the photon is absorbed by an electron (hole), simultaneously a momentum conserving process will undertake place by either emitting or absorbing a phonon [87, 88]. The free carrier absorption phenomenon is an extrinsic absorption process which usually occurs as a result of heavy doping, unintentional dopants and impurities [86, 87]. This absorption mechanism has a higher contribution in the case when incident photon has an energy that is well comparable with the band gap of the material, and in a case where electronic band absorption is very weak [87, 89].

Free carrier absorption usually has drawbacks and it degrades the optical transmission and spectral resolution of optoelectronics, like Fabry-Perot optical resonators, microcavities, infrared photodetectors and photovoltaic devices [90, 91]. It is well studied in the literature that this absorption mechanism lies in between the electronic absorption edge and lattice absorption edge [91].

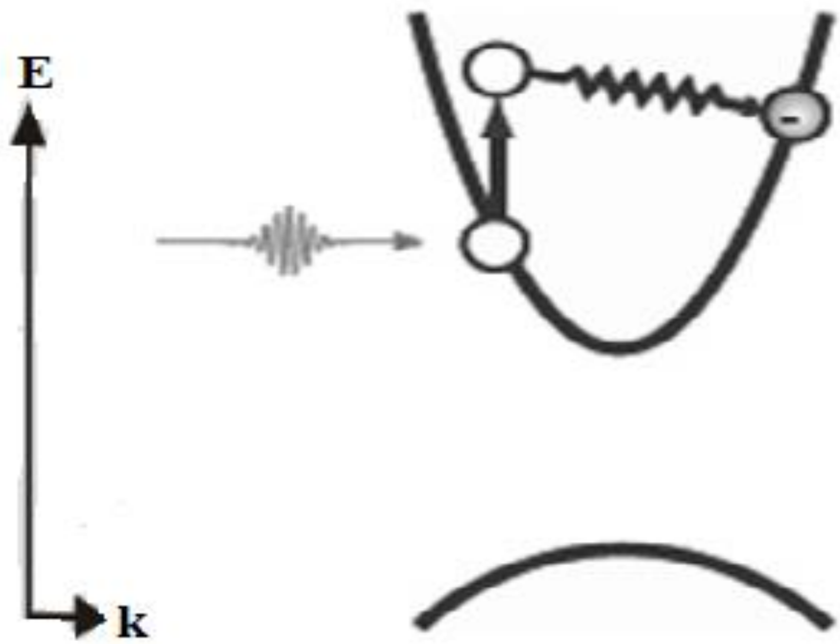

Figure 24. Schematic of free carrier absorption in the conduction band [79].

6. Results and discussion

6.0. Mechanical analysis of MOEMS-based micro-actuators

In this chapter, the experimental set up of the electrostatic actuation test using an optical profilometer, and the electromechanical characterization of micro-actuators with an emphasis on the mechanical data analysis will be discussed. The Least square fitting technique is also utilized to compare the experimental data with the curve fitting. Various micro-actuator x-beam designs were explored, and a serpentine design that can achieve higher sensitivity and compatible with CMOS technology is recommended.

6.1. Experimental set-up

The investigation of the mechanical performance of MOEMS microstructures demands a means to measure 3D profiles to accurately record the displacement of the micro-actuator under an applied external bias. White light interferometery, a non-destructive technique was applied to investigate the surface profiles of the MOEMS micro-actuators [92]. A schematic overview of the white interferometery and the actuation test setup is shown in Fig. 25.

The incident radiation comes from from a white light source, anf the incident radiation is splitted by a beam splitter as shown in Fig. 25. The lights that reflect back from the stationary mirror in the microscope objective and the movable mirror, in this case from the micro-actuator, will combine to form an interferogram which is detected by a CCD sensor. A transducer is used to translate the interferogram during measurement.The processed interferograms usually form a 3D image of the surface of the micro-actuator [92].

The electromechanical characterization on the assembled micro-actuators was performed by applying a voltage using a Keysight B2962A power supply, and a Bruker Contour GT-K optical profilometer was used to collect the displacement data by scanning the electrically active area of the micro-actuator for various spacer thicknesses. A Bruker GT-K optical profiler was chosen because it gives a high-resolution three-dimensional surface measurement in the vertical shift interference (VSI) mode. The VSI mode is one of the latest technologies developed at Veeco, and is capable of measuring the topography of samples to a maximum of 1 mm. Hence, the VSI mode is suitable to characterize the micro-actuators [92].

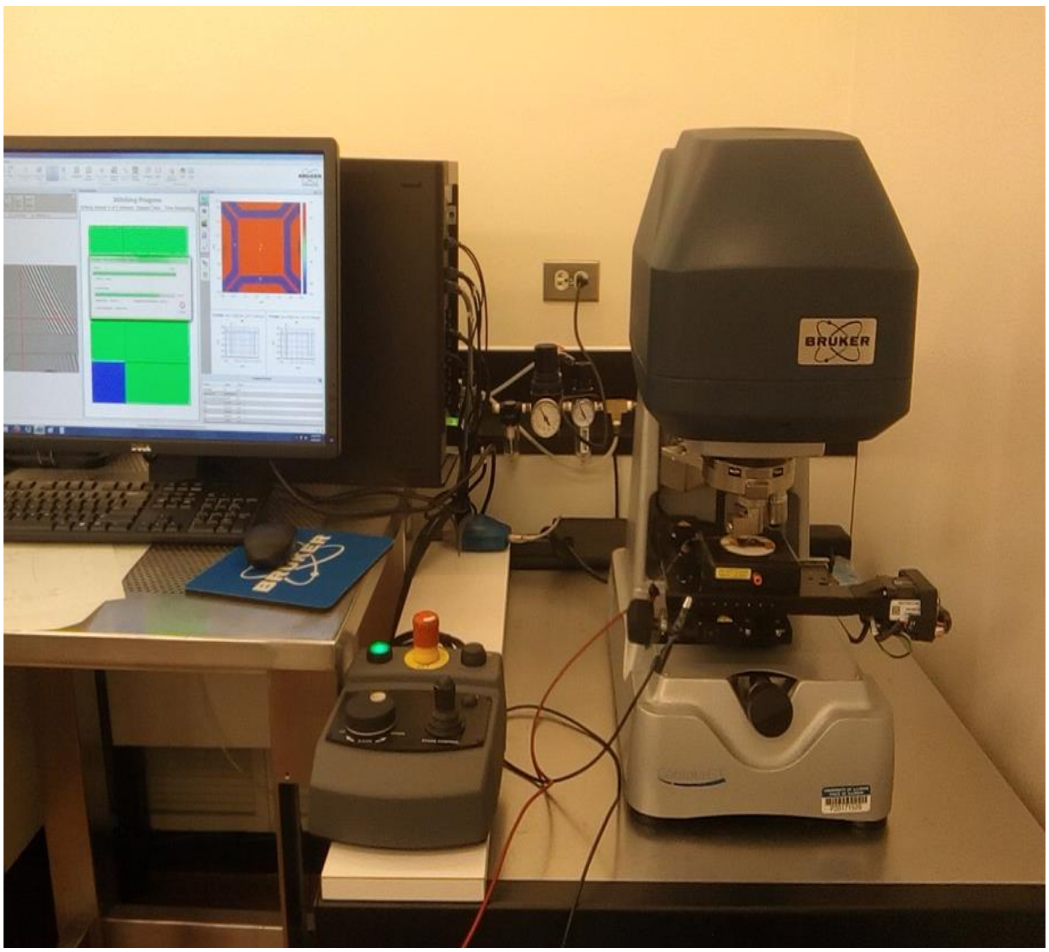

(a)

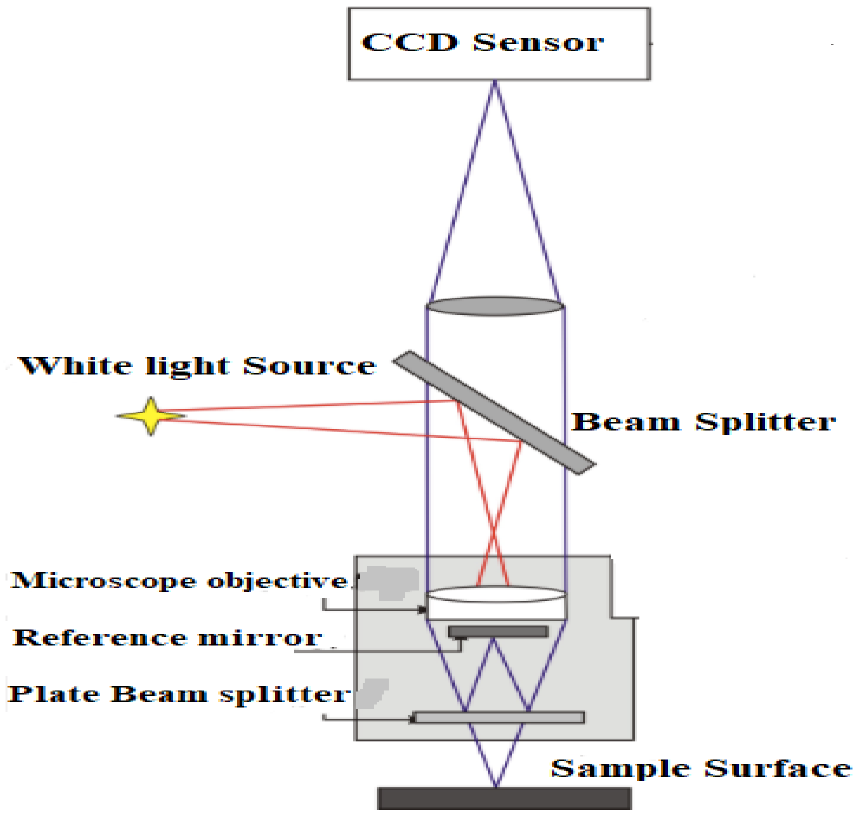

(b)

Figure 25. (a) Actuation setup with a Bruker Contour GT-K optical profilometer. (b) Schematic of white light interferometer [92]. The micro-actuator sits on the stage while a voltage is applied, and the scan is performed.

6.2. The electromechanical characterization of parallel plate electrostatic micro-actuator

The parallel-plate electrostatic micro-actuation measurement was used in this study as a principal technique to characterize the electromechanical performance of various micro-actuators. The micro-actuation displacement and sensitivity (d/V) were the main parameters of interest to be obtained from this technique. In this section, we will explain the electromechanical data analysis.

The electromechanical test was performed by measuring the initial spacing between the movable membrane and stationary bulk chips at 0 VDC and was then measured for every subsequent voltage applied to the micro-actuator. The scan data was split into x and y profiles for ease of analysis. The active area in the middle portion of the x and y profiles is shown below. The micrographs below represent x-beam 3 designs.

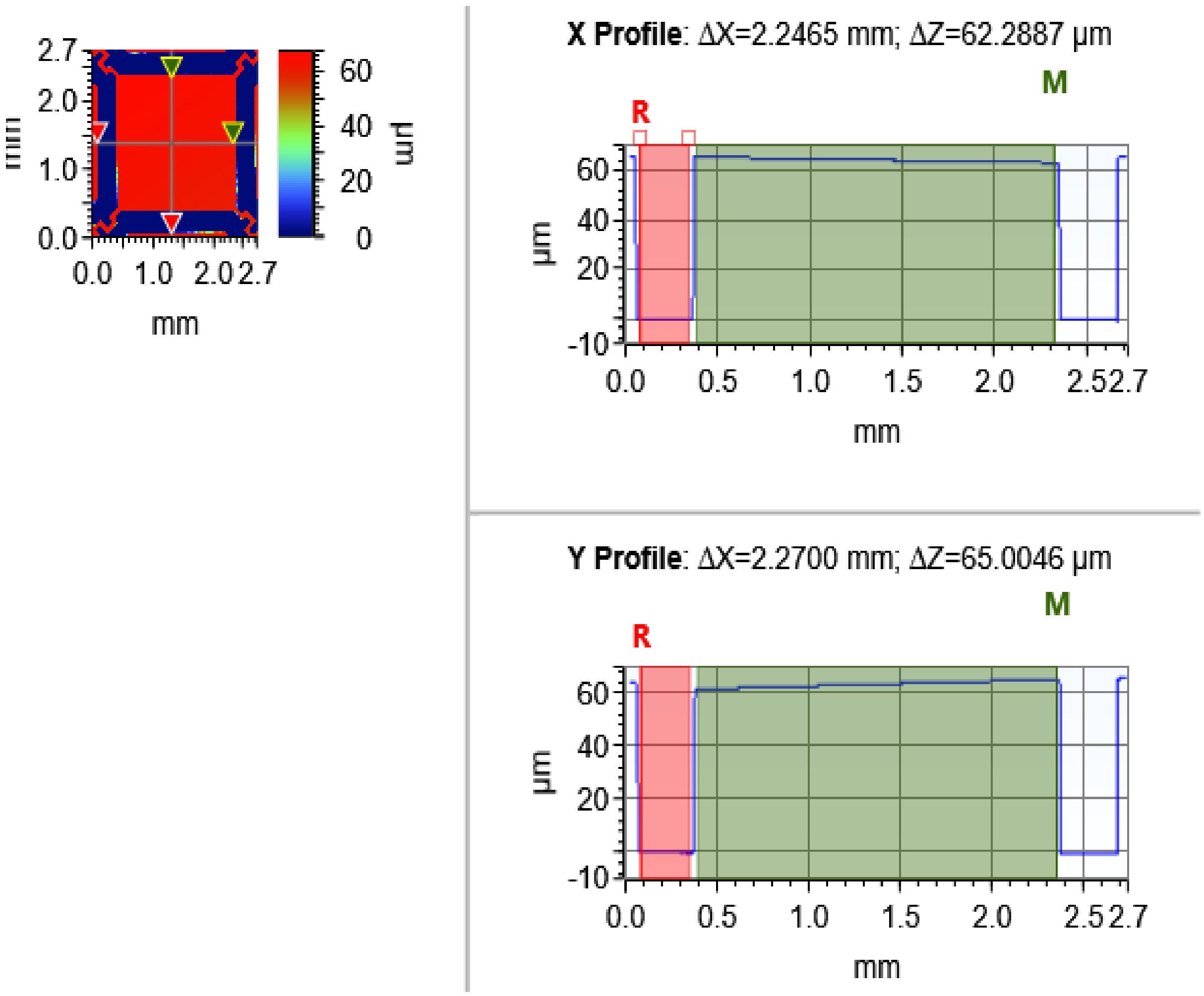

(a)

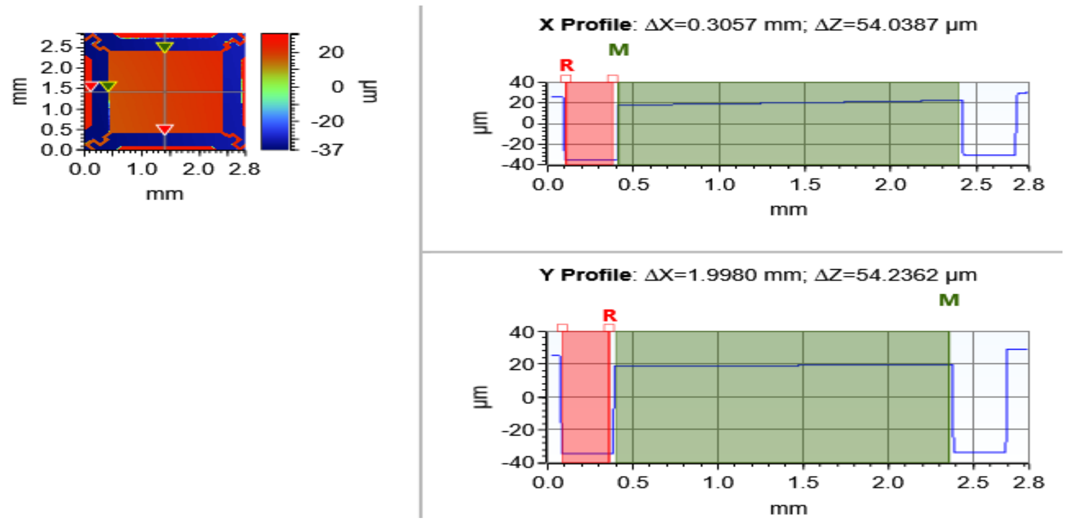

(b)

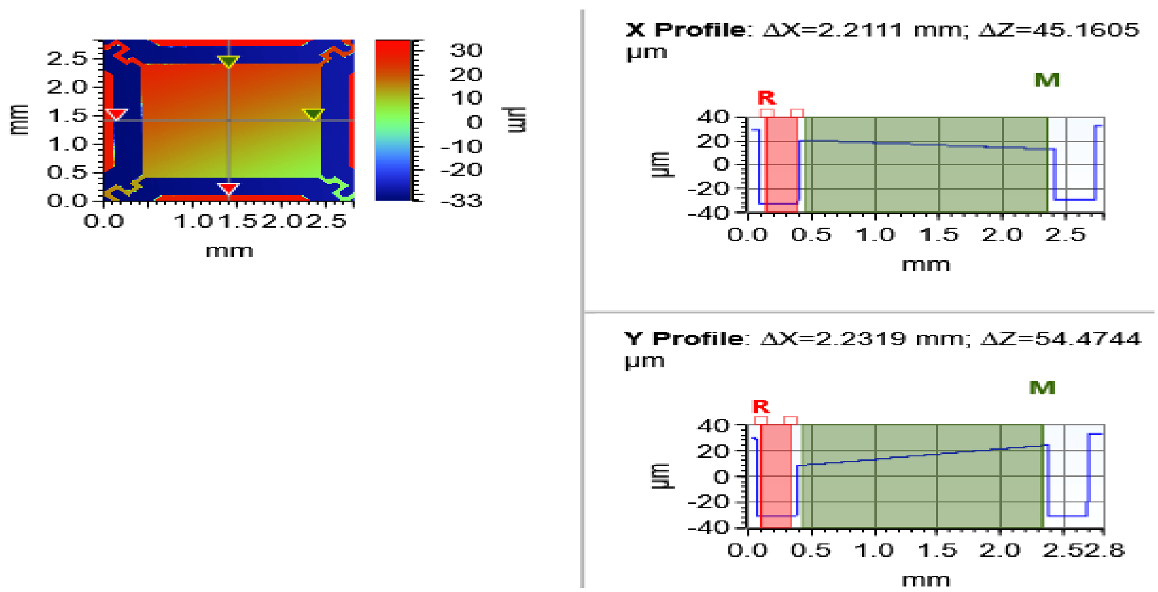

(c)

Figure 26. X-Y profile scans of the displacement of micro-actuator at 0 VDC (a), 128 VDC (b), and 129 VDC (c). The scan includes the 30 μm device layer. b) shows the spacer thickness has decreased indicating the x-beam has moved from its original position in (a). c) shows scan of the same x-beam, once displacement has exceeded the snap-in condition. The x-beam's displacement is non-uniform and unstable at an applied voltage of 129 VDC.

In Fig. 26(b), the x-beam is clearly shown to have deflected from its initial spacing at 0 VDC by approximately a third of the initial gap at 128 VDC. Beyond this voltage, the x-beam shows non-uniform and unstable displacement since the condition stipulated in Eq. (4.4) has been surpassed. Fig. 26(c) shows a scan of the x-beam for a ~33 µm spacer after it exceeds the snap-in condition for a voltage of 129 VDC. The displacement is clearly non-uniform since the x-profile of the scan has displaced 9.31 µm more than the y-profile. It can also be seen that the membrane tilt has become exaggerated compared to Fig. 26(b).

Two different spacer thicknesses were used to test each x-beam chip design to study the sensitivity and the mechanical stiffness constants. In this thesis three different x-beam designs were used. The square region for all three x-beams has a dimension 2 mm x 2mm. The arm lengths of x-beams 1 and 2 were rigid and it has length of 1.9 mm each, whereas the widths of these arms were 0.1 mm and 0.25 mm respectively. Whereas x-beam 3 has arms with ten meanders, each segment being 0.25 mm x 0.075 mm, the total arm lengths of x-beam 3 was 3.625mm. Fig. 27 shows the displacements of all three x-beams versus the applied voltage. We can see from the inset in Fig. 27b that for a ~27 µm spacer thickness, x-beam 2's displacement was ~7.2 µm even at the power supply limit of 210 VDC. This contrasts with both x-beams 1 and 3 in Figs. 27a and 27c, respectively, whose displacements approached the one-third limit at much lower voltages for similar spacer thicknesses. This indicates that x-beam 2's mechanical stiffness constant is much larger than the other two designs since it did not reach its snap-in condition. As a result, smaller average spacer thicknesses of ~13.6 µm and ~19.25 µm were used.

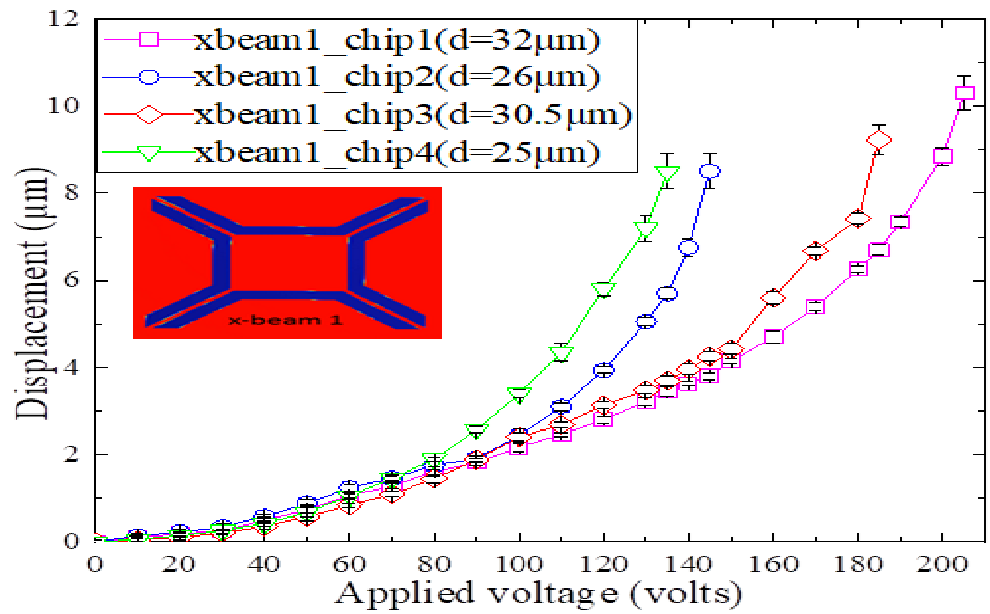

xbeam1_chip1(d=32µm)
xbeam1_chip2(d=26µm)
xbeam1_chip3(d=30.5µm)
xbeam1_chip4(d=25µm)
x-beam 1
Displacement (µm)
Applied voltage (volts)

(a)

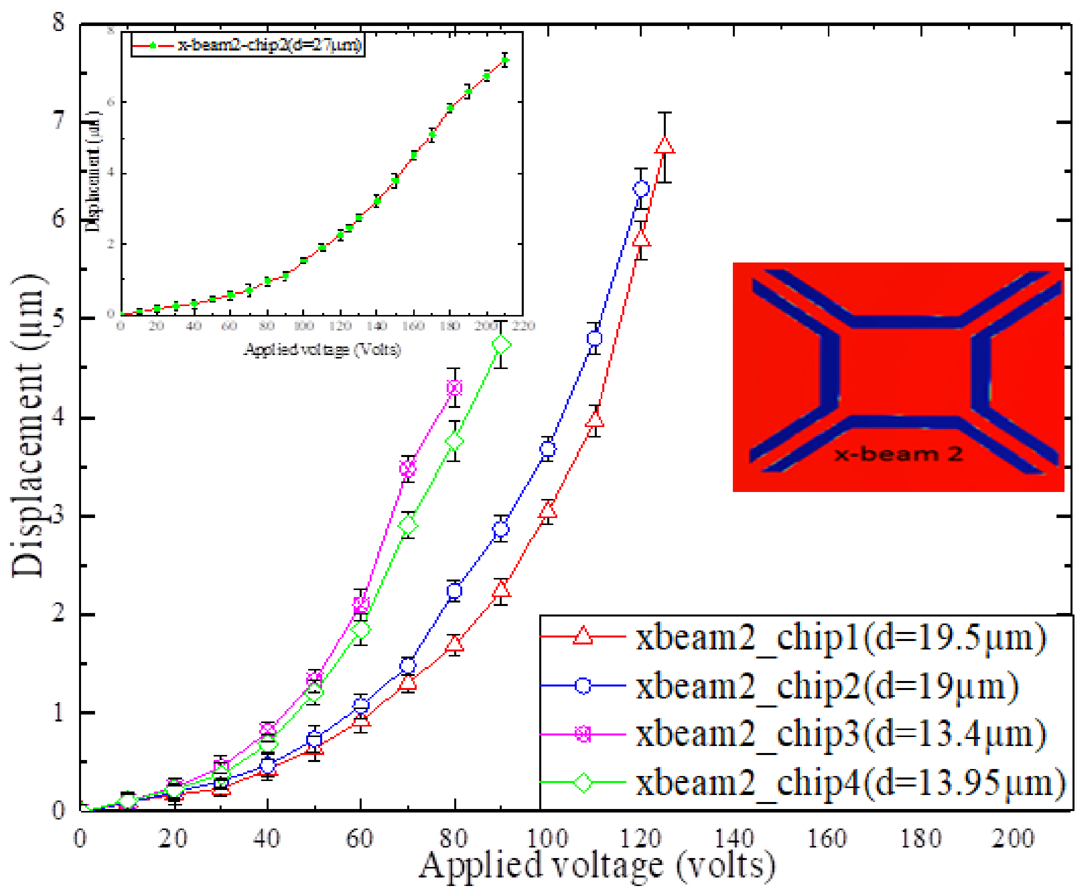

x-beam2-chip2(d=27µm)
Applied voltage (Volts)
x-beam 2
xbeam2_chip1(d=19.5µm)
xbeam2_chip2(d=19µm)
xbeam2_chip3(d=13.4µm)
xbeam2_chip4(d=13.95µm)
Displacement (µm)
Applied voltage (volts)

(b)

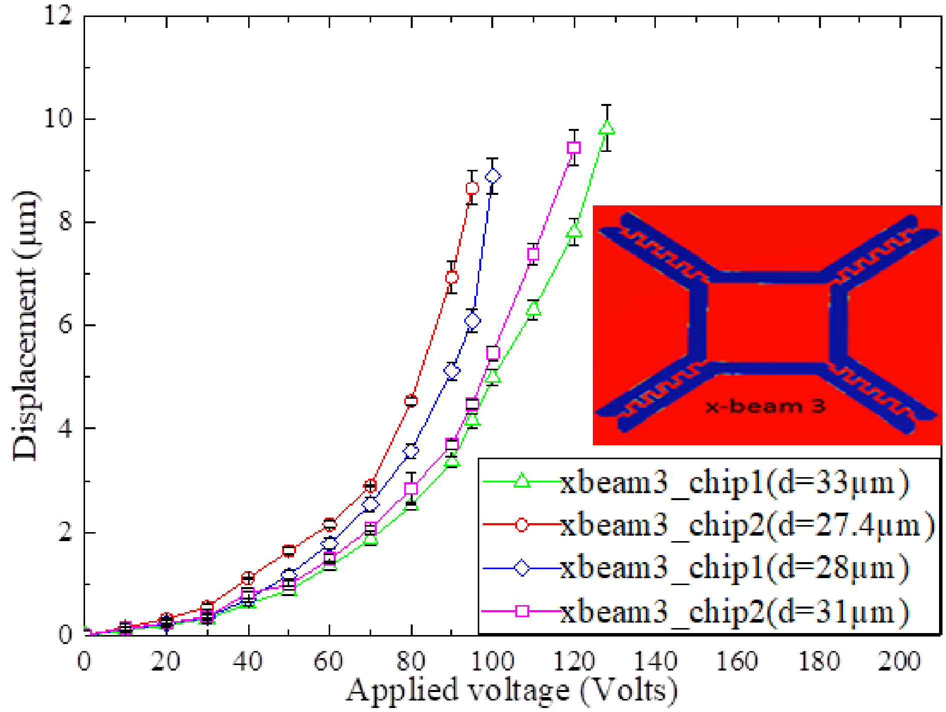

(c)

Figure 27. Displacement of x-beams for two spacer thicknesses on two different membrane chips for (a) x-beam 1, (b) x-beam 2, and (c) x-beam 3. Though x-beams 1 and 3 have almost the same surface area, x-beam 3 snaps at a lower voltage than x-beam 1, meaning its design results in a lower mechanical stiffness constant. The inset of (b) shows the displacement of x-beam 2 at 210 VDC (the limit of our power supply). Since it didn't reach its snap-in condition, it means its stiffness constant must be very large. Smaller spacer thicknesses were then used to determine its stiffness constant.

According to the model governing the behavior of parallel plate actuators, the mechanical stiffness constant of micro-actuators depends on surface area and length of arms [93, 95]. Even though x-beams 1 and 2 have the same arm lengths, x-beam 1 has a higher displacement than x-beam 2 for a similar spacer thickness, as shown in Fig. 27a and the inset of Fig. 27b. This arises from the difference in the surface areas of the two x-beams. However, as shown in Fig. 27a and Fig. 27c, x-beam 1 has a lower displacement than x-beam 3 at any applied voltage for similar spacer thicknesses despite both having almost the

same surface area. The first reason for this is that x-beam 3's arms are longer than those of x-beam 1's. Another reason is due to the different arm designs. While x-beams 1 and 2 have rigid arms that uniformly distribute an accumulation of electric charge across their surfaces, x-beam 3 has a design that causes accumulation of charge on the sharp corners of the meanders; hence the electrostatic force will be larger at those corners. The result is a larger electrostatic force pushing down on x-beam 3, causing its displacement to be much larger than its two counterparts [94, 95]. In addition, x-beam 3 incorporates ten folded meanders that are arranged in series, hence the effective stiffness constant of this x-beam is given by, $\frac{1}{k_{eff}} = \sum_{i=1}^{i=10}(\frac{1}{k_i})$ and the serpentine design allows the x-beam to achieve a lower stiffness constant.

Table IV: Estimated mechanical stiffness constants and sensitivities of x-beams 1, 2, and 3.

x-beam	Spacer thickness (μm)	Snap-in voltage (VDC)	Sensitivity (μm/V)	Stiffness constant (N/m)
x-beam1 chip #1	32	202	0.05	177
	26	146	0.058	172.43
x-beam1 chip #2	30.5	185	0.049	171.5
	25	136	0.062	168.29
x-beam2 chip #1	13.95	76	0.06	374.79
	19.5	125	0.053	371.35
x-beam2 chip#2	13.42	72	0.059	377.98
	19	121	0.052	376.2
x-beam2 chip #2	27	Did not snap at 210	0.034	-
x-beam3 chip#1	33	128	0.08	64.68
	28	101	0.088	65.92
x-beam 3 chip #2	31	118	0.08	66.31
	27.4	95	0.089	62.24

The estimated mechanical stiffness constants and sensitivities are shown in Table IV. The estimation and knowledge of the mechanical stiffness constant is important since it has an impact on the electromechanical characteristics of MOEMS micro-actuators. In this work, we confirmed that the thickness of the spacer that separates the movable membrane and stationary bulk chips alters the electrostatic force, which in turn affects the displacement of the movable membrane; we use this information to estimate the sensitivity and mechanical stiffness.

To estimate the mechanical stiffness constant of x-beams, the snap-in voltages were used as per Eq. (4.4). For two different x-beam chips at two different spacer thicknesses, the estimated values of mechanical stiffness constants are within 5% of one another.

The sensitivity, an electromechanical parameter is calculated by dividing the displacement with respect to an applied external bias (d/v) of the micro-actuators, serves to highlight and study the mechanical performance of various x-beam designs even further [96, 97]. As shown in Table IV, the sensitivities of each x-beam design were calculated from the electromechanical test using the maximum stable displacement attained at the snap-in point. The sensitivities of x-beam 3 for all spacer thicknesses were found to be much larger than those of x-beams 1 and 2. It is noted that when a lower stiffness constant with a reasonable sensitivity is required, it is very useful to use serpentine x-beam design. The estimated results showed that x-beam-3 attains an average sensitivity of ~ 0.084 μm/V. The higher sensitivity of x-beam 3 allows the micro-actuator to operate at lower applied voltage, that later reduces the power consumption and makes it compatible with the CMOS technology.

The on-set of instability for x-beams at the snap-in voltages mentioned earlier is shown in Figure. 28 below. There is an abrupt change in the displacement of the micro-actuators past the snap-in condition.

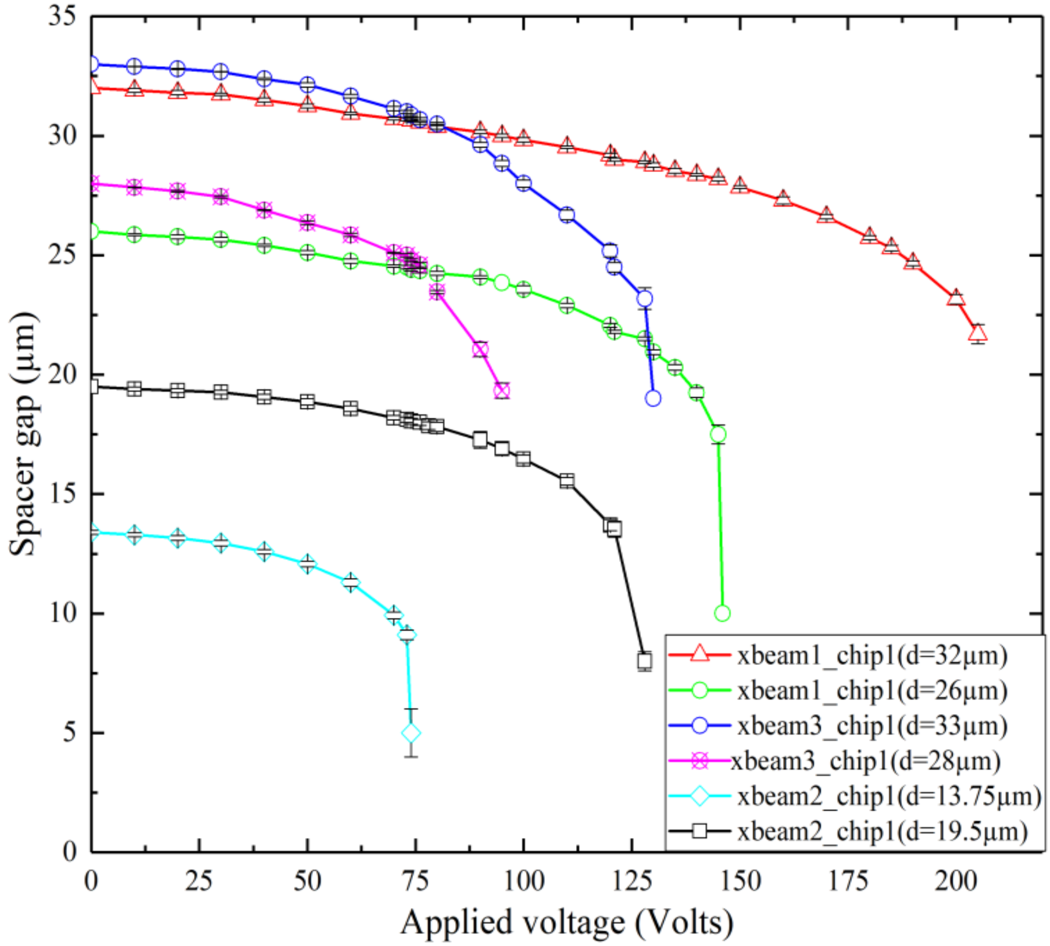

Fig. 28. Spacer gap vs. applied voltage. For each x-beam design, the snap-in condition is shown to be the point where the spacer gap between movable membrane and stationary bulk chip has exceeded one-third of its initial value. There is an abrupt change in the spacer gap past this point.

The cross-sectional area per arm length is another important factor that should be considered while designing movable x-beam membranes. This parameter affects the stiffness constants of the micro-actuators, that later has an effect in the electromechanical performance of assembled devices.

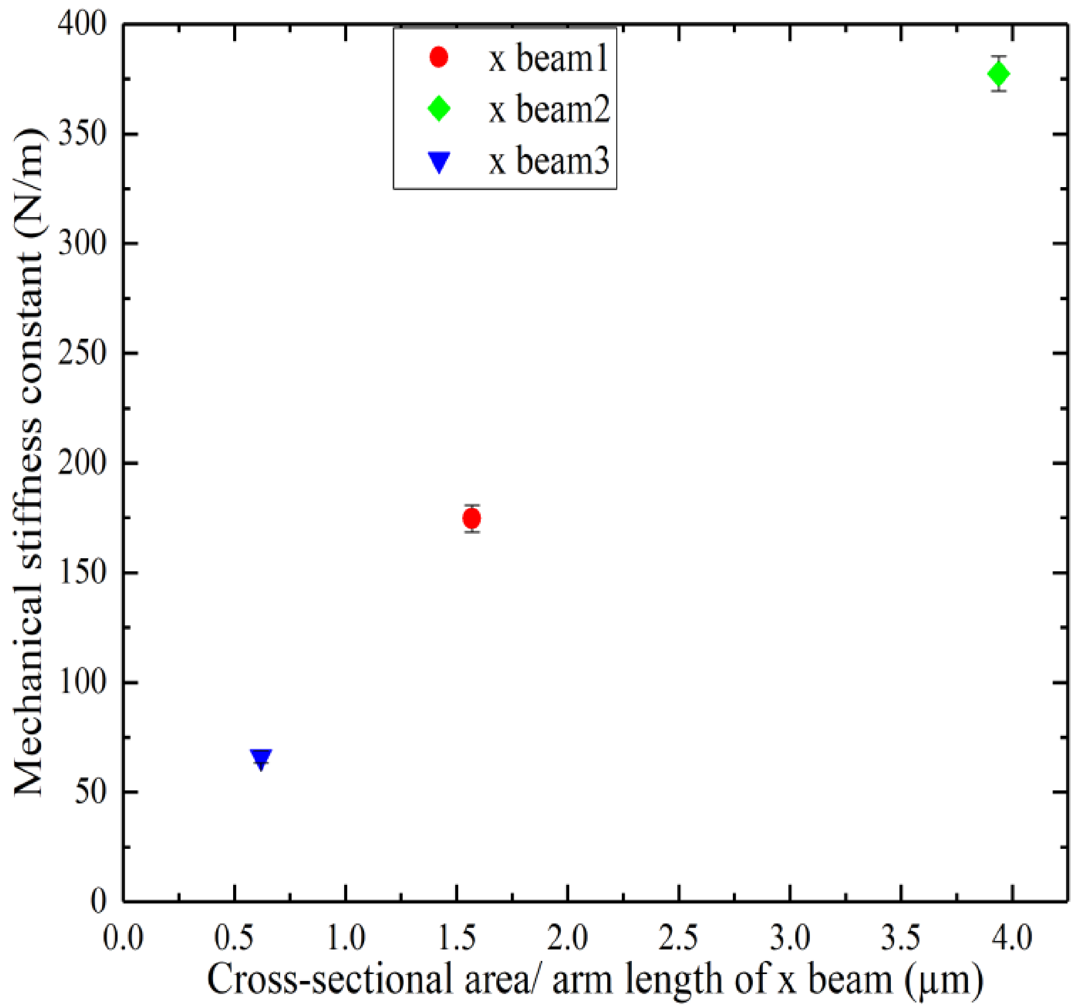

Figure. 29. Mechanical stiffness constant vs. x-beam area of cross-section per arm length. As can be seen x-beam area of cross-section/arm length is proportional to mechanical stiffness constant of the x-beam design. The meandering design of x-beam 3, which has a smaller cross-sectional area per arm length, plays a role in optimizing the displacement of the micro-actuator at a given applied voltage that minimizes its mechanical stiffness constant. All the cross-sectional area per arm length comparisons are based on a micro-actuator with active device layer of $\approx 30\ \mu m$.

The MOEMS-based micro-actuators with DBR mirrors were developed and assembled. The displacements of the micro-actuators with DBR layers was very low compared to the micro-actuators without DBR layers as shown in Figure. 30 below.

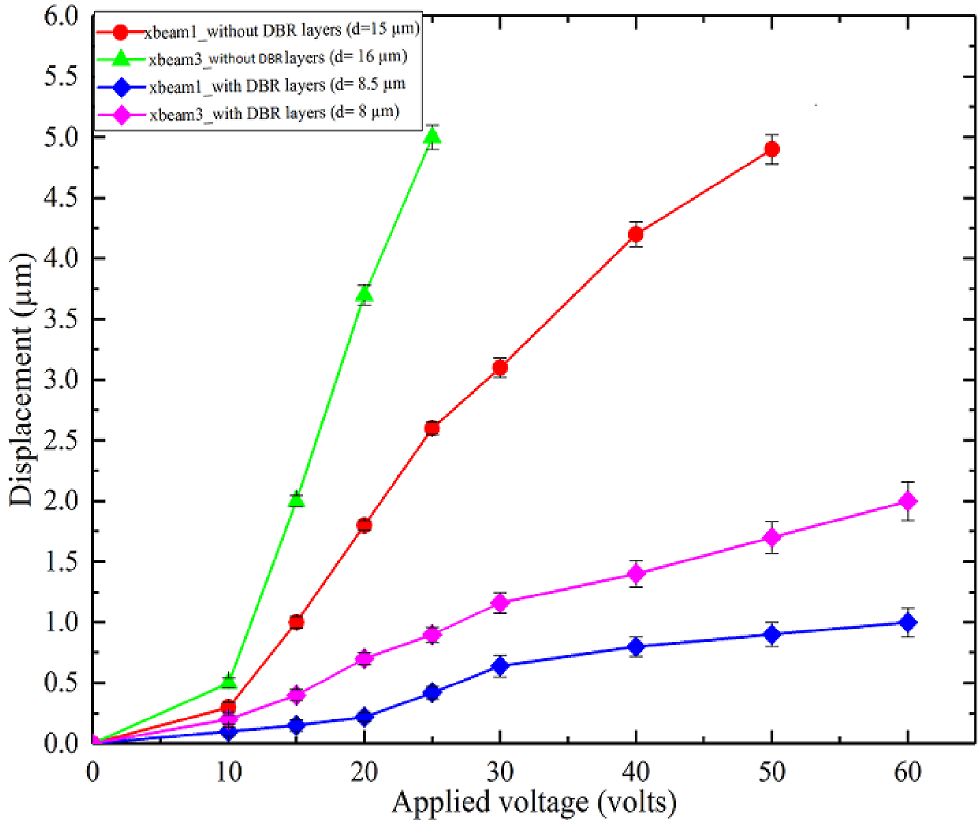

Figure 30. Displacement of x-beams for two spacer thicknesses on two different membrane chips with DBR thin films.

However, because of the defects in the movable DBR, such as bowing, non-planarity and non-parallelism, the assembled MOEMS micro-actuators with DBR mirrors showed limited tunability. The non-parallelism usually occurs when there is a variation in the thickness of the SU-8 photoresist spacer layer that might arise from non-uniform bonding pressure between the movable and stationary DBR mirrors.

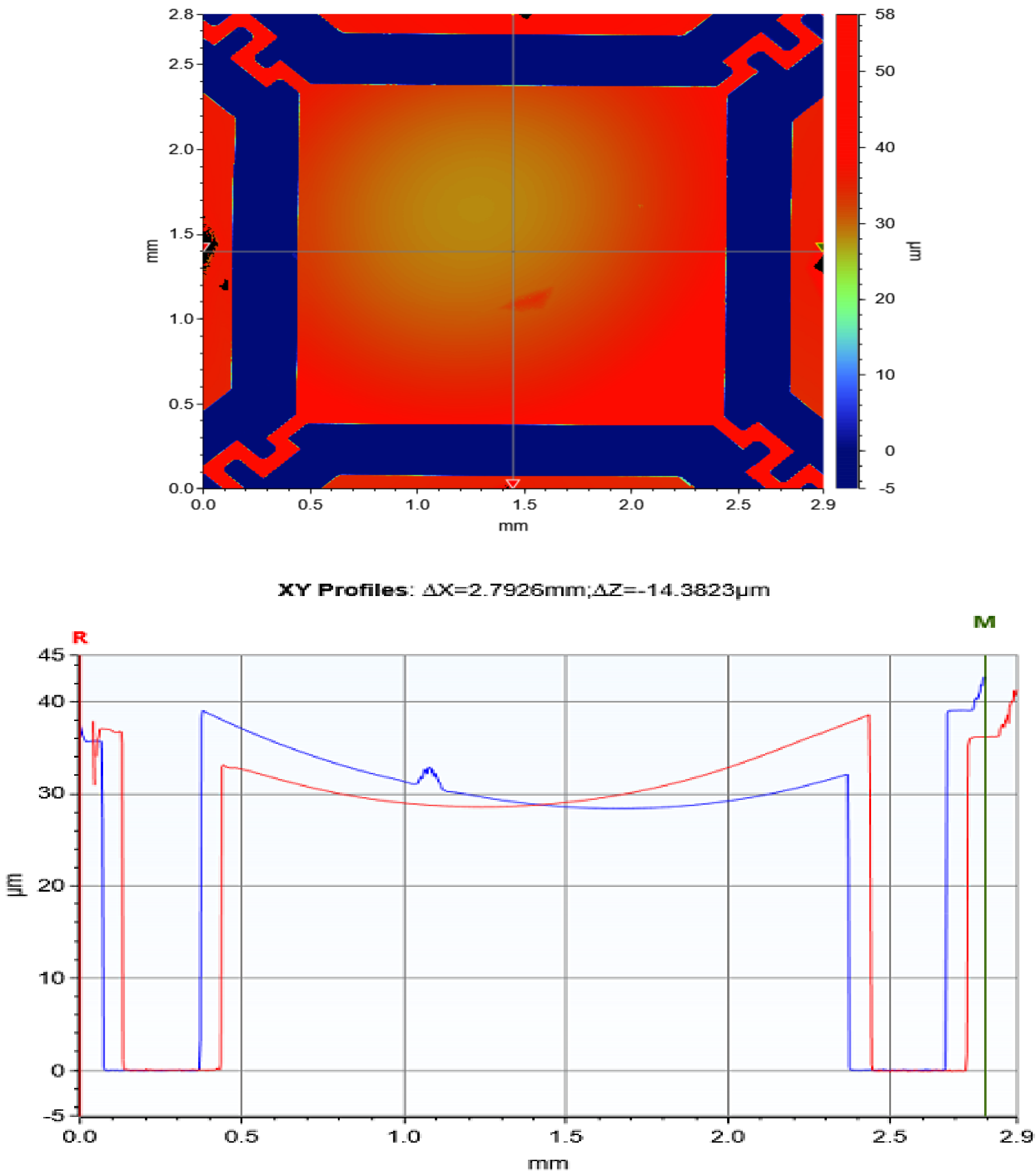

Figure 31. X-Y profile scans of the displacement of micro-actuator with DBR layers, at 5 VDC.

The non-parallelism effect of the DBR mirrors get worse during the actuation. This is an inherent limitation of parallel-plate micro-actuators. The micro-actuation data was not repeatable, and it makes the integration of these devices impractical. The curvature of the movable DBR mirror gets worse when multilayers were deposited on the thin movable membrane. The bowing effect is one of the major drawbacks of these devices that limits them from hyperspectral sensing application.

6.3. Least square curve fitting

The electromechanical test data acquired at different applied voltages for the various x-beams were fitted to extract the mechanical stiffness constants. The mechanical stiffness constants of the x-beam designs for various spacer thicknesses are shown below.

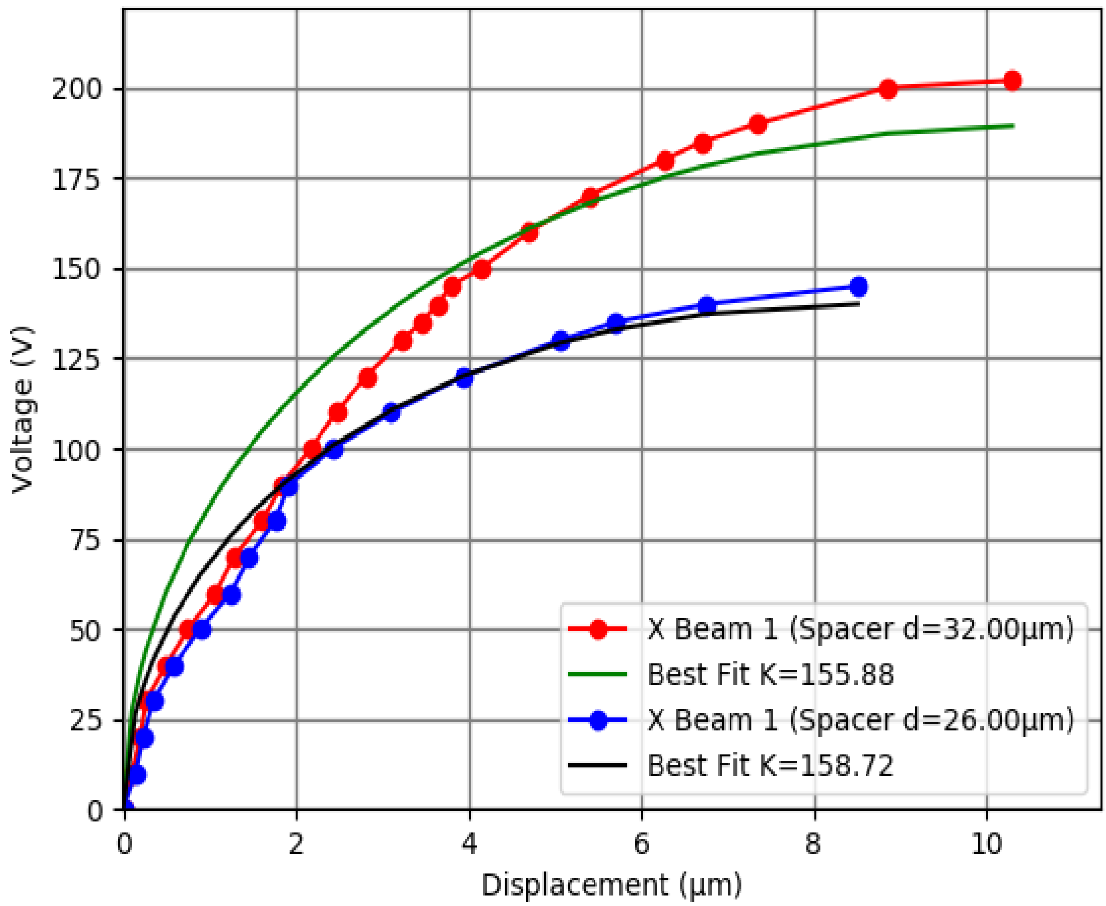

(a)

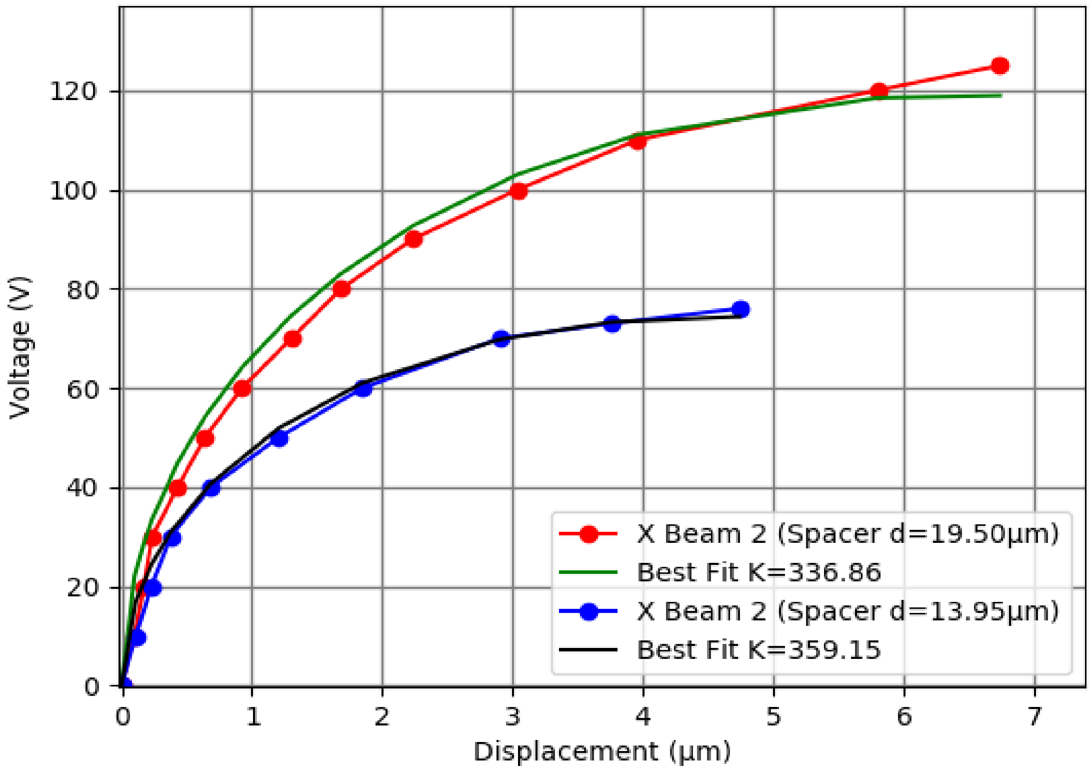

(b)

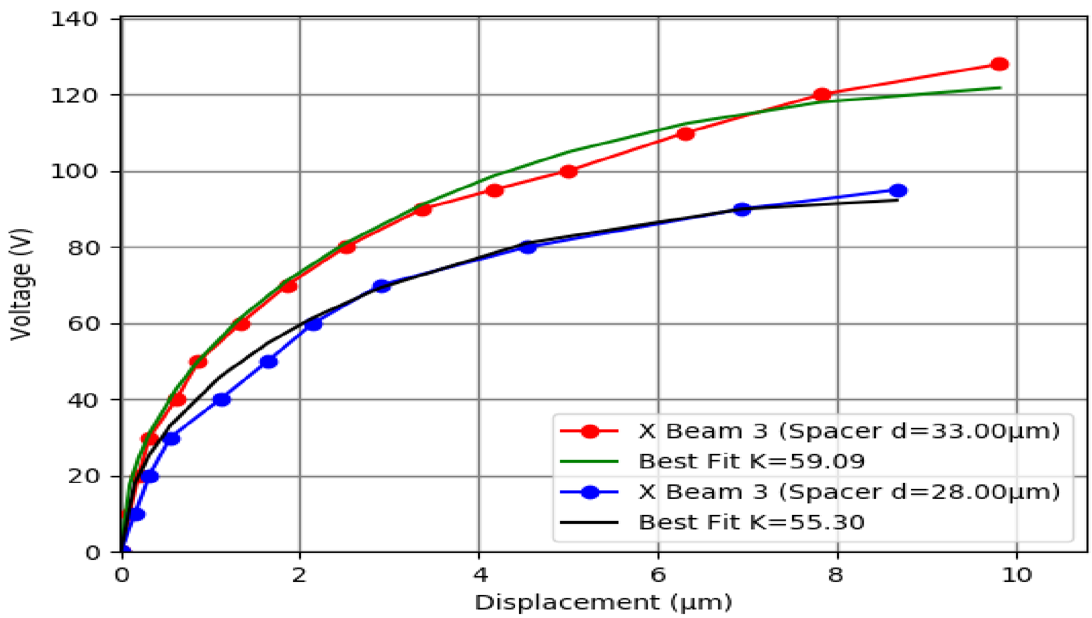

(c)

Figure 32. Least square fits of the mechanical stiffness constants.

The mechanical stiffness constants were least square fitted as shown in Fig. 32. The best fit line agrees with in ~ 10% of the experimental data, as illustrated in the Table V.

x-beam	Spacer thickness (μm)	Snap-in voltage (VDC)	Stiffness constant experimental (N/m)	Stiffness constant least square fit (N/m)
x-beam 1	32	202	177	155.58
	26	146	172.43	158.72
x-beam 2	19.5	125	371.35	336.82
	13.95	76	374.79	359.15
x-beam 3	33	128	62.5	59.09
	28	101	63	55.3

Table V: Comparison between the mechanical stiffness constants of the x-beams: least square fitted and experimental data.

7. Optical analysis of DBRs and Fabry-Perot optical filters

In this chapter, we will analyze the optical performance of DBR mirrors and Fabry-Perot optical filters. The selection and growth of various DBR thin film materials is presented. Particularly E-beam deposition of the selected DBR thin films is discussed. An optical model, that uses the optical transfer matrix method is employed to guide the experiment. The optical characterization of DBR mirrors and optical filters with an emphasis on the optical transmission and spectral resolution will be discussed. Interfacial grading of the multi-layer structure that has the potential to optimize the optical performance of DBR mirrors and Fabry-Perot optical filters is suggested. We have also demonstrated the fabrication of a DBR mirror that exhibits a highly reflective and wide stop-band zone. The mirror is designed to operate in the MWIR region, with a central wavelength of 4 μm.

7.1. Material selection for DBR mirrors in the MWIR region

Various dielectric materials have been explored and assessed for the application of DBR optical mirrors. Selecting the suitable dielectric material for the DBR structure is very critical, and it depends on many conditions that include, adhesion between the multilayers, environmental safety, compatibility of the deposition process, spectral range and the required reflection [98]. Highly reflective DBR structures with high refractive index contrast and lossless materials should be designed for the target infrared spectrum [99].

The optical performance of the dielectric materials plays a vital role in choosing the proper materials for the optical mirrors. The extinction coefficient and the percentage of absorption loss are the main parameters that give the required information to predict and select the ideal dielectric materials suitable for DBR mirrors [99]. The absorption of the dielectric materials limits the performance of the DBR mirrors. Since a variety of dielectric materials absorb in MWIR region, it should be noted that they must be chosen in a way to provide a very low percentage of absorption

[98, 99]. Fig. 33 below shows the absorption and extinction coefficients of ~ 1 μm thick single layer of ZnSe, BaF_2, Ge and ZnS dielectric thin films, which are commonly used for DBR applications.

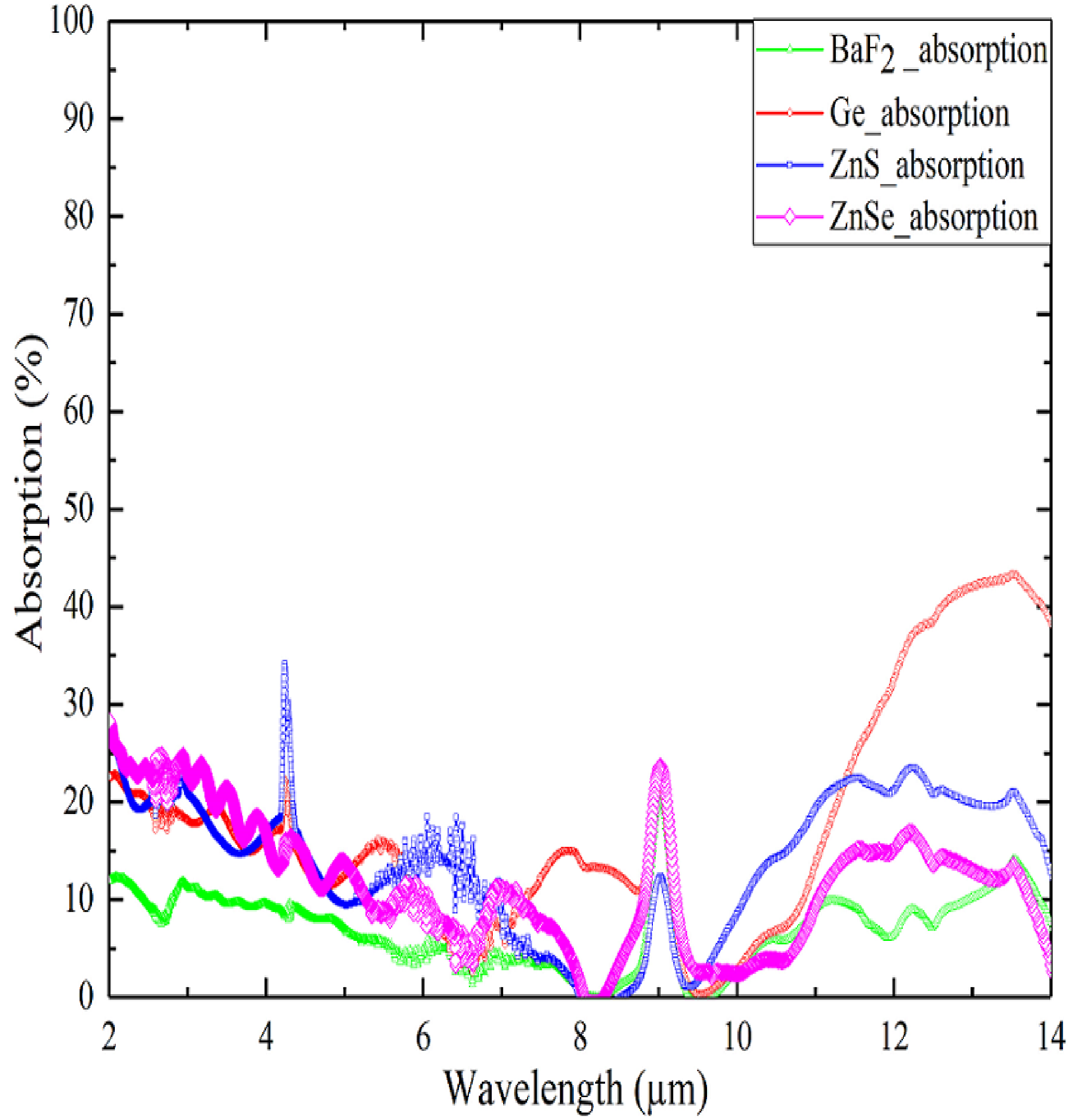

(a)

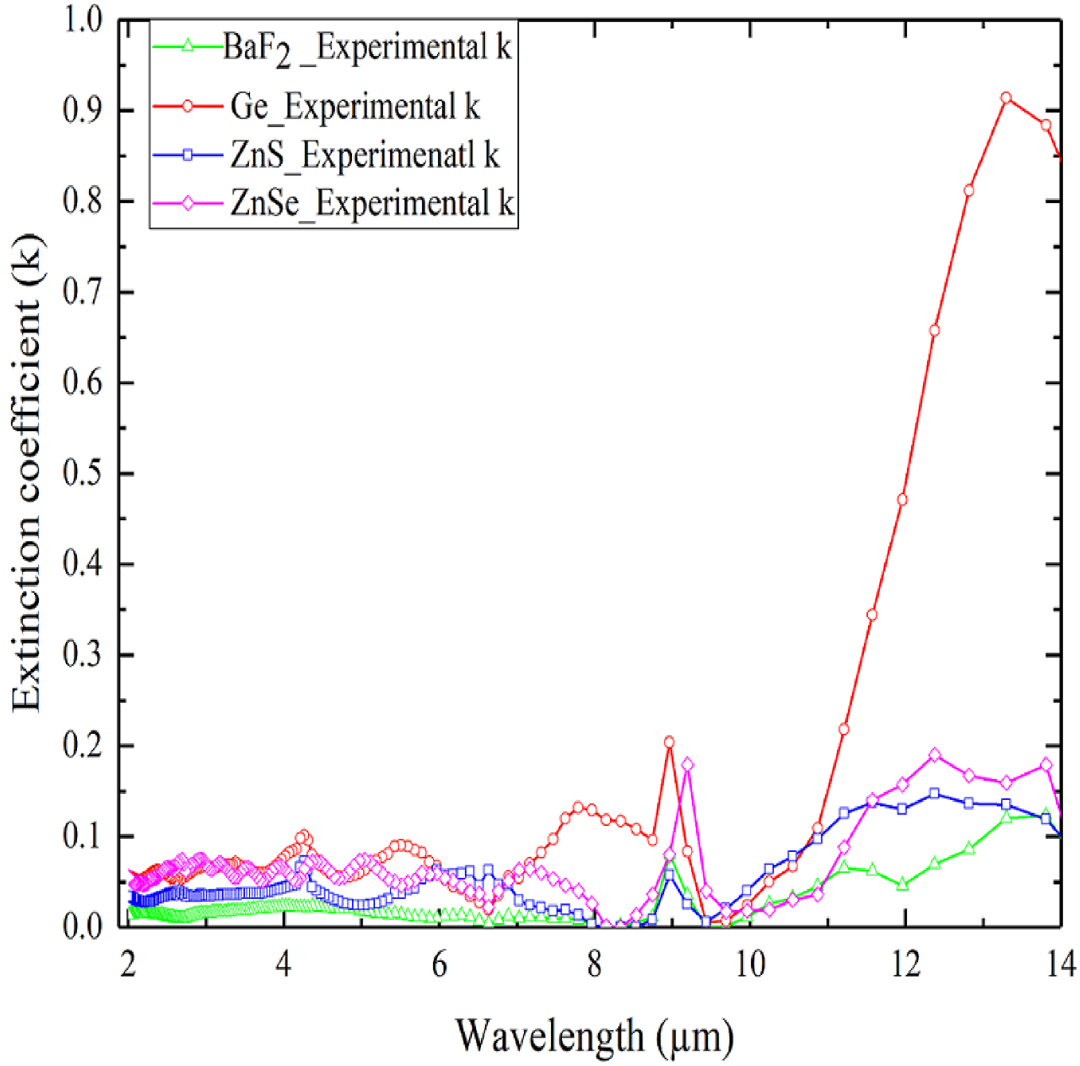

(b)

Figure 33. a) Absorption vs. wavelength and b) extinction coefficient vs. wavelength of various dielectric materials.

To understand the optical performance the deposited DBR thin films in the MWIR region, the absorption losses and the extinction coefficients were studied. Although other techniques, including ellipsometry, are available to predict these values, in this work we have chosen the optical transfer matrix model. Mathematical derivations will be discussed later in Section 7.2 of this thesis.

	Hall		Our data at Microphysics Laboratory, UIC	
Extinction coefficient of ZnSe	MWIR	LWIR	MWIR	LWIR
	$7x10^{-2}$	$1x10^{-3}$	$7.7x10^{-3}$	$2.3x10^{-2}$

(a)

	Utah State University		Our data at Microphysics Laboratory, UIC	
Extinction coefficient of BaF_2	MWIR	LWIR	MWIR	LWIR
	$1.5x10^{-3}$	$2x10^{-3}$	$1x10^{-3}$	$2x10^{-2}$

(b)

	Hall		Our data at Microphysics Laboratory, UIC	
Extinction coefficient of Ge	MWIR	LWIR	MWIR	LWIR
	$4x10^{-4}$	$2x10^{-5}$	$8x10^{-2}$	$2.4x10^{-2}$

(c)

	Hall		Our data at Microphysics Laboratory, UIC	
Extinction coefficient of ZnS	MWIR	LWIR	MWIR	LWIR
	$1.5x10^{-3}$	$2x10^{-3}$	$5.7x10^{-2}$	$9x10^{-2}$

(d)

Table VI: Comparison between the extinction coefficients (a) ZnSe, (b) BaF_2, (c) Ge, and (d) ZnS thin films [100, 113].

The extinction coefficients of the fabricated single layer ZnSe, BaF_2, Ge and ZnS thin films were compared with current results of other researchers in Table VI. Our experimental data of BaF_2 and ZnSe thin films agrees well in the MWIR region, with minor differences compared to the literature data. We believe the polycrystalline nature of the deposited thin films in our laboratory have higher absorption and higher extinction coefficients when compared with the single crystalline literature data. It is well studied that polycrystalline thin films usually have pronounced defects that increase the absorption loss. We believe the grain boundaries of polycrystalline thin films are the major defects that makes the absorption loss higher compared to the single crystalline counterparts. As can be seen from Fig. 32, ZnSe and BaF_2 thin films have low absorption losses and low extinction coefficients in the infrared region, hence they were chosen as appropriate source materials for the fabrication of DBRs.

The various material properties of DBR thin films at room temperature are summarized in the table below.

	Ge	ZnS	ZnSe	BaF_2
Refractive index at 4 µm	4.02	2.25	2.43	1.45
Refractive index at 10 µm	4.00	2.20	2.40	1.40
Band gap (eV)	0.67	3.54	2.58	9.1
Electronic absorption edge at 300K (µm)	1.85	0.33	0.476	0.136
Lattice absorption edge (µm)	18	10	22.2	22
Absorption mechanism of incident photon	Multiple phonon absorption	Multiple phonon absorption	Multiple phonon absorption	Single phonon absorption
Thermo-optic coefficient (dn/dT) at 300K (K^{-1})	$4.25x10^{-4}$	$4.2x10^{-5}$	$6.26x10^{-5}$	$-1.64x10^{-5}$
Thermo-optic coefficient (dn/dT) at 120K (K^{-1})	$3.3x10^{-4}$	$4.1x10^{-5}$	$5.29x10^{-5}$	$-9.95x10^{-6}$

Table VII: Material properties of DBR thin films at room temperature [114].

It is also important to check other optical properties of DBR thin films, such as optical transparency, thermo-optic properties, and the absorption mechanisms of the DBR thin films in the target MWIR region. As was discussed in Section 5.4, the optically transparent region lies between the electronic and lattice absorption edges. The selected DBR thin films are optically transparent in the MWIR region as illustrated in Table VII. Where, ZnSe is optically transparent between 0.476 µm and 22.2 µm, and BaF_2 is optically transparent between 0.136 µm and 22 µm. The dielectric thin films used in this work also offer the advantage of no spectral wavelength shift while operating at lower temperatures, since it is composed of materials with positive and negative thermo-optic coefficients that compensate this effect.

7.2. Optical modeling of DBR thin films

In this section the propagation of electromagnetic radiation through the multilayer structure is modeled and assessed using the governing thin film equations. The multilayer structure was regarded as an optical system with an entrance and exit ports [35, 100, 119]. The incident waves at the entrance port are always related with the reflected and transmitted waves at the exit port [119, 122]. The transfer matrix is built by considering the multi-layer structure as a cascaded system of interfaces and layers, where each layer has its own transfer matrix. The complete optical transfer matrix is obtained by multiplying the transfer matrices of each layer in the DBR structure [35, 100].

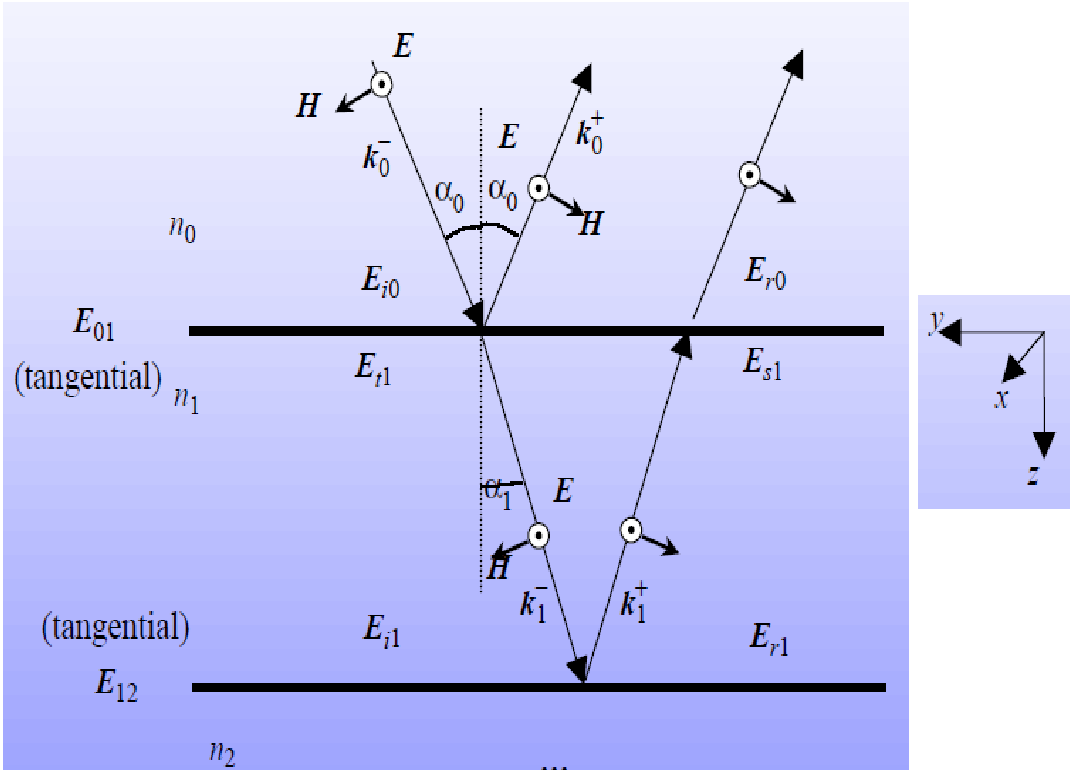

Figure 34. Schematic of multilayered optical materials [29]

In this section we will derive the optical transfer matrix by applying the boundary conditions and relationships discussed in Section 2.3 of this thesis. In the optical transfer matrix formalism, an s-polarized wave is assumed, and the tangential components of the electromagnetic fields are considered. Mathematical derivation of the optical transfer matrix are given by a set of equations [35, 100]:

$$\begin{cases} \boldsymbol{E}_{01} = \boldsymbol{E}_{t1} + \boldsymbol{E}_{s1} \\ \eta_0 \boldsymbol{H}_{01} = \gamma(\boldsymbol{E}_{t1} - \boldsymbol{E}_{s1}) \\ \boldsymbol{E}_{12} = \boldsymbol{E}_{i1} + \boldsymbol{E}_{r1} \\ \eta_0 \boldsymbol{H}_{12} = \gamma(\boldsymbol{E}_{i1} - \boldsymbol{E}_{r1}) \\ \gamma = n_1 \cos(\alpha_1) \end{cases} \tag{7.1}$$

where η_o and γ represent the optical admittances of free space and dielectric layers, respectively.

For the DBR multilayered structure, the tangential component of the electric fields are related to each other by taking into consideration the optical path change of each layer and it is given by [35]:

$$\begin{cases} \boldsymbol{E}_{i1} = \boldsymbol{E}_{t1}\boldsymbol{e}^{-i\delta} \\ \boldsymbol{E}_{s1} = \boldsymbol{E}_{r1}e^{-i\delta} \\ \delta = d_1\boldsymbol{k_{z1}} = \frac{2\pi}{\lambda}n_1 d_1 \cos(\alpha_1) \end{cases} \tag{7.2}$$

where δ denotes the optical phase shift.

Solving for the tangential part of the electromagnetic radiation on both ends of each layer yields a characteristic optical transfer matrix,

$$\begin{pmatrix} \boldsymbol{E}_{01} \\ \eta_0\boldsymbol{H}_{01} \end{pmatrix} = \begin{pmatrix} \cos\delta & \frac{i\sin\delta}{\gamma} \\ i\gamma\sin\delta & \cos\delta \end{pmatrix} \begin{pmatrix} \boldsymbol{E}_{12} \\ \eta_0\boldsymbol{H}_{12} \end{pmatrix} \tag{7.3}$$

The transfer matrix connects the tangential fields of each layer, for instance, the j-th layer matrix is represented by:

$$M = \begin{pmatrix} m_{11} & m_{12} \\ m_{21} & m_{22} \end{pmatrix} = \begin{pmatrix} \cos\delta_j & \frac{i\sin\delta_j}{\gamma} \\ i\gamma\sin\delta_j & \cos\delta_j \end{pmatrix} \tag{7.4}$$

The optical transfer matrix for the whole multilayer structure is given by,

$$\begin{pmatrix} \boldsymbol{E}_{01} \\ \eta_0\boldsymbol{H}_{01} \end{pmatrix} = M_1 M_2 \ldots\ldots\ldots M_N \begin{pmatrix} \boldsymbol{E}_{N,N+1} \\ \eta_0\boldsymbol{H}_{N,N+1} \end{pmatrix} = M_{total} \begin{pmatrix} \boldsymbol{E}_{N,N+1} \\ \eta_0\boldsymbol{H}_{N,N+1} \end{pmatrix} \tag{7.5}$$

In this work, we used QWOT layers, hence the phase shift associated to each layer is, $\delta = \frac{2\pi}{\lambda} n_1 d_1 \cos(\alpha_1) = \frac{2\pi}{\lambda} n_1 \left(\frac{\lambda}{4n_1}\right) = \frac{\pi}{2}$. Substituting this value into Eq. (7.4), the transfer matrix will be modified as [35, 100]:

$$M = \begin{pmatrix} 0 & \frac{i}{\gamma} \\ i\gamma & 0 \end{pmatrix} \tag{7.6}$$

For a DBR mirror comprised of two alternating dielectric layers, the matrix will have a formalism:

$$M = \begin{pmatrix} 0 & \frac{i}{\gamma_1} \\ i\gamma_1 & 0 \end{pmatrix} \begin{pmatrix} 0 & \frac{i}{\gamma_2} \\ i\gamma_2 & 0 \end{pmatrix} = \begin{pmatrix} \frac{-\gamma_2}{\gamma_1} & 0 \\ 0 & \frac{-\gamma_1}{\gamma_2} \end{pmatrix} \tag{7.7}$$

The matrix in Eq. (7.7) for a single bilayer of DBR mirror with configuration of [HLHL..H] materials is re-written by:

$$M = \begin{pmatrix} \frac{-n_L}{n_H} & 0 \\ 0 & \frac{-n_H}{n_L} \end{pmatrix} \tag{7.8}$$

For N bilayers or number of stacks, the optical transfer matrix will consist of N identical matrices,

$$M = \begin{pmatrix} (\frac{-n_L}{n_H})^N & 0 \\ 0 & (\frac{-n_H}{n_L})^N \end{pmatrix} \tag{7.9}$$

The reflectivity of the DBR multilayer structure are often calculated by inserting Eq. (7.9) into Eq. (7.5) and taking into consideration the number of stacks in the whole DBR structure [100].

In this work, the optical transmission of the whole DBR structure is computed by solving the values of B and C:

$$\binom{B}{C} = M_1 M_2 \ldots \ldots . . M_N \binom{\mathbf{1}}{\eta_0 n_s} \tag{7.10}$$

The optical transmittance of the multilayer structure is given by:

$$T = \frac{4{\eta_0}^2 \eta_s}{(\eta_0 B + C)\,(\eta_0 B + C)^*} \tag{7.11}$$

Eq. (7.11) is useful to calculate the optical transmission of DBRs and it also helps to extract unknown parameters [29, 100].

In this work, the optical performance of different stacks of ZnSe and BaF_2 dielectric thin films were modeled. The computed transfer matrix has been utilized to predict transmission, reflection of DBRs [120, 121]. The purpose of optical modeling in this thesis work is to guide the experimental design of the DBR mirrors.

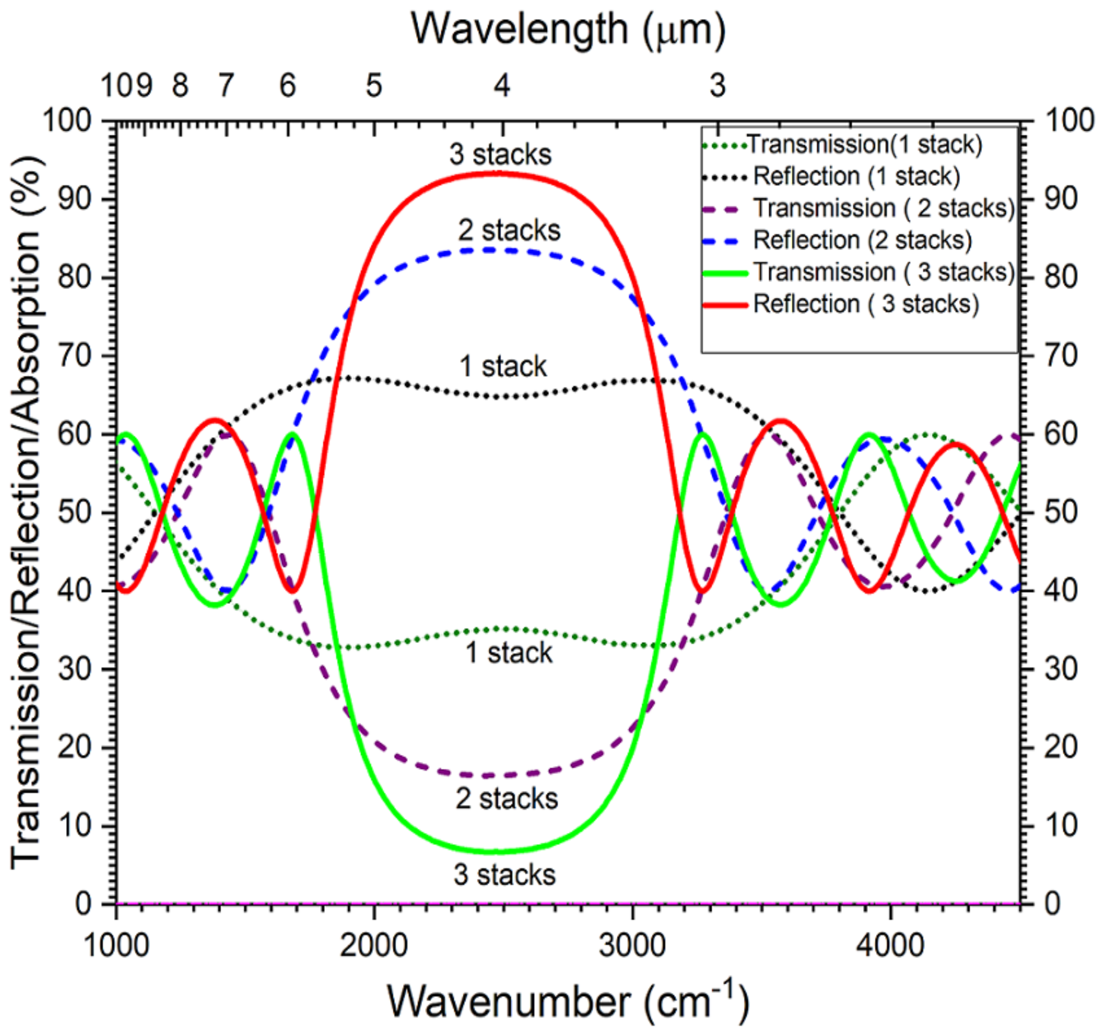

Figure 35. Modeled optical properties of DBR thin films for various dielectric stack numbers.

The optical modeling predicts that the reflection of the DBR mirror increases as the number of dielectric stacks increases, and that three stacks of $ZnSe/BaF_2$ thin films can achieve ~ 93% reflection. Ideal conditions were used in the optical model, such as assuming the dielectric layers are completely lossless, the thicknesses of the alternating thin films are uniform, and each layer has a thickness specified by QWOT, the surface roughness between each interface is also ignored and the infrared signal has been assumed to have normal incidence.

7.3. Electron-beam deposition of DBR thin films

7.3.1 Experimental set-up

Electron beam evaporation was used to grow the DBR thin films. The electron beam deposition technique has been chosen since it has several advantages compared to the other PVD techniques, namely thermal evaporation and sputtering methods. Electron beam deposition offers a high material utilization efficiency that reduces the cost compared to other PVD methods. It has a lower degree of contamination from the crucible or boat since the electron beam only heats the target material, which affects the quality of the thin film [16]. Electron beam evaporation also has the flexibility to attain a wide range of deposition rates [12, 15].

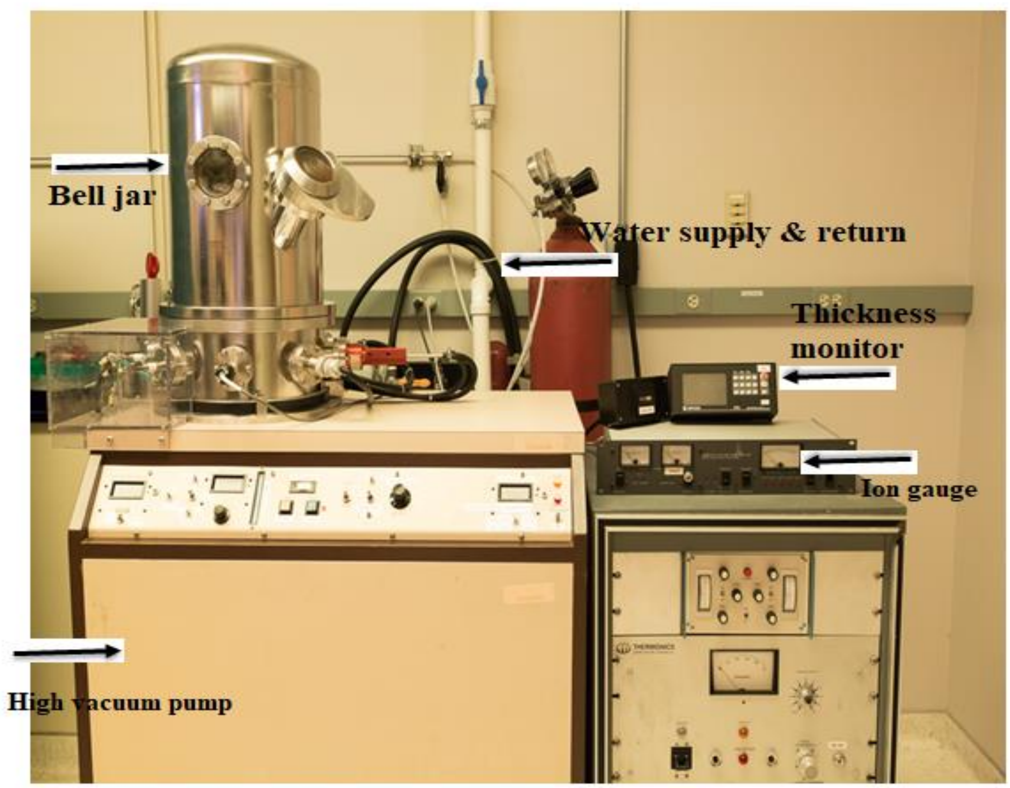

(a)

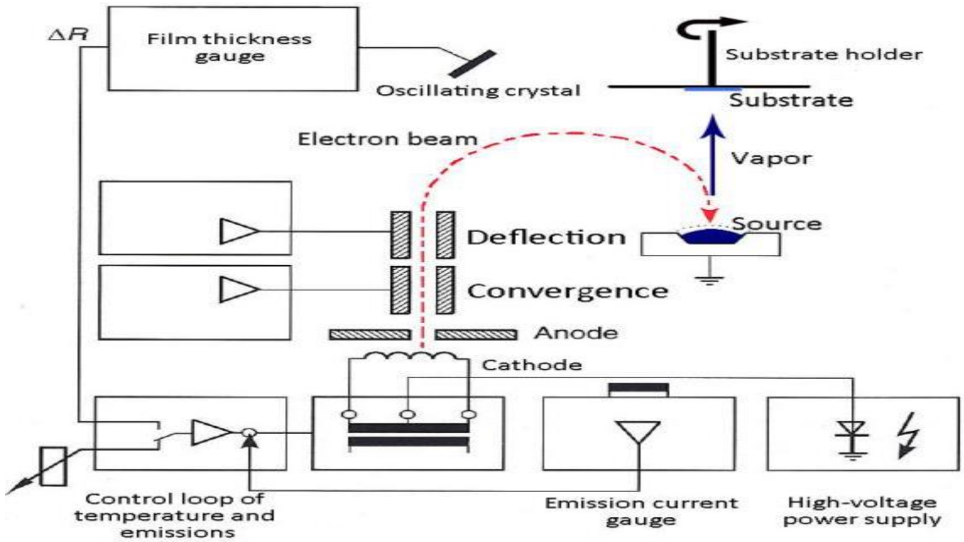

(b)

Figure 36. (a) Thermionics VE-100 E-beam vacuum evaporator, (b) schematic diagram of electron beam deposition process [12].

In this work, the dielectric thin film coatings were deposited on lightly doped silicon wafers using a Thermionics VE-100 E-beam vacuum evaporator system. The system is an auto-operating turbo-molecular pumped vacuum system with a metal bell jar mounted on a collar with feedthroughs for an electron beam gun evaporation source. It features an electron beam gun with three pockets in a graphite boat. The system allows a platform to deposit three different alternating source materials in a single run, hence it can deposit multi-layers in a single run without breaking the vacuum of the chamber.

7.3.2. DBR multilayers growth

The dielectric multilayers were deposited on lightly doped silicon wafers using the electron beam deposition technique. The wafers were RCA cleaned prior to thin film deposition. A base solution of NH_4OH: H_2O_2: H_2O with 1:1:5 was used to remove surface particles. The wafers were then dipped in hydrofluoric acid to remove the thin surface oxide resulting from the oxidizing conditions. Finally, the wafers were cleaned with an acid solution of HCl: H_2O_2: H_2O to remove trace contaminants [115]. The wafers were then dried with nitrogen, this cleaning step promotes the adhesion between the substrates and the thin films [115]. Alternating layers of the dielectric thin films were then sequentially deposited on the cleaned substrates to form the DBR structure.

The DBR multilayer structure in this work is comprised of alternating stacks of polycrystalline ZnSe and BaF_2 thin films grown on a silicon substrate to operate in the MWIR region. The DBR mirror made from three stacks of ZnSe/BaF_2 thin films achieved a reflection of ~ 93%, which makes it applicable to optical filtering. The dielectric thin films were grown at the NCF of UIC at deposition rates of ~ 2.5 Å/s for BaF_2, 3 Å/s for ZnSe, and 12 Å/s for SiO thin films. The vacuum chamber was held at a pressure of 6 x10^{-6} torr during the deposition.

Each dielectric multilayer growth was carried out on a 380 µm thick, lightly doped silicon wafer with <100> orientation at room temperature. The target thicknesses of the DBR thin films were ~ 416 nm and ~ 689 nm for ZnSe and BaF_2 layers, respectively, which corresponds to the QWOT. Interfacial grading layers of nano-thick amorphous silicon monoxide were also deposited using the electron beam evaporator system.

Source material	Density (g/cm^3)	Z-ratio	Pressure (torr)	Refractive index at 4µm	Deposition rate (Å/s)	Target thickness (nm)
ZnSe	5.26	0.722	$6x10^{-6}$	2.4	3	416
BaF_2	4.88	0.930	$6x10^{-6}$	1.45	2.5	689
SiO	2.16	0.870	$6x10^{-6}$	1.78	12	80

Table VIII. Growth conditions of DBR thin films

The resulting DBR mirrors are highly reflective and mechanically stable. The adhesion of the DBR multilayers was examined using a tape-test [98]. A kapton tape was used to check and characterize mechanical stability of DBRs. The DBRs did not either delaminate or crack from the substrate while pulling. This is believed to principally be a consequence of pre-cleaning of the substrate with the RCA solution prior to thin film deposition [98]. The topology of the DBR multi-layer structures was investigated using a high resolution transmision electron microscope (HR-TEM). Their TEM images are presented in the later sections of this thesis.

7.4. Interface grading of DBR mirrors

Interfacial grading of the dielectric Bragg mirrors is one of the most effective engineering techniques used to reduce thickness non-uniformity, surface roughness and defects at the interfaces between the alternating multilayers. Proper grading can be achieved by choosing a suitable material that matches with the optical properties and lattice structures of the alternating dielectric thin films [101].

In recent years, thin films of silicon monoxide have found use in many technological applications, such as protective layers in mirrors and electron microscopes. They have also been used in multi-layer coatings to increase the reflection of dielectrics in various spectral regions [102]. In this work, a nano-thick silicon monoxide thin film was chosen as an interface grading layer since it can easily adhere with ZnSe and BaF_2 polycrystalline thin films [103]. Silicon monoxide offers the advantage of reducing Fresnel optical loss since its refractive index value (n ~ 1.8 at 4 μm) is close to the geometric mean of the alternating dielectric Bragg reflector thin films, hence it acts as a nano-thick antireflection coating layer between the dielectric thin films. The nano-thick interface grading layer serves as a barrier to stop the inter-diffusion of atoms between the alternating dielectric multilayers, which can optimize the overall optical performance of the dielectric mirrors and Fabry-Perot optical filters.

In many cases, the condensed silicon monoxide thin films show a greater amount of oxygen composition compared to a true SiO thin film [104, 105]. It has been reported in the literature that true SiO thin films that have the proper stoichiometry were achieved by adjusting to ≥ 10 Å/sec deposition and deposition pressure, $p \leq 10^{-5}$ torr [105, 106]. It is noted that changes in the stoichiometry of interface grading thin film might also arise by gettering occurring while the thin film is condensing [106].

(i)

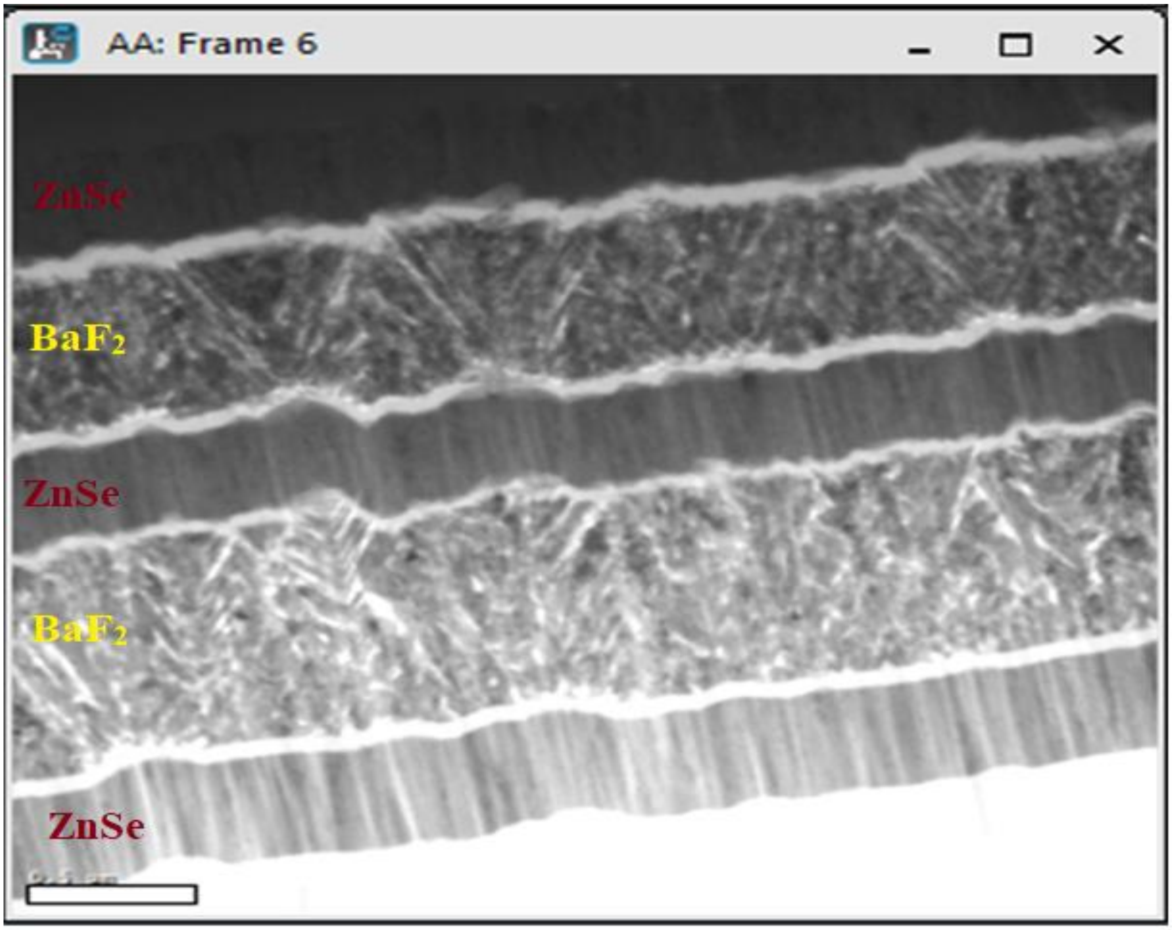

(ii)

Figure 37. Transmission electron microscope image of (i) abrupt interface (no SiO interfacial layers), (ii) graded interface (with SiO interfacial layers) DBR mirror composed of alternating ZnSe/BaF_2 thin films deposited using the electron beam deposition method for a target central wavelength of 4 µm.

XTEM has been used to characterize thicknesses and defects in the DBR multi-layer structure. The results (see Fig. 37(a)) showed there are thickness variations of DBR layers and roughness variations at different interfaces of the multilayer structure, these variations are expected to arise from the lattice mismatch between the consecutive layers [98]. The cross-sectional HR-TEM images also show the polycrystalline BaF_2 layers are more defective than ZnSe layers. The pores on the BaF_2 layers are indications of defects, hence there is a need to minimize the defects in the DBR multi-layer structure.

Fig. 37 (b) represents a high-resolution TEM image of graded interface DBR mirror. In this case, a nano-thick interface grading layer of SiO thin film, ~ 80 nm thick was deposited at each interface between the polycrystalline ZnSe and BaF_2 thin films. The nano thick amorphous SiO layer was deposited at a rate ~ 12 Å/s. when comparing the cross-sectional TEM images of Fig. 37(a) and Fig. 37(b), it is believed from the literature that both chemical reaction and interdiffusion of defective atoms reduce the optical performance of abrupt interface DBR mirrors [110]. The BaF_2 layers of abrupt interface DBR mirrors are porous, it is believed these pores are faceted islands. These faceted islands are highlighted in Fig. 37(a). The faceted porous islands in the BaF_2 layers are highlighted by circles in Fig. 37(a). The circles in BaF_2 layers were analyzed using an ImageJ, image processing software. The size of the highlighted red circles, namely faceted islands were estimated to vary in size from ~ 0.1 µm to ~ 0.28 µm in diameter. It is believed from the literature, the faceted islands in the BaF_2 layer are expected to be point defects. Particularly, Frenkel defect, one of the most common defects in ionic crystalline layers [107, 116]. The ImageJ analysis results also suggest that about 5.5%, 4%, and 3.5% of BaF_2 respective alternating layers have faceted island defects. It is also observed from the TEM images, the first BaF_2 layer has more pores compared to the other counterparts. It has been reported in the literature that these defects are mainly formed due to anisotropic interfacial energy of thin films [107, 116]. The graded interface DBR mirror does not have faceted islands, unlike the abrupt interface mirrors and it is believed the amorphous interfacial grading layers played a role in mitigating interdiffusion of defective atoms in the multilayer structure.

It is studied and well known in the literature that BaF_2 thin films often have a dendritic growth [107, 117]; by observing the TEM images we noticed the dendrites propagate to the adjacent ZnSe layers throughout the multi-layer structure in the case of abrupt interface DBR mirror. It is believed that the abrupt DBR mirror is suffering from diffusing defective atoms that degrade the optical performance of the mirror. In contrast, propagation of defects was not noticed in the graded interface DBR mirrors, it is interpreted that the SiO interface grading layer has stopped the propagation of defects.

We have also observed from TEM images that, the ZnSe layers of the abrupt interface DBR mirror closely follow the contours of BaF_2 layers immediately below, and it seemed to be in direct contact with BaF_2 layers. In contrast, the highly defective, highly irregular and partly porous BaF_2 layers show considerable pores in the adjacent ZnSe layers, this is evidenced by the line of the light contrast as highlighted by red squares in Fig. 37(a). The morphology is also apparent in the images. Though the graded DBR mirror showed similar layer morphology as abrupt interface DBR mirror, there are no obvious porous regions above each of the BaF_2 layers. Moreover, except for a few possible exceptions, there is no direct contact between ZnSe and BaF_2 layers, an advantage that can reduce the chemical reaction between the adjacent layers.

Though the deposition parameters, such as deposition rate, vacuum of the chamber and the emission current were kept steady, the thicknesses of BaF_2 thin films were not uniform. The top layers of BaF_2 thin films in the DBR structure were more compressed compared to the bottom layers. It is believed the lattice mismatch during the thin film deposition accumulates strain at the interface that causes the BaF_2 thin films to deform [107, 118, 123]. The deformation of BaF_2 thin films was more pronounced in the case of abrupt interface DBR mirror.

The surface roughness between the adjacent multilayers is another factor that has effect on the overall performance of the DBR mirrors. It is observed from the TEM images, the abrupt interface DBR mirror has more cracks and delamination that might arise from lattice mismatch induced defects in the multilayer DBR structure.

7.4.1. STEM-EELS study of SiO and SiO_2 thin films

The interface grading SiO nano-thick thin films have been analyzed using a combined an STEM and EELS system. It has been known that SiO source material can form two oxides, either SiO or SiO_2, hence a careful atomic compositional investigation should be performed to identify the stochiometry [102]. The assessment is very critical since the stochiometry affects the overall optical performance of the designed DBR mirror. The purpose of the STEM-EELS study is to distinguish between SiO and SiO_2 thin films on the basis of electron energy loss near edges (ENLES) structure using the silicon edge around 100 eV.

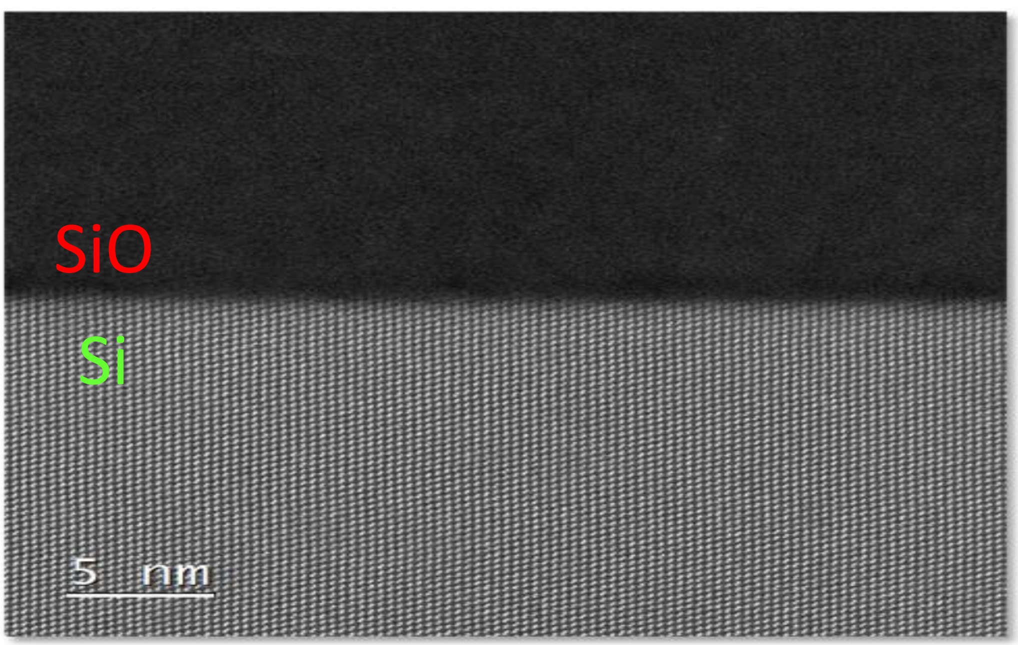

a) SiO/Si interface, deposition rate of SiO thin film ~ 12 Å/sec.

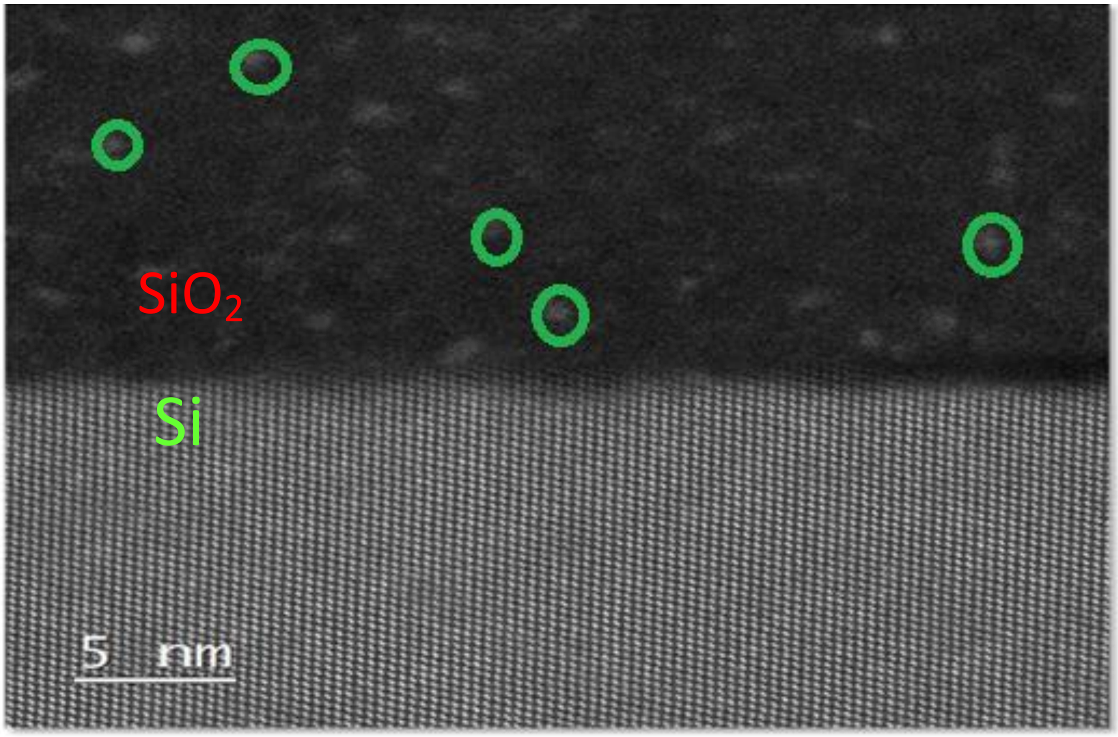

b) SiO_2/Si interface, deposition rate of SiO_2 thin films ~ 2 Å/sec.

Figure 38. HAADF-STEM images showing (a) SiO/Si and (b) SiO_2/Si interfaces.

As can be seen in Fig. 38, HAADF-STEM was employed to understand chemical composition of SiO/Si and SiO_2/Si interfaces. In this work, the SiO source material was deposited on two silicon substrates at two different deposition rates ~ 2 Å/sec and ~ 12 Å/sec. The micrographs show that the rate of deposition has a significant role in affecting the atomic composition of the grading layer.

It has been revealed from the micrographs that when the deposition rate of the SiO source material is reduced, it will increase the formation of precipitates that increases percentage of the oxygen content in the thin film that later changes its stoichiometry. The highlighted green circles in Fig. 38(b) are indications of the precipitates that are formed when we decrease the deposition rate of the thin film.

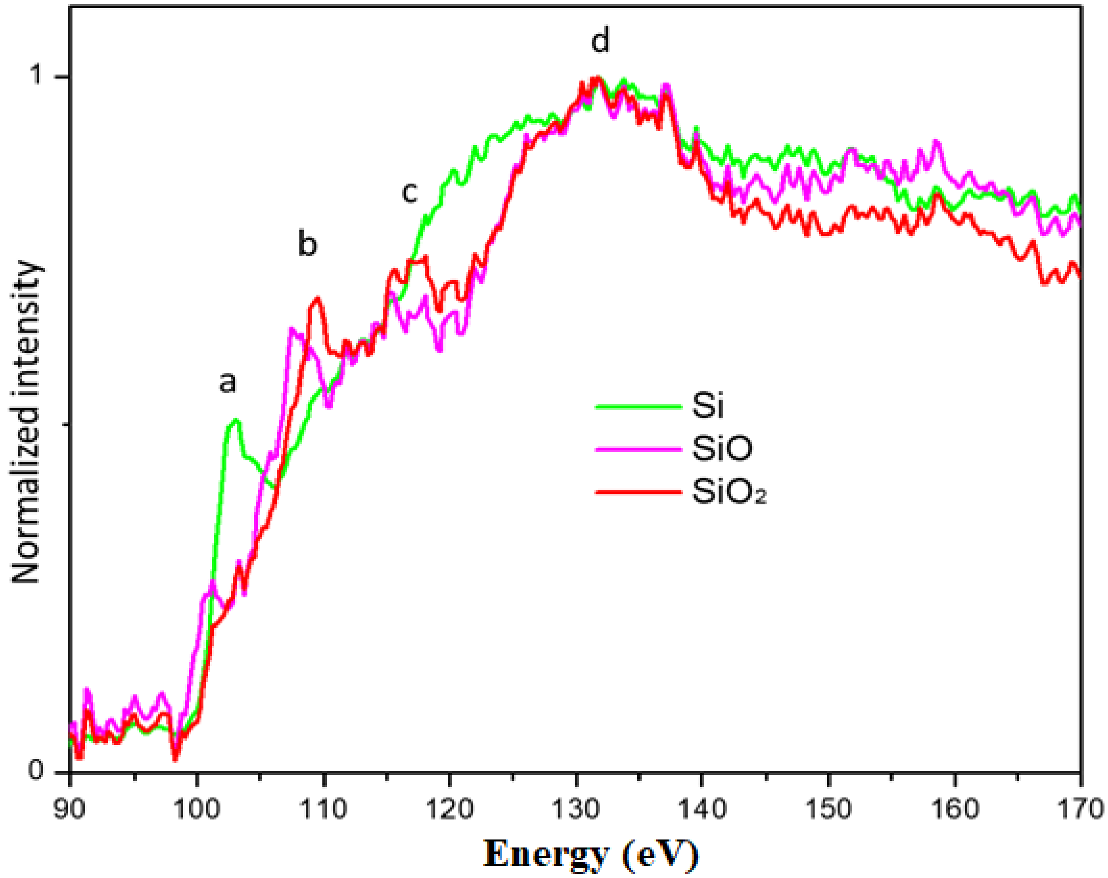

Figure 39. Normalized EELS spectra extracted from the Si-L edge for Si (substrate), SiO and SiO_2 thin films respectively. Features on the edge has been labeled for identification purposes.

The two silicon oxides, SiO_2 and SiO, that can form from silicon monoxide source material during electron beam deposition have been distinguished using EELS. By analyzing normalized EELS spectra, the SiO Si-L edge has a pre-peak "a" like the silicon substrate, while SiO_2 does not have Si-L edge. The SiO Si L-edge has broader and slightly shifted "b" peak compared to the SiO_2 Si-L edge. The SiO_2 Si L-edge shows a higher "c" peak compared to the SiO Si-L edge. Based on our normalized EELS spectra results and the literature data, we can conclude that by controlling the deposition rate of the thin films, we can adjust the stoichiometry of the interface grading layer. A silicon monoxide thin film deposited at a rate ~ 12 Å/sec was appropriate for our device requirements.

7.5. Optical testing of DBR thin films

The optical performance of DBRs was characterized using Fourier transform infrared (FTIR) specctroscopy. It offers the advantages of fast speed and sensitivity compared to the conventional dispersive instruments. Unlike grating-based spectrometers, a FTIR spectrometer collects and scans all wavelengths simultaneously. It obtains infrared spectra by collecting an interferogram on a sample signal. A mathematical convolution of the Fourier transform is applied to convert the interferogram into a final spectrum that matches intensity versus frequency [108, 110].

Omnic software was used to test the DBR mirrors. Optical tests were performed using the following procedure. Initially, a background spectrum without a sample is collected. This spectrum provides a response of the spectrometer that takes into account the performance of the infrared light source, the intereferometer, and the detector, as well as carbon dioxide and water molecules present at a specfic wavelengths as shown in Figure 40.

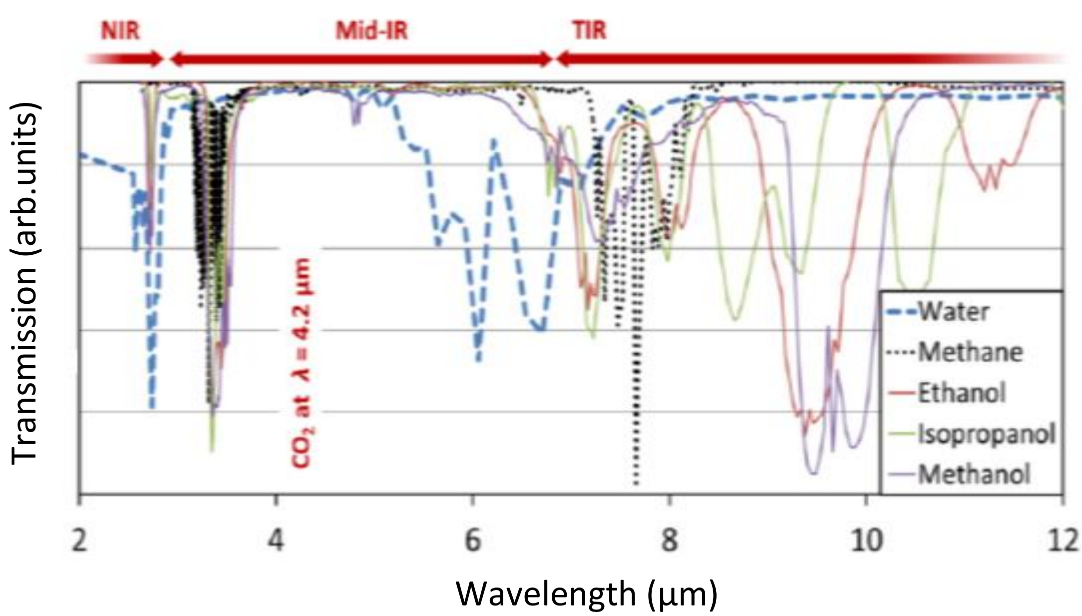

Figure 40. The absorption spectra of common hydrocarbons, water vapor and CO_2 gas. Data source: www.webbook.nist.gov

To collect the transmittivity and reflectivity of a DBR, first the DBR mirror is loaded on the sample holder of the FTIR spectrometer, then a beam from the source is focused and directed to the sample to obtain the maximum signal. The output of the FTIR includes the percentage of transmission, reflection , and absorption as a function of wavelength [108, 109].

7.5.1. Comparative study of the optical performance of abrupt and graded interface DBR mirrors

In this section, the optical performance of abrupt and graded interface DBR mirrors are studied and compared. The transmission, reflection, absorption, and stop band zone, are the main parameters considered to highlight the optical performance of various DBR mirrors.

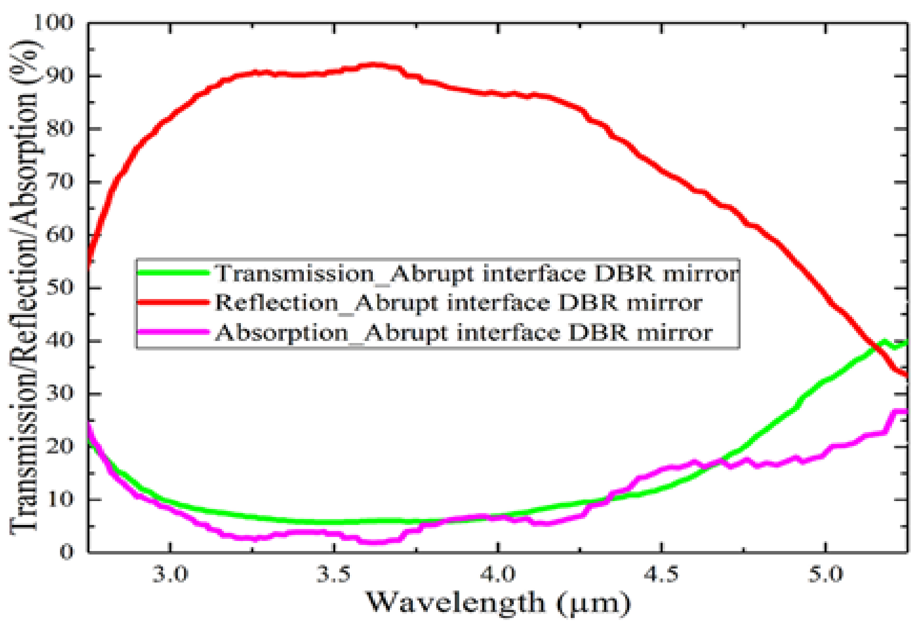

(a)

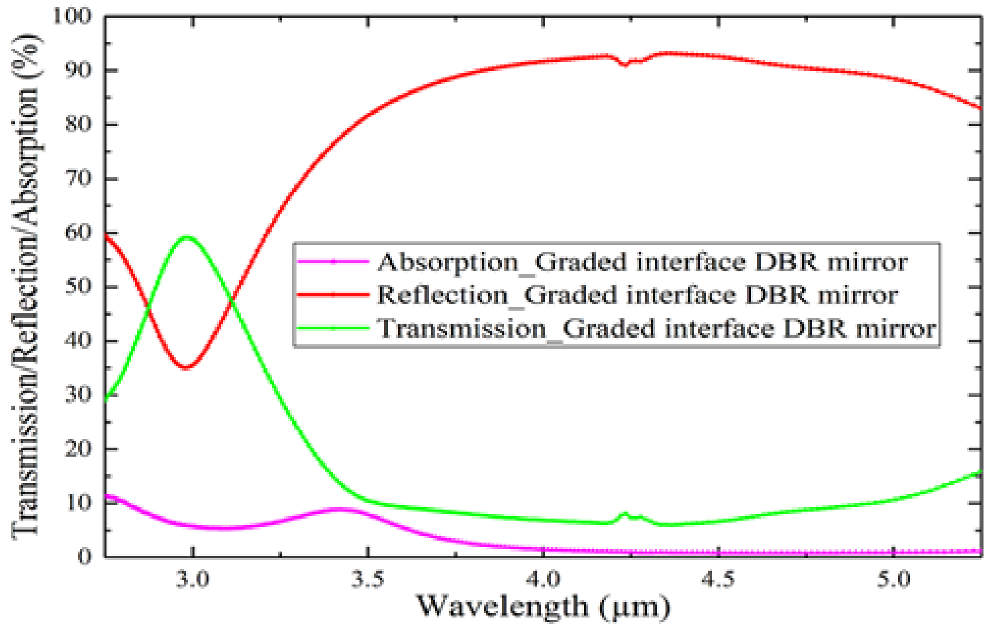

(b)

Figure 41. Transmission, reflection and absorption of three stacks of alternating ZnSe/BaF_2 thin films. (a) abrupt interface DBR mirror and (b) graded interface DBR mirror

The optical performance of abrupt and graded interface micro-mirrors comprised of three stacks of alternating dielectric multilayers are demonstrated in the above figures. As illustrated in Fig. 41, though abrupt interface DBR micro-mirror with a design [ZnSe/BaF_2/ZnSe/ BaF2/ZnSe] has achieved a reflection of ~ 90% at the target wavelength, the mirror is not a broadband reflector in the target region, which can limit the operability of the mirror in the target wavelength range. The abrupt interface DBR mirror has also suffered from an absorption loss that has an impact in reducing the transmission of the optical filter. Hence the absorption loss of the mirror should be mitigated, and it is one of the goals of this thesis to address this issue.

The graded interface DBR mirror that is comprised of multilayers with a design [ZnSe/SiO/BaF_2/SiO/ZnSe……ZnSe] showed better optical performance compared to the abrupt interface DBR mirror in the MWIR region. The graded interface mirror achieved a reflection of ~ 93% in the MWIR region. The absoption loss of graded interface DBR mirror at the central wavelength, 4 µm was ~ 1.5 %, very low compared to ~ 10 % absorption loss of abrupt interface DBR mirror. The graded interface DBR mirror also has a wider stop zone (high reflection zone) in the MWIR region (3-5 µm), that allows the mirror to have a wider band width. This design is recommended for the application of tunable band-pass optical filters since it has a broader bandwidth, that allows operability at the target MWIR region.

It is noted in the literature that in the case of abrupt interface DBR mirrors, there is a high chance of chemical reaction that forms a new chemical species at the interface between the adjacent layers [110]. In this work, it is believed that the defects in the BaF_2 layers diffuse into the adjacent ZnSe layer and it forms BaSe compound that might have an effect in increasing free carrier concentration in the multilayers and lower down the optical performance of the abrupt interface DBR mirrors. Hence, a nano-thick interface grading technique was suggested to mitigate this issue. It is believed that the free carrier absorption loss has been mitigated by the nano thick silicon monoxide interface grading layer.

7.6. Assembly of Fabry-Perot optical filters

Various Fabry-Perot optical filters comprised of abrupt interface and graded interface DBRs have been assembled by bonding two parallel DBR mirrors using an adhesive wafer bonding technique. In this technique, SU-8 photoresist has been deposited in the supporting layer of the bottom mirror and the mirrors were bonded by reflowing the photoresist while increasing the temperature and applying a bonding pressure as discussed in Chapter 4 of this thesis.

The Fabry-Perot optical filters have been designed to operate at the MWIR region with central wavelength ~ 4 µm. Depending on the optical cavity thickness, a specific wavelength will be transmitted.

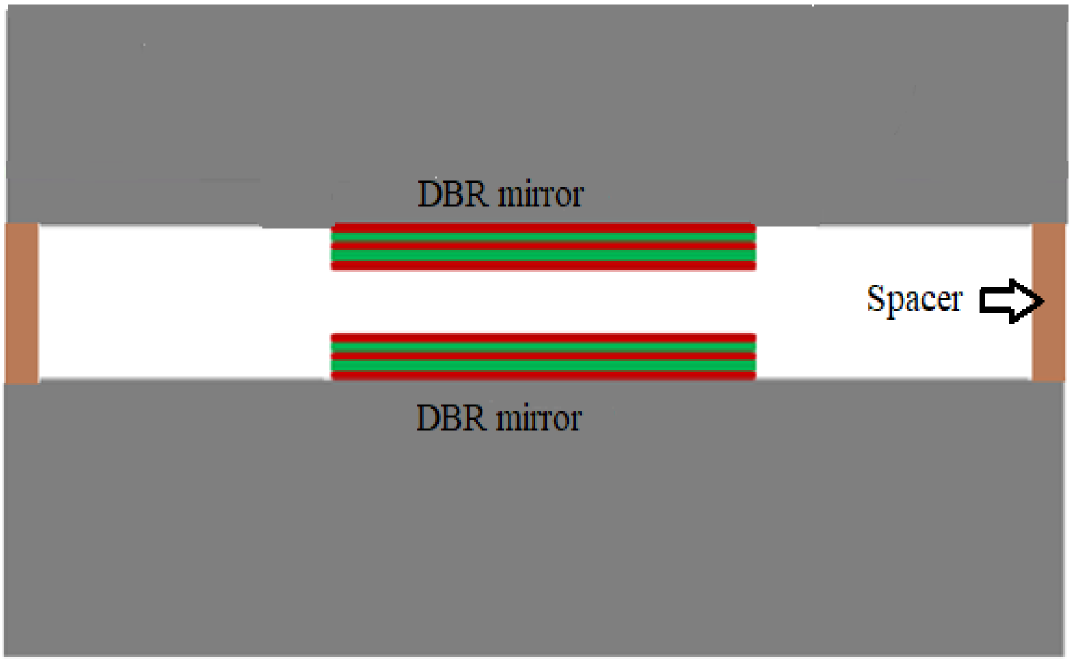

Figure 42. Schematic of assembled fixed cavity optical filter

The Fabry-Perot optical filter was designed to have an optical cavity of thickness 2µm, for the operation of first cavity mode in the target central wavelength (~ 4 µm). The primary purpose of optical filters is to isolate and transmit the target wavelength from an incident signal. The isolation of the target wavelength is realized through a combination of QWOT thin film design and a half wavelength cavity thickness [111, 112].

7.6.1. Comparative study of abrupt interface and graded interface Fabry-Perot optical filters

The optical performance of the assembled abrupt interface and graded interface Fabry-Perot optical filters were assessed and a comparative study between the assembled optical filters was conducted.

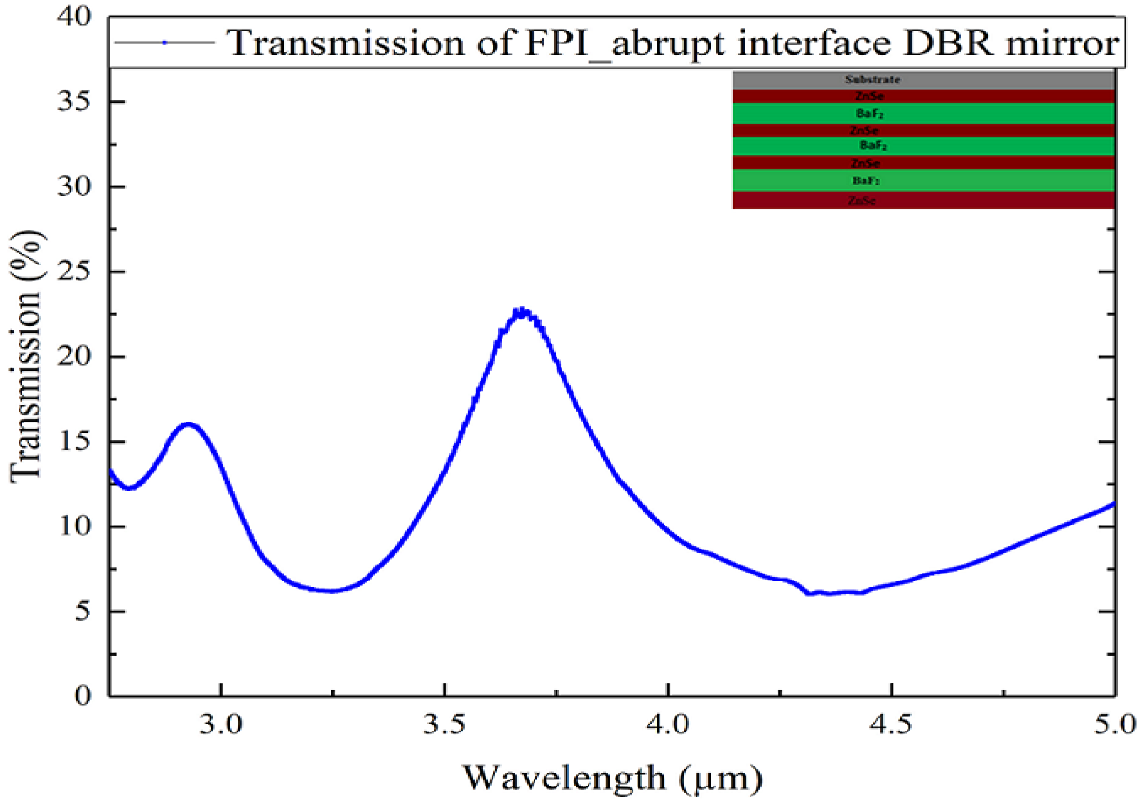

(a). Abrupt interface Fabry-Perot optical filter

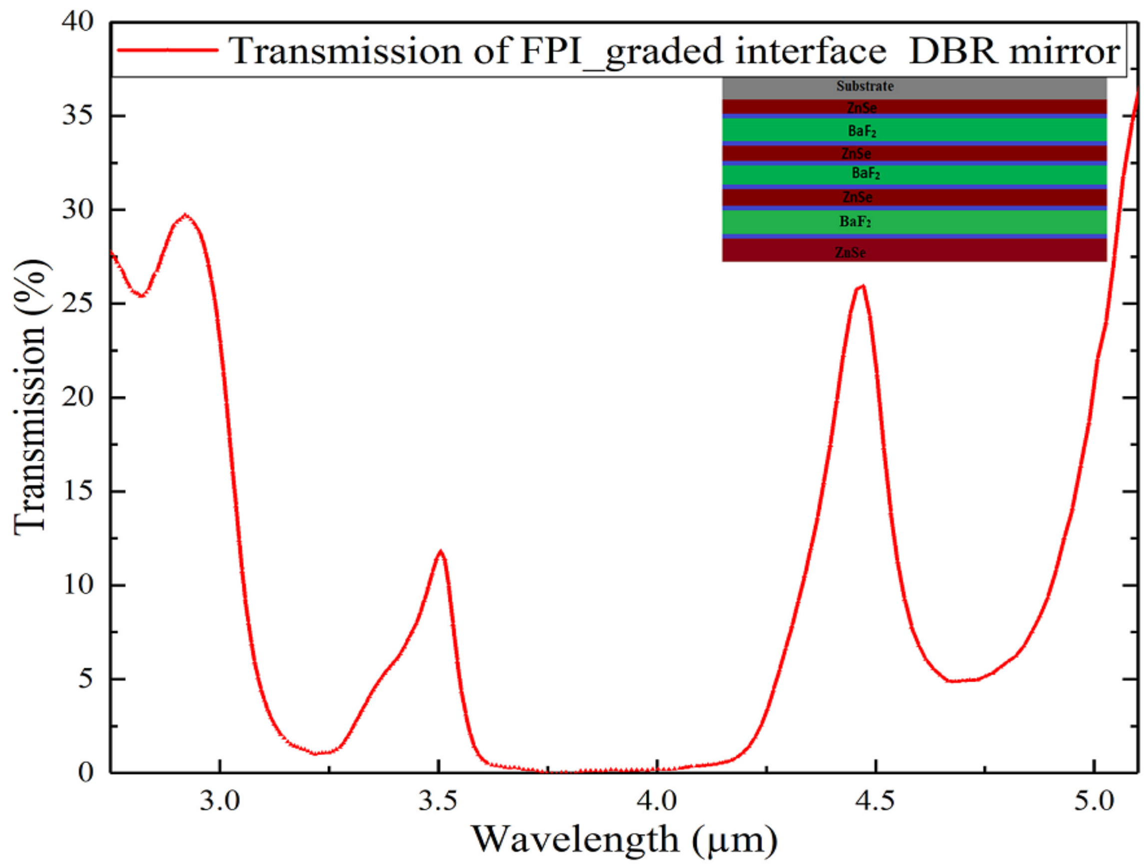

(b). Fabry-Perot optical filter with graded interface DBR mirror

Figure 43.Transmission of abrupt interface and graded interface optical filters in MWIR region.

The optical performance and the main figures of merit of the optical filters is presented below.

Type of DBR mirror	Reflection (%)	Transmission peak (%)	FWHM (μm)
Abrupt interface mirror	90	22	0.45
Graded interface mirror	93	26.5	0.2

Table IX. The reflection, transmission peak and FWHM of Fabry-perot optical filters.

It is studied in the literature and was discussed in Section 2.4 of this work that the optical transmission of Fabry-Perot optical filters depends on the absorption loss and transmission of DBR mirrors as mentioned in Eq. (2.33), $T_{FPI} \cong \left(\frac{1}{(1+\frac{A}{T})^2}\right)_{\mathrm{DBR}}$, based on our experimental data, the graded interface DBR mirrors have a lower absorption loss to transmission ratio, ($\frac{A}{T}$), compared to abrupt interface DBR mirrors at the target wavelength. This later optimizes the transmission of the graded interface optical filters.

It is also well known and studied, the higher the reflectivity of the DBR mirrors, the sharper and narrower the transmission peaks of the optical filters. This effect was highlighted using the FWHM of optical filters given by, $\mathrm{FWHM} = \frac{\lambda(1-\mathrm{R})}{2\pi\sqrt{\mathrm{R}}}$. In this work, the graded interface DBR mirrors showed a higher reflection of ~ 93% that has an effect in narrowing the FWHM, that will increase the finesse of optical filters. In this study, the reflective finesse has increased by ~ 225% compared to the abrupt interface optical filters.

As shown in Table IX, the graded interface Fabry-Perot optical filters had achieved a better optical performance compared to abrupt-interface optical filters. We presume the SiO grading interface layer in the DBR multi-layer structure has minimized the lattice mismatch defects, which are believed to be one of the major limitations that degrades the optical performance of abrupt interface DBR mirrors.

There is a wavelength shift between the transmission peaks of the optical filters, the graded interface filter showed a central wavelength ~ 4.3 µm, and the abrupt interface filter showed a central wavelength ~ 3.75 µm. The wavelength shift in the transmission peak is believed to arise mainly due to differences in the thicknesses of optical cavities of the optical filters caused by parallel deviation defects during the assembly of DBR mirrors.

7.7. Temperature dependent optical characterization of Fabry-Perot optical filters

Understanding how the temperature affects the optical transmission and spectral resolution of optical filters is critical for designing practical devices. In this thesis, the optical transmission of MOEMS-based Fabry-Perot optical filters were studied at different temperatures that range from 120K to 300K.

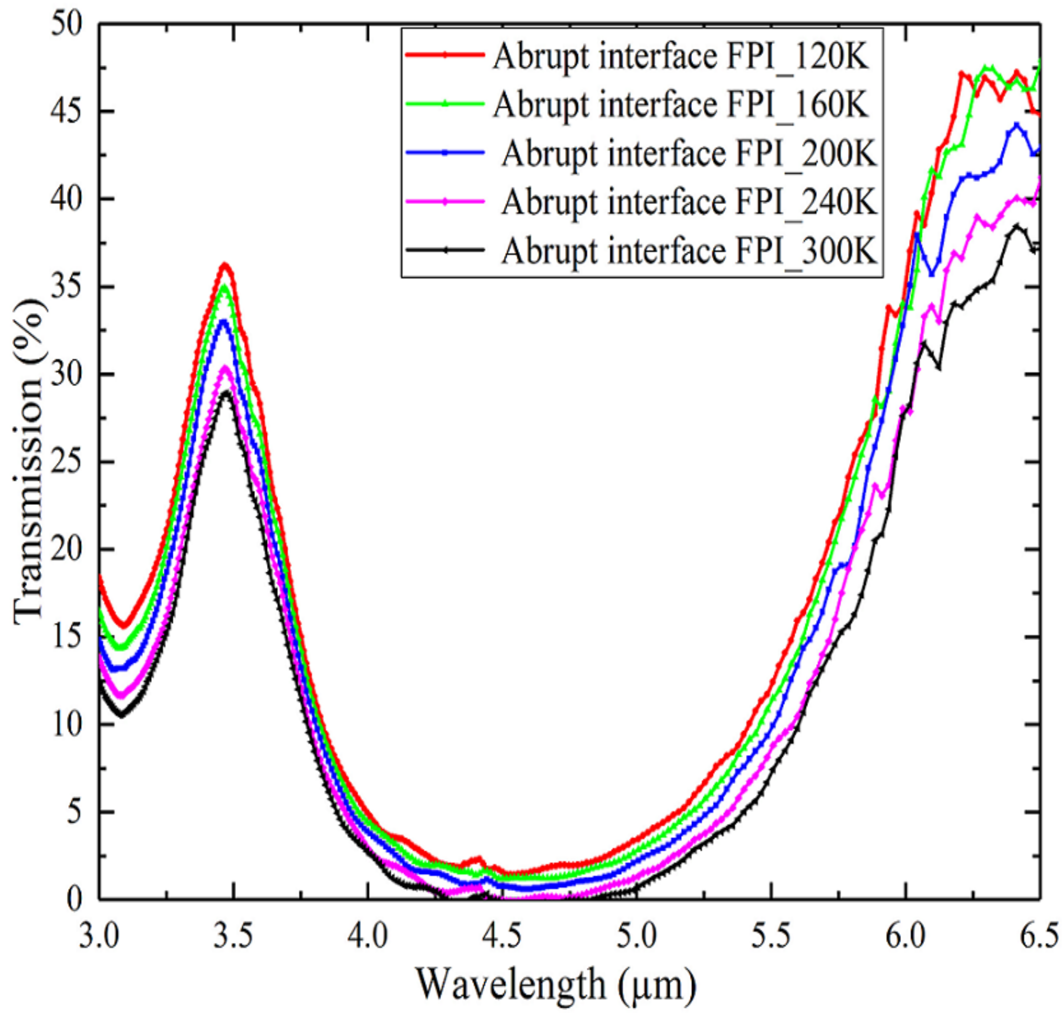

(i)

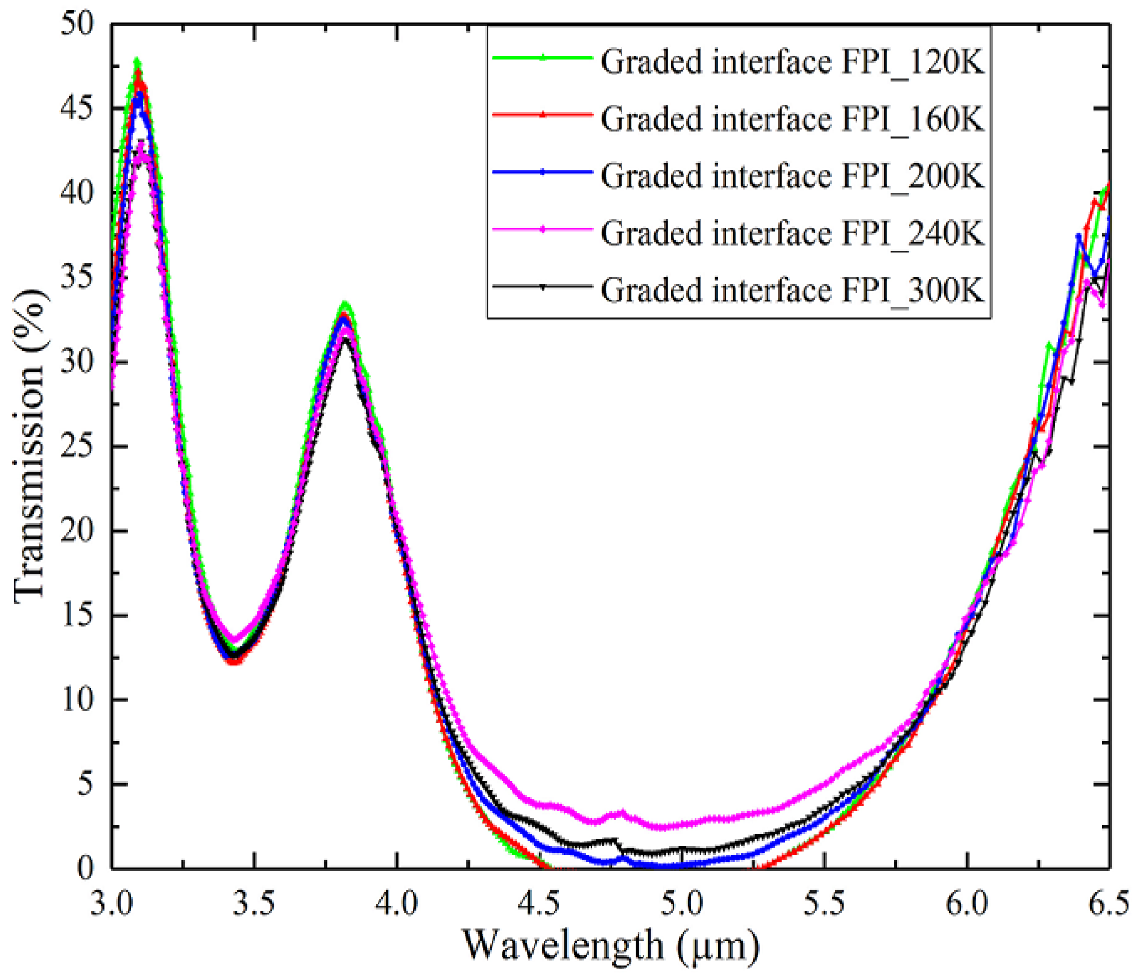

(ii)

Figure 44.Temperature dependent optical transmission of (i) abrupt interface optical filter, and (ii) graded interface optical filter

The transmission peak of the abrupt interface Fabry-perot optical filters depends on temperature. When temperature increases,thicknesses of multilayers increase due to thermal expansion.This will later shift the transmission peaks of abrupt interface optical filters to a longer wavelength when increasing temperatures. Whereas the transmission peaks of graded interface filters increased only by a very small amount of percentage as we cool down from room temperature to 120K.

We believe the free carrier absorption loss that occurs as a result of unintentional dopants and lattice mismatch induced defects is dominant compared to the intrinsic absorption losses, which consists of electronic absorption and phonon absorption in the target MWIR region. Since the DBR materials selected in this work are wide band gap materials, ~ 2.58 eV and ~ 9.1 eV for ZnSe and BaF_2 thin films, respectively, a mid wavelength infrared signal at the target central wavelength ~ 0.31eV cannot undergo electronic (interband) absorption, since its value is very low when compared with the band gap of the respective selected DBR thin films. The phonon absorption that occurs as a result of coupling between the thermally induced vibrations of constituent atoms and incident infrared radiation is also very low since the concentration of thermally induced vibrations is expected to be low in these temperature ranges (120 K- 300 K).

Our results show that the abrupt interface optical filter has achieved a maximum optical transmission peak ~ 37% at 120 K. The transmission peaks are more sharp and have narrower FWHM as temperature is reduced, an indication that the finesse of the optical filters is optimized. It is believed that cooling down the Fabry-Perot optical filter has frozen out the carriers and reduced the carrier concentration in abrupt interface Fabry-Perot optical filters, which suppresses the free carrier absorption loss.

8. Conclusions

8.1. MOEMS-based micro-actuators

The MOEMS movable membranes that are critical for the realization of micro-actuators have been fabricated from SOI wafers, a three-layered wafer that is composed of single crystalline device layer, buried silicon dioxide insulating layer and bulk handle wafer. SOI wafers were chosen since they have the advantage of eliminating parasitic capacitance and leakage currents, a major drawback in bulk silicon technology that degrades the performance of electronic devices.

SU-8 (3025), a negative photoresist that offers many important features such as high aspect ratio, near UV processing, and an insulating intermediate layer has been deposited on a bulk stationary membrane to act as a spacer. The micro-actuator is then assembled by bonding the stationary bulk wafer with the movable membrane chip using adhesive wafer bonding technique, by applying pressure to the chips while varying the bonding temperature.

capacitive MOEMS-based parallel plate micro-actuators were assembled and tested using parallel electrostatic actuation method. The mechanical stiffness constants and sensitivities of micro-actuators with three different x-beam designs have been estimated based on the snap-in conditions. The x-beam with serpentine design showed the highest sensitivity, resulting in the lowest stiffness constant. The serpentine design, which causes accumulation of charge on the sharp corners, increases the electrostatic force felt by the x-beam, this in turn plays a role in minimizing its stiffness constant and has an effect of increasing the displacement. The impact of sensitivity should be considered when designing micro actuators. Using a smaller device layer thickness and meandering arms are recommended to achieve better sensitivities. This gives the advantage of practical lower operating voltages which can be useful for low power devices. Also, meandering arms or anchor can be used in other types of micro-actuator designs and can be applied to systems that require closely packed micro-actuators during integration.

8.2. Graded interface DBR mirrors in the MWIR region

Interference-based Fabry-Perot optical filters were designed to transmit incident light in the MWIR region. A DBR, a one-dimensional photonic crystal, is an essential component of the optical filters. The DBR is comprised of a pair of dielectric materials with alternating refractive indices. The central wavelength of the DBRs is always controlled by changing the design of multilayers. The percentage of absorption loss in the target wavelength also limits the application of different materials. Many dielectric thin films have absorption peaks in the MWIR region that makes the selection of materials challenging. In addition, high refractive index contrast is required to achieve a mirror with high reflection band zone.

In this work, we investigated the optical performance of electron beam deposited ZnSe and BaF_2 -based DBR mirrors in the MWIR region. It was identified that absorption loss affects the optical performance of the distributed Bragg mirrors. Some absorption loss always arises from the free carrier absorption in the multi-layers. A DBR mirror made from abrupt interface alternating thin films suffered an absorption loss conjectured to be from interdiffusion of atoms between the multi-layers. Hence, there is a need to minimize the free carrier absorption loss by designing the appropriate interface grading layer. A nano-thick amorphous silicon monoxide interface grading layer, ~ 80 nm thick, was deposited at the interface between the polycrystalline thin films with a goal to minimize the absorption loss and stop the interdiffusion of atoms. It showed improved performance of the optical filters. The silicon monoxide layer also served as an anti-reflection coating layer to minimize the Fresnel optical loss at the interface between the multilayers.

It was noted that while depositing the SiO interface grading layer, a careful compositional investigation needed to be performed since silicon monoxide has the potential to form two different oxides, either silicon dioxide or silicon monoxide. We performed a compositional analysis using a STEM- EELS system and identified that the deposition rate of silicon monoxide source material affects its stoichiometry. It has been recommended from our study that to get the true silicon monoxide thin films, the deposition rate should be held at a rate ≥ 12 Å/s.

The graded interface Fabry-Perot optical filters (with SiO interfacial layers) showed a better optical performance and spectral resolution compared to the abrupt interface optical filters (without SiO interfacial layers) in the MWIR region.

8.3. Future work and recommendations

High-quality DBRs were fabricated and assembled to form Fabry-Perot optical filters. It still needs more investigation to solve the challenges in the realization of tunable optical filters for the application of hyperspectral sensing. The filters studied in this work are applicable in various novel optoelectronic devices like micro-cavity structures, optical lasers, and optical switches.

The optical properties of DBR multilayers should be optimized for the desired optical filtering application. It is believed that free carrier absorption loss is a major drawback that degrades the optical transmission and spectral resolution of FPFs. Hence grading the interface of the multi-layers with a nano-thick silicon monoxide thin film is recommended to mitigate the free-carrier absorption by minimizing the interdiffusion of atoms between the layers.

The intended application of this work is to embed two-dimensional atomic crystals with highly reflective DBRs in forming a micro-cavity structure. Two dimensional atomic crystals such as black phosphorous and graphene have showed a promising photon absorption. The photon absorption can be enhanced by inserting these materials inside DBR cavities in forming micro-cavities. The DBR-based microcavity structure is recommended since it offers a lower cost and can be applied in polaritonic devices that demand strong-light matter interaction.

We also propose a low-cost next generation micro-cavity structure that can be formed by embedding two dimensional atomic crystals into a DBR structure. The proposed design can be used to increase absorption in 2D materials, when it is embedded inside the cavity of DBR structures. The proposed cavity structures have promising potential to increase efficiency of next generation 2D MWIR infrared sensors and photodetectors.

The suggested future work also involve assembly of tunable MWIR optical filters with infrared photodetectors in the MWIR region for the hyperspectral imaging and multi-spectral sensing applications to detect harmful chemical agents in the target wavelength.

9. Bibliography

[1]. M. Muallem, A. Palatnik, G. D. Nessim, and Y. R. Tischler, Room temperature fabrication of dielectric Bragg reflectors composed of CaF2/ZnS multilayered coating, ACS Appl. Mater. Interfaces, 7, 474 (2015).

[2]. G. Gerlach and W. Dötzel. Introduction to Microsystem Technology: A Guide for students, Chichester, John Wiley & Sons, 2008.

[3]. Mohamed Gad-el-Hak: MEMS: Applications, CRC press, 2005.

[4]. N. Maluf and K. Williams, Introduction to microelectromechanical systems engineering, Artech house, 2004.

[5]. J. Buhler, F-P Steiner, and H. Baltes, Silicon dioxide sacrificial layer etching in surface micromachining., J. Micromech. Microeng., 7, R1 (1997).

[6]. G. Hernandez, Fabry-Perot Interferometers, London, Cambridge University Press, 1988.46.

[7]. J. Shelby, Optical materials color filter and absorption glasses, Ency-clopedia of Modern Optics, edited by R. D. Guenther, Elsevier, Oxford, 440 (2005).

[8]. R. A. Crocombe, D. C. Flanders, and W. Atia, Micro-optical instrumentation for process spectroscopy, Proc. SPIE, 5591, 11 (2004).

[9]. S. D. Smith, and O. S. Heavens, A tunable infrared interference filter, J. Sci. Instrum., 34, 492 (1957).

[10]. C. Lei, T. J. Rogers, D. G. Deppe, and B. G. Streetman, J. Appl. Phys., 69, 7430 (1991).

[11]. N. Tkachenko, Optical spectroscopy: methods and instrumentations, Elsevier Science, 1st edition, Amsterdam, 75 (2006).

[12]. D. A. Kozak, B. Fernandez, S. Velicu, J. Kubby, Prototyping of MWIR MEMS-based optical filter combined with HgCdTe Detector, Proc. SPIE, 7594, 75940W1 (2010).

[13]. J. Hodgkinson, and R. P. Tatam, Optical gas sensing: a review, Measurement Science and Technology, 24, 75940W1 (2013).

[14]. H. Saari, V. V. Aallos, C. Holmlund, J. Mäkynen, B. Delaure, K. Nackaerts, and B. Michiels, Novel hyperspectral imager for lightweight UAVs, Proc. SPIE, 7668, 766805 (2010).

[15]. D. Landgrebe, C. Haake, T. Höpfner, S. Beutel, B. Hitzmann, T. Scheper, M. Rhiel, and K. F. Reardon, On-line infrared spectroscopy for bioprocess monitoring, Appl. Microbiol. Biotechnol., 88, 11(2010).

[16]. R.F. Wolffenbuttel, MEMS-based optical mini and microspectrometers for the visible and infrared spectral range, Journal of micromechanics and microengineering, 15, S145 (2005).

[17]. M. Cardona, P.Y. Yu, Comprehensive semiconductor science and technology, Springer, New York, 125 (2011).

[18]. J. M. Vaughan, The Fabry-Perot interferometer: History, theory, practice and applications, Taylor & Francis Group, New York, 1st edition, 1989.

[19]. A. Manenkov, and V. P. Bykov, On open electromagnetic resonators: relation between interferometers and resonators, Quantum Electronics, 40, 217 (2010).

[20]. G. W. Chantry, The use of Fabry-Perot interferometers, etalons and resonators at infrared and longer wavelengths - G93 an overview, J. Phys E: Sci. Instrum.,15, 3 (1982).

[21]. M. Born, and E. Wolf, Principles of Optics, 6th ed. (reprinted with corrections), Pergamon, Oxford, UK, 325 (1993).

[22]. C. L. Tan, and H. Mohseni, Emerging technologies for high performance infrared detectors, Nanophononics, 7, 69 (2018).

[23]. Q. Guo, A. Pospischil, M. Bhuiyan, H. Jiang, H. Tian, D. Farmer, B. Deng, C. Li, S. J. Han, H. Wang, Q. Xia, T. P. Ma, T. Mueller, and F. Xia, Black phosphorous mid-infrared photodetectors with high gain, Nano lett., 16, 4648 (2016).

[24]. Y. Q. Diana, H. D. J. Felipe, G. L. Steven, and S.G, Optical spectrum of MoS_2: Many body effects and diversity of exciton states, Phys. Rev. Lett, 111, 216805 (2013).

[25]. W. Zhang, C. P. Chuu, J. K. Huang, C. H. Chen, M. L. Tsai, Y. H. Chang, C. T. Liang, Y. Z. Chen, Y. L. Chueh, J. H. He, M. Y. Chou, L. J. Li, Ultrahigh-gain photodetectors based on atomically thin graphene-MoS_2 heterostructures, Sci Rep., 3826, 1 (2014).

[26]. C. Weisbuch, M. Nishioka, A. Ishikawa, and Y. Arakawa, Observation of the coupled exciton-photon mode splitting in a semiconductor quantum microcavity, Phys. Rev. Lett., 69, 3314 (1992).

[27]. D. Goldberg, I. D. Lev, A. Lisyansky, Z. Shi, V. M. Menon, T. Vadim, Y. Michael, and O. Serge, Exciton-lattice polaritons in a multiple quantum well based photonic crystal., Nat. Photonics, 3, 662 (2009).

[28]. M. Wu, G. Li, W. Yuen, and C. C. Hasnain, widely tunable optical filter at 1.5 µm micromechanical optical filter using AlO_x/AlGaAs DBR, Electronics Letters, 33, 1702 (1997).

[29]. J. Peerlings, R. Riemenschneider, V. N. Kumar, M. Strassner, J. Pfeiffer, V. Scheuer, J. Daleiden, K. Mutamba, S. Herbst, H. Hartnagel, and P. Meissner, Two-chip InGaAs/InP Fabry-Perot p-i-n receiver for WDM systems, Photonics Technology Letters, IEEE, 11, 260 (1999).

[30]. J. J. Wierer, A. David, and M. M. Megens, III-nitride photonic-crystal light emitting diodes with high extraction efficiency, Nature Photonics, 3, 163 (2009)

[31]. T. Moudakir, S. Gautier, S. Suresh, M. Abid, Y. E. Gmili, G. Patriarche, K. Pantzas, D. Troadec, J. Jacquet, F. Genty, P. Voss, and A. Ougazzaden, Suppression of crack generation in AlGaN/GaN distributed Bragg reflectors grown by MOVPE, Journal of Crystal Growth, 12, 46 (2013).

[32]. S. Xia, D. Chen, Z. Qi, X. He, C. Peng, X. Chen, C. Bian, L. Qu, and J. Sun, Application of nanomaterials in sensors and diagnostics, Microelectromechanical Sensors, Springer, 207 (2012).

[33]. N. Tkachenko, Optical spectroscopy: Methods and Instrumentations, Elsevier Science, 1st edition, 2006.

[34]. E. Hecht, Optics, Addison-Wesley, 4th edition, 2002.

[35]. H. A. Macleod, Thin film optical filters, Institute of Physics publishing, 3rd edition, 2001.

[36]. M. L. Morley, S. Velicu, Y. Chang, C. H. Grein, D. A. Kozak, B. Fernandez, J. Kubby, N. Gupta, Design and fabrication of Fabry-Perot filters for infrared hyperspectral imagers, Journal of Micro/Nanolithography, MEMS and MOEMS, 13, 01111161 (2014).

[37]. P. D. Atherton, N. K. Reay, J. Ring, and T. R. Hicks, Tunable Fabry-Perot filters, Opt. Eng., 20, 806 (1981).

[38]. J. P. Colinge, Silicon-on-insulator technology: materials to VLSI, Kluwer academic publishers, 2nd edition, 32 (1997).

[39]. D. K. Sadana, and M. Current, Fabrication of silicon-on-insulator (SOI) wafers using ion implantation, Ion implantation science and technology, edited by J. F. Ziegler, Ion Implantation Technology, 341 (2000).

[40]. S. Tachi, K. Tsujimoto, K. Ninomiya, K. Suzuki, and S. Okudaira, Low temperature reactive ion etching and microwave plasma etching of silicon, Applied physics letters, 52, 616 (1987).

[41]. S. Wolf, and R. N. Tauber, Silicon processing for the VLSI era, process technology, lattice Press, 1, 1986.

[42]. B. E. Volland, Profile simulations of gas chopping etching processes: model development and comparison with experiments, doctoral dissertation, Universität Kassel, Germany, 2004.

[43]. O. Ataro, Micro-electromechanical structural design and optimization of vertical cavity photonic devices with wide continuous tuning, doctoral dissertation, Universität Kassel, Germany, 2005.

[44]. Y. Uenishi, M. Tsugai, and M. Mehregany, Micro-opto-mechanical devices fabricated by anisotropic etching of (110) silicon, Journal of Micromechanics and Microengineering, 5, 305 (1995).

[45]. B. Bilenberg, T. Nielsen, B. Clausen, and A. Kristensen, PMMA to SU-8 bonding for polymer-based lab-on-a-chip systems with integrated optics, J. Micromech. Microeng, 14, 814 (2004).

[46]. Y. Z. Xiao, G. Y. Wu, Z. H. Li, G. B. Zhang, Y. L. Hao. Y. Wang, Silicon–glass wafer bonding with silicon hydrophilic fusion bonding technology Sensors Actuators A, 72, 46 (1999).

[47]. L. Yu, F. Tay, G. Xu, B. Chen, M. Avram, C. Iliescu. Journal of Physics: International MEMS Conference Series 34, 776 (2006).

[48]. M. Alexe, and U. Gösele, Wafer bonding applications and technology, Springer-Verlag, Berlin, 2004.

[49]. C. Nobel, Industrial adhesives handbook, Casco Nobel, Fredensborg, Denmark, 1992.

[50]. E. S. Hung, S. D. Senturia, Extending the travel range of analog-tuned electrostatic actuators, Journal of microelectromechanical systems, 8, 497 (1999).

[51]. T. Iseki, M. Okumura, and T. Sugawara, Two-dimensionally deflection mirror using Electromagnetic-actuation, optical review, 189 (2006).

[52]. O. Cugat, J. Delamare, and G. Reyne, Magnetic micro-actuators and systems (MAGMAS), IEEE transactions on magnetics, 39, 3607 (2003).

[53]. W. P Robbins, High displacement piezoelectric actuator utilizing a meander line geometry-part II. Theory, IEEE transactions on ultrasonics, ferroelectrics, and frequency control, 38, 454 (1991).

[54]. J. Singh, T. Gan, A. Agarwal, Mohanraj, and S. Liw, 3D free space thermally actuated micro mirror device, sensors and actuators A, 123, 468 (2005).

[55]. J. Sam Jebar Kumar, E. Amoatey Tetteh, E. Paul Braineard, A study of why electrostatic actuation is preferred and a simulation of an electrostatically actuated cantilever beam for MEMS applications, International Journal of Engineering Sciences & Emerging Technologies, 6, 441 (2014).

[56]. G. T. Kovacs, Micro machined Transducers Sourcebook, McGraw-Hill Science, 1st edition, 1998.

[57]. S. E. Robert, Electromagnetics: History, theory, and applications, Wiley-IEEE Press, 1st edition, 1999.

[58]. H. Busta, R. Amantea, D. Furst, J. M. Chen, M. Turowski, and C. Mueller, A MEMS shield structure for controlling pull-in forces and obtaining increased pull-in voltages, Journal of micromechanical micro engineering, 11, 720 (2001).

[59]. M. Born, and E. Wolf, The handbook of optics, Pergamon, New York, 2nd edition, 1980.

[60]. P. Attia, M. Bontry, A. Bossehoeuf, and P. Hesto, Fabrication and characterization of electrostatically driven silicon micro beams, Journal of Microelectronics, 641 (1998).

[61]. J. Seeger, and B. Boser, Charge control of parallel-plate electrostatic actuators and the tip-in instability, Journal of microelectromechanical System, 12, 656 (2003).

[62]. W. C. Chuang, H. L. Lee, P. Z. Chang, and Y. C. Hu, Review on the modeling of Electrostatic MEMS, Sensors, 10, 6149 (2010).

[63]. A. F. Marques, J. C. Terré, and M. S. Andrei, Resonant pull in condition in Parallel-plate electrostatic actuators, Journal of microelectromechanical systems, vol. 16, 2007, pp. 1044-1053.

[64]. E. Garmire, "Theory of quarter-wave-stack dielectric mirrors used in a thin Fabry–Perot filter", Appl. Optics, 42, 5442 (2003).

[65]. D. I. Babic, and S. W. Corzine, Analytic expressions for the reflection delay, penetration depth, and absorptance of quarter-wave dielectric mirrors, IEEE, J. of Quantum Electronics, 28, 514 (1992).

[66]. S. O. Kasap, Optoelectronics and photonics, Upper Saddle River, EUA; Prentice-Hall, 3rd edition, 57 (2001).

[67]. T. H. Gessmann, and E. F. Schubert, High-efficiency AlGaInP light-emitting diodes for solid-state lighting applications, Journal of Applied Physics, 5, 2203 (1995).

[68]. O. Blum, L. J. Conway, S. K. Haywood, F. Mansoor, Molecular beam epitaxy grown AlAsSb/GaAsSb distributed Bragg reflector on InP substrate operating near 1.55 µm, Journal of vacuum science and technology B, 12, 1122 (1994).

[69]. A. Raab, and G. Springholz, Low-density InP-based quantum dots emitting around 1.5 µm, Appl. Phys. Lett, 77, 299 (2000).

[70]. J. H. Park, T. S. Sudarshan, Chemical vapor deposition., ASM International, 2nd edition, 2001.

[71]. D. M. Mattox, Handbook of physical vapor deposition (PVD) processing, Elsevier, 2nd edition, 2010.

[72]. L. L. Kazmerski, and D.M. Racine, Morphology and size distributions of islands in discontinuous films, Journal of applied physics, 46, 791 (1975).

[73]. K. S. Sree Harsha, Principles of physical vapor deposition of thin films, 1st edition, Elsevier, Boston, 2006.

[74]. A. E. Raid, and F. D. Barlow, Thin film technology handbook, McGraw Hill Academic publishers, New York, 1997.

[75]. M. A. Paul, and G. S. David, Optical properties of semiconductors, McGraw Hill Academic publishers, 2nd edition, 1994.

[76]. D. Attwood, B. Hartline, and R. Jhonson, The advanced light source: Scientific opportunities, Lawrence Berkeley Laboratory publication, 55, 1984.

[77]. E. Levenshetein, M. S. Rumyantsev, and M. Shur, Handbook series on semiconductor parameters, World scientific, New York, 1, 1996.

[78]. G. G. Macfarlane, T. P. Mclean, J. E. Quarrington, and V. Roberts, Fine structure in the absorption-edge spectrum of silicon, Physical Review, 111, 1245 (1958).

[79]. C. Kittel, Introduction to solid state physics, J. Wiley & Sons, 8th edition, 2005.

[80]. N. W. Ashcroft, and Mermin, Solid State Physics, Thomson learning, 2nd edition, 1976.

[81]. P. K. Basu, Theory of optical processes in semiconductors bulk and microstructures, oxford university press, 2003.

[82]. S. Oscini, optical properties of confined silicon structures, phys. stat sol (a), 170, 377 (1999).

[83]. Y. L. Chen, D. P. Yang, Mössbauer effect in lattice dynamics: Experimental techniques and applications, Wiley-VCH, 1st edition, 2007.

[84]. J. H. Simmons, and K. S. Potter, Optical materials, Academic press, 1st edition, 1999.

[85]. M. Fox, Optical properties of solids, Oxford university press, 2nd edition, 2001.

[86]. D. K. Schroder, R. N. Thomas, and J. C. Swartz, Free carrier absorption in silicon, IEEE J. Solid state Circuits SC-13, 1, 180 (1978).

[87]. C. M. Horwitz, and R. M. Swanson, The optical (free-carrier) absorption of a hole-electron plasma in silicon, Solid state Electron, 23, 1191 (1980).

[88]. J. I. Pankove, Optical processes in semiconductors, Dover Publications, New York, 74 (1971).

[89]. B. K. Ridley, Quantum processes in semiconductors, Clarendon press, Oxford, 3rd edition 217 (1982).

[90]. T. Tiedge, E. Yablnovitch, and G. D. Cody, Limiting efficiency of solar cells, IEEE Trans. Electron devices, 31, 711 (1984).

[91]. M. B. Clevenger, C.S. Murray, and D. R. Riley, Spectral utilization in thermophotovoltaic devices, Matter. Res. Soc. Proc, 485, 291 (1997).

[92]. A. Barron, I. Kurganskaya, A. Luttge, Physical methods in Chemistry and Nano Science, Connexions, 823 (2009).

[93]. T. M. Adams, and R. A. Layton, Introductory MEMS fabrication and applications, Springer, 173 (2010).

[94]. B. Balakrisnan, A. Nacev, J. M. Burke, A. Dasguptal, and E. Smela, Design of compliant meanders for applications in MEMS actuators, and flexible electronics, Smart Mater. Struct., vol. 3669, 149 (2012).

[95]. M. Lishchynska, C. O'mahony, O. Slattery, and R. Behan, Spring constant models for analysis and design of MEMS plates on straight or meander tethers, Sensor letters, 4, 200 (2006).

[96]. J. H. Jerman, D. J. Clift, and S. R. Mallinson, A miniature Fabry-Perot interferometer with a corrugated silicon diaphragm support, Sensors and actuators A, 29, 151 (1991).

[97]. X. Shiyun, S. Yugang, T. Chunsen, and C. Long, Research on Meander-type coupled structure of capacitively coupled power transfer system, WSEAS Transactions on Circuits and Systems, 14, 247 (2015).

[98]. G. Kedawat, S. Srivastava, V. K. Jain, P. Kumar, V. Kataria, Y. Agrawal, B. K. Gupta, Y. K. Vijay, Fabrication of artificially stacked ultrathin ZnS/MgF_2 multilayer dielectric optical filters, ACS Appl. Mater. Interfaces, 5, 4872 (2013).

[99]. A. Emadi, H. Wu, G.de Graaf, and R. Wolffenbuttel, Design and implementation of a sub-nm resolution micro spectrometer based on a linear-variable optical filter, Opt. Express, 20, 489 (2012).

[100]. H. Mao, K. K. M. B. D. Silva, M. Martyniuk, J. Antoszewski, J. Bumgarner, J. M. Dell, and L. Faraone, Ge/ZnS-based micromachined Fabry-Perot filters for optical MEMS in the longwave infrared, Journal of microelectromechanical systems, 20, 2109 (2015).

[101]. K. L Lear, and R. P. Schneider, Uniparabolic mirror grading for vertical cavity surface emitting lasers, Applied physics letters, 68, 605 (1996).

[102]. Hass, Schroeder, and Turner, Optical properties of silicon monoxide in the wavelength region 0.24 to 14 μm, Journal of the optical society of America, 44, 181 (1953).

[103]. H. Lüth, Solid surfaces, interfaces and thin films, Springer, 5th edition, 2010.

[104]. K. F. Bonhoeffer, Structure of amorphous silicon monoxide, Journal of applied physics, 43, 995 (1972).

[105]. M. A. Linnik, and A. Chirstou, Effects of Bragg mirror interface grading and layer thickness variations on VCSEL performance at 1.55 µm, Proc. SPIE, 4286, 1 (2001).

[106]. M. Musbach, Sensitivity of the absorbance and capacitive methods in measurement the number of cells in-vivo, Journal of medical physics and biophysics, 2, 40 (2015).

[107]. P. A. Gabrys, S. E. Seo, M. X. Wang, E. Oh, R. J. Macfarlane, and C. A. Mirkin, Lattice mismatch in crystalline nanoparticle thin films, Nano. Lett., 18, 579 (2018).

[108]. Z. M. Zhang, L. M. Hanssen, and R. U. Dalta, Polarization-dependent angular reflectance of silicon and Germanium in the infrared, Infrared Physics & Technology, 37, 539 (1996).

[109]. Thermo Nicolet corporation, FTIR vs. dispersive infrared theory of infrared spectroscopy instrumentation. Madison: Thermo Electron, 2002.

[110]. K. L. Lewis, A. M. Pitt, A. G. Cullis, N. G. Chew, and L. Charlwood, laser induced damage in dense optical thin films, 472 (1985).

[111]. Y. Jiang, and C. Tang, An optical fiber methane sensing system employing a two-step reference measuring method, Sensors actuators B, 133, 174 (2008).

[112]. M. Lackner, M. Schwarzott, F. Winter, B. Kögel, S. Jatta, H. Hakbritter, and P. Meissner, CO and CO_2 spectroscopy using a 60 nm broadband tunable MEMS-VCSEL at ~ 1.55 µm, J. Opt. Lett., 31, 3170 (2006).

[113]. J. F. Hall and W.F.C. Ferguson, optical properties of cadmium sulfide and zinc sulfide from 0.6 µm to 14 µm, J. Opt. Soc. Amer., 45, 714 (1955).

[114]. M. J. Weber, Handbook of optical materials, CRC press, New York, 1st edition, 2003.

[115]. J. M. Delarios, C. R. Helms, D. B. Kao, and B. E. Deal, Effect of surface cleaning procedures on oxidation kinetics and surface chemistry, Appl. Surf. Sci., 30, 17 (1987).

[116]. P. Varotsos, comments on the formation entropy of a Frenkel defect in BaF_2 and CaF_2, Phys. Rev. B, 13, 938 (1976).

[117]. Keith L. Lewis, I. T. Muirhead, A. M. Pitt, A. G. Cullis, N. G. Chew, A. Miller, and T. J. Wyatt-Davies, Molecular beam deposition of optical coatings and their characterization, Applied optics, 28, 2785 (1989).

[118]. A. Rizzo, M. Sagace, U. Galietti, and C. Pappalettere, Measurements of strain during vapor deposition of thin films and multilayers, Thin solid films, 433, 144 (2003).

[119]. O. Wing, Analysis of VLSI multiconductor systems by bi-level waveform relaxation, IEEE.int. conf. ICCAD Dig. Tech. papers, 166 (1990).

[120]. Leo P Schuler, MEMS-based micro-spectrometer technologies for NIR and MIR wavelengths, Journal of Physics D: Applied physics.42, 1 (2009).

[121]. Jiang Huang, Quan Wen, Quiyu Nie, Fie Chang, Ying Zhou, and Zhiyu wen, Miniaturized NIR spectrometer based on novel MOEMS scanning tilted grating, micromachines, 9, 478 (2018).

[122]. T. Menkad, A. Dounavis, Resistive coupling-based waveform relaxation algorithm for analysis of interconnect circuits, IEEE transactions on circuits and systems, 64, 1877(2017).

[123]. E. Afsharipour, B. Park, C. Shafai, IEEE photonics journal, Determination of Reactive RF-Sputtering Parameters for Fabrication of SiOx Films with specified refractive Index, for Highly Reflective SiOx Distributed Bragg Reflector, 9, 1 (2017).

[124]. V. Schulz, H. Ebert, and G. Gerlach, A novel miniaturizable closed-loop Hydrogel-based pH sensor, IEEE sensors proceedings, 2011.

[125]. S. D. Senturia, Microsystem design, springer, USA, 2001.

[126]. C. A. Choi, C. K. Kim, and C. H. Jun, A self-aligned vertical comb-drive actuator on SOI wafer for a 2D scanning mirror, Journal of Micromechanics and Microengineering, 14, 1148 (2004).

[127]. D. K. Tripathi , H. Kala, K. K. M. B. D. Silva, M. Martyniuk, G. Putrino, B. Nener, and L. Faraone, Conference on Optoelectronic and Microelectronic Materials and Devices (COMMAD), 2018.

VITA

DEGINET ADMASSU

773-648-0836 3631 South Wallace, Chicago, IL 60609 dadmas2@uic.edu

EDUCATION:

PhD. Physics; **University of Illinois at Chicago, USA**
Area of Specialization: Micro-Opto Electromechanical Systems Aug. 2012 -Dec.2019

MSc. Physics; **University of Illinois at Chicago, USA** Aug. 2012- Dec.2015

MSc. Chemical Engineering; **Royal Institute of Technology**, Sweden Aug.2009- June 2011

M. Sc physics, Addis Ababa University, Ethiopia Sept 2006- Aug.2008

B. Sc physics, Bahir Dar University, Ethiopia Sept 2003- July 2006

PROFESSIONAL EXPERIENCE:

Graduate Research and Teaching Assistant Aug. 2012- Dec. 2019

- Guide undergraduate students to perform laboratory experiments on Mechanics and waves.
- Tutor undergraduate students of Science and Engineering for 5 hours per week.
- Researched on various thin films for distributed Bragg reflector applications.

Sivananthan Laboratories Inc.
Device process Engineer Sept. 2017-Jan. 2019

- Fabrication of micro actuators, including photolithographic patterning.
- Electromechanical characterization of micro-actuators.
- Design and implementation of controlled experiments.

ABSTRACTS: D. Admassu, T. Durowade, S. Velicu, W. Gao, S. Sivananthan, “Micro-Opto-Electro-mechanical (MOEMS) based MWIR Fabry-Perot Filters for Hyperspectral Imaging”, US Workshop of Physics and Chemistry of II-VI materials, 2017.

PUBLICATIONS:

Effect of Interface Grading on the optical performance of Distributed Bragg Reflectors

D. Admassu, T. Durowade, and S. Sivananthan In preparation

Estimation of the Mechanical Stiffness Constant of MEMS-based Parallel-Plate Micro-Actuators

D. Admassu, T. Durowade, W. Gao, S. Velicu, S. Sivananthan In preparation